On the Maclaren River volcanic field: Petrogenesis of Pleistocene Yakutat slab tear volcanism in south-central Alaska, (USA)

by

Alexander Thomas Bearden

B.S., University of Missouri – Kansas City, 2021

A THESIS

submitted in partial fulfillment of the requirements for the degree

MASTER OF SCIENCE

Department of Geology
College of Arts and Sciences

KANSAS STATE UNIVERSITY
Manhattan, Kansas

2023

Approved by:

Major Professor
Dr. Matthew Brueseke

Abstract

The Maclaren River volcanic field (MRVF) of south-central Alaska consists of at least three monogenetic volcanoes that lie along the projection of the ca. ~1 Ma Yakutat slab tear. These volcanoes, which are <1 Ma. lie along a ~20 km south-north transect within the Denali Gap, a region between the Aleutian and Wrangell Arcs previously considered to be amagmatic. In this study, I present results from geologic mapping, thin section petrographic analysis, whole rock major and trace element geochemical analysis, and Sr-Nd-Pb-Mg-B isotopic analyses of lavas and pyroclastic deposits of three MRVF volcanoes to document their physical volcanology and petrogenesis.

Maclaren River volcanic field eruptive products (e.g., lavas and near-vent pyroclastic deposits) range from alkali basalt to subalkaline basaltic andesite and transitional basaltic trachyandesite/trachyandesite (~46-57 wt% SiO_2). The studied volcanoes are named #1, #2, #3, from north to south. Volcano #1 (ca. 958 ka) lavas are porphyritic and contain olivine phenocrysts in a groundmass of clinopyroxene + plagioclase ± sparse biotite microlites. Volcano #2 lavas and scoria are porphyritic and their mineralogy is indicative of a more hydrated mantle source (abundant phlogopite + amphibole + olivine + clinopyroxene phenocrysts) and show evidence of crustal interaction (granitic xenoliths). Volcano #3 is located ~9 km south of volcano #2, but erupted coevally at ca. 422 ka. At volcano #3, the rocks consist of olivine + clinopyroxene + plagioclase + opacitic amphibole and show evidence of crustal interaction (plagioclase + quartz xenocrysts). Sr-Nd-Pb isotopic analysis was conducted on a subset of samples from each MRVF volcano via thermal ionization mass spectrometry and multicollector inductively coupled plasma mass spectometry. $^{87}Sr/^{86}Sr_i$ values range from 0.70343-0.70401 and are similar to modern Aleutian and Wrangell Arc magmas and the Holocene, Buzzard Creek

maars. This similarity is also borne out by Nd-Pb isotope data. All MRVF volcanoes display primitive mantle-like δ^{26}Mg values (-0.20 to -0.29). Volcanoes #1 and #2 display depleted mantle-like δ^{11}B values, while volcano #3 has a more positive δ^{11}B, suggesting influence from altered oceanic crust.

I suggest the MRVF involves magma production in a subduction-affected environment, along a nascent slab tear (e.g., LILE enrichments, HFSE depletions, and adakite-like bulk rock chemistries). Batch melt modeling indicate three mantle sources for MRVF magmas: (1) a mantle wedge metasomatized by slab-derived sediment melt; (2) subcontinental lithospheric mantle also metasomatized by a slab-derived sediment melt; and (3) an eclogitic slab, where slab melts interacted with mantle peridotite. The magmas that formed volcano #1 are dominated by source #1, a metasomatized lithospheric mantle source. Volcano #2 is dominated by source #2, metasomatized subcontinental lithosphere, and volcano #3 is dominated by source #3, an eclogitic slab. This study provides further constraints on magma generation and mantle upwelling processes along flat slab tear/edge environments, as well as the tectonomagmatic processes that occurred at ~1 Ma in south-central Alaska, when the collision of the thickest (~30 km) segment of the Yakutat slab occurred.

Table of Contents

List of Figures

List of Tables

Acknowledgements

I am incredibly grateful to everyone who has supported me over the course of my graduate work and research career thus far. This research was made possible by funding provided from the Geological Society of America (NSF/GSA Graduate Student Geoscience Grant # 13500-22, which is funded by NSF Award # 1949901), the Alaska Geological Society Don Richter Memorial Grant, the Association of Earth Science Clubs of Greater KC, and the Kansas State University Department of Geology.

Thank you to Dr. Fang-Zhen Teng at the University of Washington for collaborating with me on this project and handling the Mg isotope analysis. Thank you Dr. Ivan Savov at the University of Leeds and Dr. Samuele Agostini at the Instituto di Geoscienze e Georisorse for conducting our B isotope analysis and chatting about my interpretations. Thank you to Kurt, Jean, and Cheryl at the Alaskan Geologic Materials Center and Alaskan Volcano Observatory for graciously providing the Jumbo Dome samples and powders.

Thank you to my thesis advisor, Dr. Matt Brueseke for mentoring me throughout this project and recruiting me to come to Kansas State to study these weird Alaskan volcanoes. You recognized my potential as a sophomore and convinced me to join the dark side and become a geochemist. Thank you for the endless supply of coffee in the lab, appreciating my terrible geology puns/memes, and infusing your humor into our 8:30 am Mineralogy labs. You motivated me to hit the ground running and apply for the NSF GRFP and every grant we could to fund this project. We really should've bought those lottery tickets when we were in Alaska.

Thank you to Dr. Jeff Benowitz, who graciously hosted us during our Alaskan fieldwork and whose assistance was invaluable. Your questions and expertise in Alaskan geology kept me on my toes and your jokes made the mosquitos more tolerable. More importantly, you introduced

me to the delicacies of caribou and Alaskan salmon. Special thanks to Sonya Creek for joining our fieldwork adventures and convincing me that I need a fieldwork dog.

I also would like to thank Dr. Pamela Kempton for her detailed feedback on my work over the past two years, which has helped push me to become a better scientist, writer, and speaker. Thank you for sending me useful references that you came across, appreciating my geology puns, and letting me teach the Petrology labs. Isotopes seem a little less like dark magic thanks to you.

Special thanks to all my friends in Manhattan that have made this experience more enjoyable. Sonjay, Onna, Meg, Lydia, and Meseeks, thank you for the late-night adventures, Hi Lo shenanigans, and friendship over the past two years. Thank you to my fellow cohort and students, especially Will, Carrie, Isabella, Kyle, Vidhesh, and Christa. Thank you to Hunter for all that you do for myself and the rest of the Geology Department at Kansas State.

I wouldn't have even considered graduate school without the support from my mentors, friends, and colleagues at the University of Missouri – Kansas City. Thank you to Dr. Alison Graettinger for your mentorship over the years, writing numerous letters of recommendation at last minute's notice, and preparing me for graduate school. Who would've thought drawing circles would get me this far? Thank you, Dr. Topher Hughes, for reminding me that I should be writing. Kadie, thank you for our discussions about graduate school and all the help you gave on my undergraduate petrology labs. Who knew I'd end up becoming a petrologist? Aaron, Trenton, Joe, and Hannah, I'm incredibly grateful for your friendship over the years. Trenton, thank you for exploring Portland, Denver, and Chicago with me during GSA and AGU conferences. I've got a spot in my small Bay Area bedroom reserved for you this next AGU meeting. Aaron, thank you for the City Barrel connection, the good times, and our fieldwork adventures. We need to go

to Idaho for another Prime Rib sandwich. Joe, thank you for recruiting me for my first undergraduate research project at Diamond Craters, mentoring me throughout my undergrad, and your friendship. Special thanks to Ben and Joe at City Barrel Brewing Company for the hospitality and my honorary employee status.

Lastly, I'd like to thank my family. Thank you for supporting me during this journey. Thank you to my mom, for your encouragement, mutual interest in cool rocks, and always making sure that I have food. Thank you to my grandmother and dad, for checking in on me and expressing their interest in my research. Riley, thank you so much for your friendship and always being willing to take a look at my writing. Asia, thank you for supporting me from the beginning and putting up with me leaving for weeks at a time on my volcano pursuits. To my cat Indie, thank you for waking me up at 6 am demanding to be fed and doing your best to distract me while I work.

Chapter 1 - Introduction

The relationship between arc magmatism and subducting slab features (e.g., geometry, obliquity, dip, etc.) is vital in understanding melt generation and migration in anomalous convergent margin settings such as during flat slab subduction. Flat slab subduction is characterized by shallow subduction angles (<30°) and often results in the near cessation of arc magmatism (Gutscher *et al*., 2000). Yet, significant arc magmatism can be generated along the edge and along tears of the flat subducting slab (e.g., Yogodinski *et al*., 2001; Brueseke *et al*., 2019; McLeod *et al*., 2022). Moreover, the processes that influence magma generation, along with the distribution of volcanism at slab edge environments, are unclear (Martin-Short *et al*., 2018). Therefore, studying the magmatic processes along flat slab edges and tears may further constrain how magma is formed and erupts in generally amagmatic settings.

The Maclaren River volcanic field (MVRF) in south central Alaska is an ideal place to investigate mantle upwelling in a slab tear/edge environment by studying eruptive products (Figure 1.1). The MRVF consists of at least three newly recognized Pleistocene monogenetic volcanoes (volcano #1, #2, and #3; Brueseke *et al*., 2023; Figure 1.2) situated along a ~21 km south-north transect within the Denali volcano "gap", a region between the Aleutian arc and Wrangell Arc previously considered to be amagmatic (Fuis *et al*., 2008; Chuang et al., 2017; Brueseke *et al*., 2023). The MRVF volcanoes lie above the projection of the imaged Yakutat slab tear (Mann *et al*., 2022). The MRVF's Pleistocene eruption ages (ca. 958 ka to 422 ka) and slab tear geochemical affinity are interpreted to reflect the onset of Yakutat slab tear formation due to Yakutat oceanic plateau collision (Brueseke *et al*., 2023).

Although MRVF geochemistry is suggestive of a slab tear origin, the petrogenesis of these slab tear volcanoes remains unconstrained. In this study, I present results from: (1)

geologic mapping; (2) thin section petrography; (3) whole rock major and trace element geochemistry and Sr-Nd-Pb-B-Mg isotope analysis of lavas and pyroclastic deposits of three MRVF volcanoes to constrain the generation and evolution of MRVF magmas. Batch melt modeling and binary isotope mixing models are employed to determine mantle sources of MRVF magmas and investigate the influence of likely subduction inputs and crustal contamination on isotopic composition of MRVF magmas. Deciphering the petrogenesis of these MRVF volcanoes has implications for understating how magma forms and erupts in locations characterized by "atypical", flat slab subduction and slab tearing, like south-central Alaska.

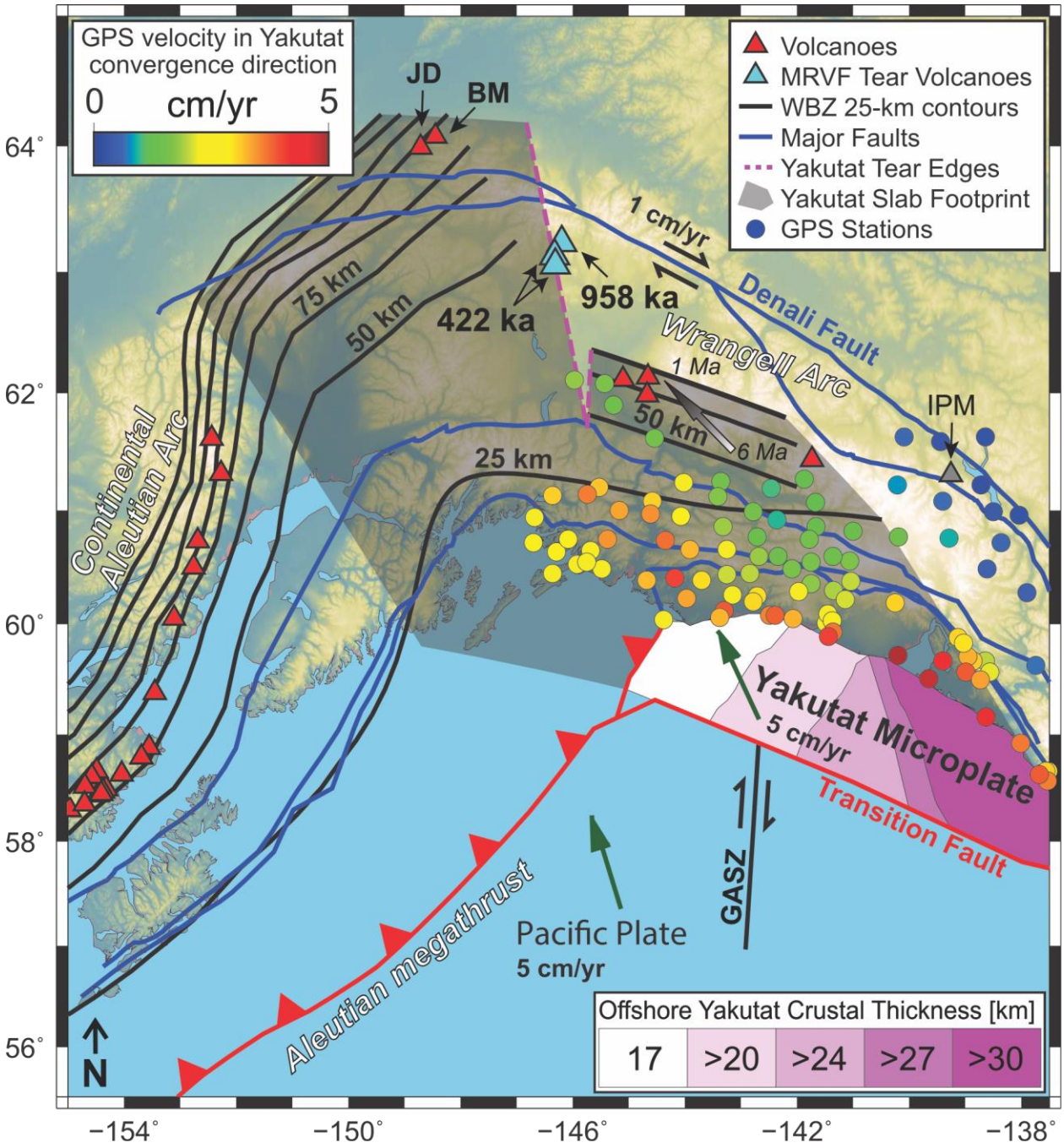

Figure 1.1: Map of the study region modified from Brueseke *et al*. (2023). Colored circles are GPS velocity values in the direction of the Yakutat block motion at selected sites across southern Alaska. Shades of magenta coloring display offshore Yakutat crustal thickness variations. Gray arrow is the general age trend of Wrangell Arc volcanism over the last 6 Ma. Abbreviations: MRVF – Maclaren River volcanic field; GASZ – Gulf of Alaska Shear Zone; Gray triangle and IPM – Miocene Wrangell volcanic belt intraplate magmatism; JD – Jumbo Dome (1.026 ± 0.057 Ma); BM – Buzzard Creek Maar (3 ka).

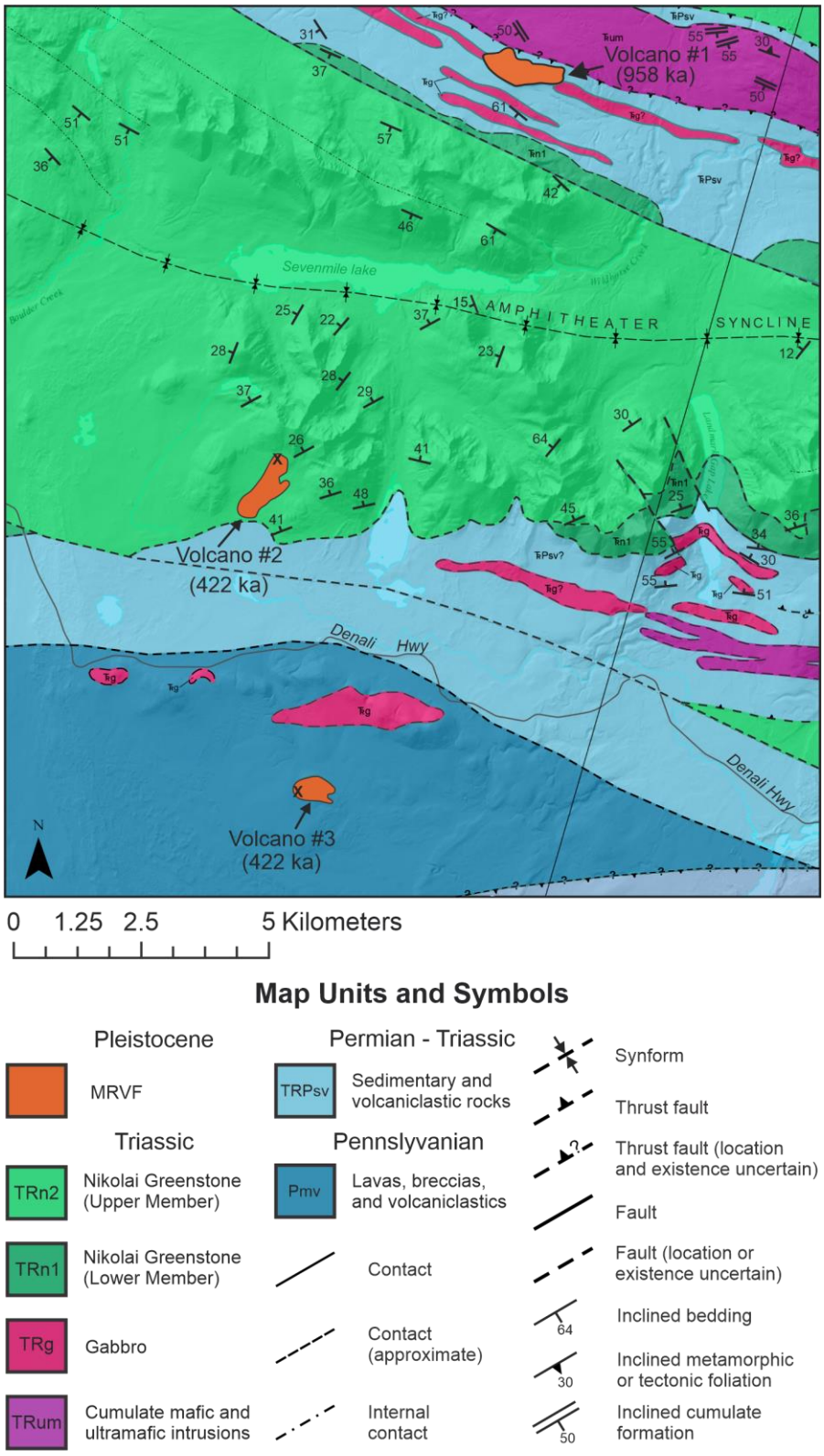

Figure 1.2: Geologic map of the Maclaren River volcanic field (MRVF) modified from Twelker *et al.* (2020) with new mapped extents of the MRVF volcanics and vent locations for volcano #2 and #3 (denoted with an X).

Magmatism at Slab Tear Environments

Slab tearing refers to a propagating tear in the slab that may form due to local collisional events, such as subduction of a buoyant high, combined with velocity variations of subduction rollback (Rosenbaum *et al*., 2008). Slab tears can form parallel or subparallel to the trench (e.g., the Hess conjugate, Elizondo-Pacheco *et al*., 2022) or perpendicular to the trench (e.g., the Pacific Plate tear in New Zealand, McLeod *et al*., 2022; the Yakutat tear, Brueseke *et al*., 2023). Slab tear formation and subsequent asthenospheric upwelling may induce magmatism in otherwise amagmatic settings (e.g., flat slab subduction, Naverette *et al*., 2021).

The geochemical signature of arc magmas is characterized by a distinct enrichment of alkalis, alkaline earth elements, and light rare earth elements (LILEs) relative to high field strength elements (HFSEs), particularly Ti, Nb, and Ta, which are usually depleted relative to primitive mantle (Wang *et al*., 2016). However, slab tear environments display a variety of magmatic processes and geochemical signatures (Yogodinski *et al*., 2001; Gasparon *et al*., 2009; Prelević *et al*., 2015; Hu *et al*., 2016; Brueseke *et al*., 2023). Slab tear formation is associated with localized lateral (toroidal) asthenospheric upwelling beneath the subducting slab and the resultant magmatism may display a general transition in geochemical signature from arc-type to ocean island basalt-type (OIB) (Prelević *et al*., 2015). Navarette *et al*. (2021) suggested that the OIB-like geochemical signature of the Las Mercedes basalt, located inboard of the Pacific trench in southern Patagonia, is related to decompression melting of fresh upwelling asthenosphere through the Aluk slab tear. Slab tearing is also interpreted to have produced the shoshonites of the monogenetic Zenobito center at Capraia Island, Italy (Gasparon *et al*., 2009). In that location, heat provided from upwelling asthenosphere through a slab tear may melt different slab components and influence melt composition (Gasparon *et al*., 2009). In Kamchatka, toroidal

mantle flow around the Pacific slab edge and subsequent upwelling through a tear is inferred to have melted the edge of the subducted Pacific slab and produced the slab melts (e.g., adakites) of Scheveluch volcano (Yogodinski *et al*. 2001). Although modern slab tears are identifiable with geophysical imaging, constraining slab tears in the geologic past usually involves interpretations based on the orientation of a chain of volcanoes/plutons and the petrogenetic history of these magmatic products. Hence, understanding the magmatic geochemical diversity of slab tear volcanoes is necessary to use their geochemical and isotopic signatures to inform the presence of a tear. Thus, studying the Pleistocene MRVF volcanoes, located over an imaged tear (Mann *et al*., 2022), will provide additional constraints on the petrogenesis and geochemical signatures of slab tear volcanoes.

Geologic Background

The Yakutat slab is an oceanic plateau that has subducted to a depth of ~500 kilometers beneath North America since 30 Ma (Brueseke *et al.*, 2019), resulting in the archetypal example of flat slab subduction/slab edge arc magmatism observed in the Wrangell Arc (Richter *et al*., 1990; Berkelhammer *et al*., 2019; Trop *et al*., 2022. The onset of Yakutat flat slab subduction generated an ~400-kilometer-wide region between the Aleutian and Wrangell Arcs that was previously considered to be amagmatic (e.g., the Denali Gap; Fuis *et al.*, 2008; Rondenay *et al*., 2010). The Denali Gap is interpreted to result from dehydration and fluid expulsion from the Yakutat slab at shallow depths which inhibit generation of significant partial melts (Chuang *et al*., 2017). Subduction of the Yakutat slab in south-central Alaska began at ~30 Ma, when volcanism in the Wrangell arc began (Brueseke *et al*., 2019).

The Yakutat oceanic plateau formed contemporaneously with the Siletzia composite terrane, which formed on the adjacent Kula plate at 55 Ma and was accreted to coastal British

Columbia by 50 Ma (Wells et al., 2014). The Siletzia composite terrane is composed of the Crescent terrane of Washington and British Columbia and the Siletza terrane of Oregon, which are all similar in composition, age, and history (Wells *et al*., 2014). Both the Yakutat and Siletzia terranes share similar basalt basement compositions, stratigraphy, and structural history. Thus, Siletzia is considered the "sister terrane" to the Yakutat (Wells *et al*., 2014). However, by 50 Ma, the Yakutat plateau began to translate northward following the Pacific capture of the Kula plate until reaching its current position (Wells *et al*., 2014; White *et al*.,2017).

Recent work by Brueseke *et al*. (2023) suggests a ca. 1 Ma age for the initiation of the Yakutat plateau collision based on the age and slab-tear geochemical affinity of the Maclaren River volcanic field. This collision likely resulted in the formation of the Yakutat slab tear, which is situated at the eastern extent of the shallowly dipping Yakutat slab and west of the Wrangell arc. The latter is underlain by a steeply dipping slab; thus the slab tear separates a region of shallow slab subduction to the east from steeper slab subduction to the west (Fuis *et al*., 2008; Daly *et al*., 2021; Mann *et al*., 2022).

The Maclaren River volcanic field is located along the southern flank of the eastern Alaska range, and MRVF rocks were originally mapped as isolated exposures of "Tertiary basalt flows" (Stout, 1976; Twelker *et al*., 2020; Waldien *et al*., 2022). Brueseke *et al*. (2023) identified eruptive vents, determined Pleistocene eruption ages for Volcano #2 and Volcano #3, and provided first order constraints for MRVF geochemistry and mineralogy.

The MRVF magmatic system erupted through the Insular terrane, which consists of three allochthonous terranes (Peninsular, Wrangellia, and Alexander Terranes) that accreted to western North America by ca. 117-114 Ma (Trop *et al*., 2020). The Insular terrane consists of three major rock sequences: (1) a late Paleozoic sequence of sedimentary, volcanic, and granitic plutonic

rocks constituting the Skolai island arc; (2) the Late Triassic to Early Triassic Peninsular island arc sequence composed of volcanic and plutonic rocks constituting the Talkeetna island arc; and (3) the Middle to Late Triassic Nikolai Greenstone formation and capping limestone that formed in a major rifting event (Berg *et al*., 1972; Plafker and Berg, 1994; Trop *et al*., 2002; Manuszak *et al*., 2007; Snyder and Hart, 2007; Greene *et al*., 2008; 2009; Nokelberg *et al*., 2015; Berkelhammer *et al.*, 2019). The Nikolai Greenstone is a 3.5 – 4 km thick unit composed of amygdaloidal tholeiitic basalt lavas and minor associated volcaniclastic rocks that are metamorphosed to lower greenschist facies (Greene *et al*., 2008; Nokelberg *et al*., 2015).

Overlying the Insular terranes are the Upper Jurassic to Lower Cretaceous sedimentary basin rocks of the Kahiltna assemblage and the Gravina-Nutzotin belt (Aleinikoff *et al*., 2000). Located south of the Denali fault, these units are comprised of marine turbidite deposits with subordinate volcanic and continental crustal detrital components (Aleinikoff *et al*., 2000). North of the Denali fault is the Yukon-Tanana terrane of Laurentia and peri-Laurentia origin and consists of Precambrian-Paleozoic metamorphic rocks intruded by Paleozoic-Mesozoic plutons (Aleinikoff and Nokleberg, 1985; Nokleberg and Aleinikoff, 1985). The Wrangellia composite terrane to the south, is juxtaposed across from the Yukon Tanana terrane along the Denali fault system (Trop *et al*., 2019).

Eroded sediments from these terranes and overlying sedimentary units were delivered to the fore-arc basin settings and the trench through fluvial systems to the west and south throughout the Cenozoic and this process continues today (Stevenson *et al*., 1983; Stevenson and Embley, 1987, Plafker *et al*., 1994, Brennan *et al*., 2009; Finzel *et al*., 2011; 2016). Therefore, sediment delivered to the trench that was not faulted, accreted, or underplated to the continental

margin (Christenson *et al*., 2013) was likely subducted with the Yakutat microplate over the past 30 Ma (e.g., Berkelhammer, 2017).

The northern subducted extent of the Yakutat slab is often denoted by two volcanic centers located ~140-150 km northwest of the MRVF: Jumbo Dome and the Buzzard Creek maars (Figure 1.1). Jumbo Dome is a Pleistocene hornblende andesite dome located in the Healy Quadrangle of central Alaska (Albanese, 1980; Athey *et al*., 2006; Cameron *et al*., 2015). Reconnaissance work (Albanese, 1980; Cameron *et al*., 2015) shows that Jumbo Dome lavas have an arc geochemical signature (e.g., low concentrations of high field strength elements and high concentrations of large ion lithophile elements relative to primitive mantle). The Buzzard Creek maars are 3 ka and consist of two vents, ~150 m and ~50 m in diameter, located along the northern foothills of the central Alaska range (Wood and Kienle, 1990; Andronikov and Mukasa, 2010; Nye *et al*., 2018). These maars lie directly above the Benioff Zone associated with Pacific Plate subduction and are 15 km northeast of Jumbo Dome. Nye *et al*. (2015) suggested that their location within an area of transtensional right lateral "bookshelf" faulting between the Denali and Tintina faults enabled the unimpeded rise of Buzzard Creek basalt through the crust. Buzzard Creek rocks are basalts and display an arc signature (Andronikov and Mukasa, 2010). Andronikov and Mukasa (2010) suggested a mantle wedge origin for Buzzard Creek magmas based on the Sr-Nd-Pb-Hf characteristics and a non-adakitic geochemical signature (e.g., low Sr/Y ratios accompanied by high Y concentrations).

Tracing Subduction Input with Magnesium and Boron Isotopes

In this study, boron and magnesium isotopes are used to trace contributions of subducting sediment, altered oceanic crust (AOC), subducted serpentinite, or melt/fluid derived therefrom. Boron is a highly fluid-mobile element with two stable isotopes (^{10}B and ^{11}B with relative

abundances of 19.9% and 80.1%, respectively) that are useful for tracing hydrous fluid transfer from the slab to the mantle (Forster *et al*., 2016). Boron is highly soluble in subduction zone fluids and incompatible in mantle melts (Hao *et al*., 2022). Thus, B is extremely depleted in the mantle but strongly enriched and preferentially fractionated (up to 40‰ in ^{11}B) into subducted sediments, altered oceanic crust (AOC), and serpentinized mantle (De Hoog and Savov, 2018). This is due to the strong fluid partitioning of B and associated isotopic fractionation of ^{11}B during metamorphic slab dehydrations that release aqueous fluids at temperatures lower than 800 °C (Sugden *et al*., 2020). Moreover, B systematics in subduction environments are insensitive to chemical variation in the mantle and are largely unaffected by the involvement of continental crust (Morris *et al*., 1990).

Magnesium is a major element in all silicate magmas and has three stable isotopes (^{24}Mg, ^{25}Mg, and ^{26}Mg, with relative abundances of 78.99%, 10.00%, and 11.01%, respectively; Rosman and Taylor, 1998) that have been proposed as a tracer of serpentinite dehydration and bulk serpentinite contributions of arc rocks (Teng, 2017; Hu *et al*., 2020; Hao *et al*., 2022). Mg isotope ratios are reported in standard δ-notation (‰) relative to the international reference solution standard DSM3: $\delta^{25,26}Mg = [(^{25,26}Mg/^{24}Mg)_{sample}/(^{25,26}Mg/^{24}Mg)_{DSM3} - 1] \times 10^3$. Magnesium isotopes are fractionated by surficial and low-temperature processes (e.g., chemical weathering fractionates light ^{24}Mg) rather than high-temperature magmatic processes (Teng *et al*., 2016). The lack of Mg isotope fractionation as a result of partial melting and magma differentiation creates a homogeneous δ^{26}Mg isotopic composition of the mantle on a global scale (-0.25 ± 0.07‰; Teng *et al*., 2010). Oceanic abyssal peridotites and mantle wedge peridotites at the slab interface have high δ^{26}Mg values and higher MgO concentrations than subducted sediment and altered oceanic crust, therefore δ^{26}Mg of arc magmas can be used to

trace serpentinite components in their source, i.e., those with higher δ^{26}Mg values with high MgO concentrations are inferred to have higher concentrations from subducted serpentinite (Hao *et al*., 2022). Bulk AOC and sediment do not significantly contribute to the high δ^{26}Mg of arc magmas; however, meta-peridotites (e.g., talc-rich serpentinite) at the slab-mantle interface display high δ^{26}Mg values (up to -0.01 ‰) and are inferred to contribute to high δ^{26}Mg of arc magmas (Hao *et al*., 2022). Fluids derived from AOC and sediment melts cannot significantly modify Mg isotope compositions in the mantle as they typically display lower MgO concentrations than mantle peridotites (Hao *et al*., 2022). Moreover, studies of Mg isotopes of Kamchatka arc xenoliths found that fluid-dominated slab input would display overwhelming mantle-like Mg isotope compositions (Hu et al., 2020).

Chapter 2 - Methods

Newly collected MRVF samples from volcano #2 and #3 were combined with the preliminary suite of samples studied by Brueseke *et al*. (2023). Fieldwork focused on sampling rocks from a fuller extent of MRVF lavas and also determining source vent locations. Volcano #1 was not targeted in this study due to the inaccessibility of the field site, thus samples from Brueseke *et al*. (2023) were incorporated here. Samples were described in the field and subsequent petrography via thin sections occurred later at Kansas State University. Thin section petrography was performed on 14 samples from the MRVF and one sample from Jumbo Dome.

Erupted Volume Calculations

Volume estimates for volcano #2 and #3 were obtained using ArcGIS 2.92 following methodology described in Brueseke *et al*. (2014). A Digital Elevation Model (DEM) at 5m resolution was downloaded from the United States Geological Survey ScienceBase Catalog

(USGS Alaska 5 Meter AK_IFSAR_2010 23). Polygons were digitized along the perimeters of volcano #2 and #3 by the Create Feature tool in ArcGIS. The Extract by Mask tool was used to restrict the DEM to the defined areas of volcano #2 and #3. The Spatial Analyst toolset was used to calculate volumes. The raster calculator tool was used to subtract the minimum elevation value from every cell within the masked DEM. The raster calculator works on an individual cell basis, applying a function or operation to each cell in the raster. Therefore, the raster calculator was then used to multiply the output DEM by the area of its cells (25m), creating a new output DEM that represented the volume of earth within that cell. The zonal statistics tool was used to sum the values of the cells within the polygon, and this sum is treated as an estimate of erupted material.

Geochemical and Isotope Analysis

Whole Rock Major and Trace Element Geochemistry

Rock samples were prepared at Kansas State University using a RockLabs Hydraulic Press with tungsten splitting jaws. Weathered surfaces were removed via a diamond-tipped rock saw and a 60-grit sandpaper grinding wheel. Samples were then cleaned in deionized water with a toothbrush and allowed to dry. After drying, samples were crushed to gravel-size using the tungsten crushing plates of the RockLabs Hydraulic Press and randomized using a cone-and-quarter method on a glass plate. Approximately 25 mL of crushed sample was powdered using a Spec Industries shatterbox machine and an alumina shatterbox assembly for eight minutes.

Three new MRVF rock powders from volcano #2 and #3, along with powder from Jumbo Dome (acquired from the Alaska Division of Geological and Geophysical Surveys), were sent to the Hamilton Analytical Lab for whole rock major (XRF) and trace element analysis (LA-ICP-MS) following methods described in Conrey *et al*. (2023). The rock powders, normally 3.5 g,

were weighed with a lithium-tetraborate ($Li_2B_4O_7$) flux at a 1:2 ratio. Next, the powder and flux were blended with a vortex blender and fused in graphite crucibles at 1000°C in a controlled muffle furnace. The resulting beads were cleansed of any residual carbon, reground to a fine powder using a tungsten carbide ring mill, and subsequently fused at 1000°C. The pellets were lapped flat to a surface finish of 15 microns and then ultrasonically cleansed in ethanol.

The samples were analyzed on a Thermo ARL Perform'X x-ray fluorescence spectrometer, measuring 44 elements (major and trace). Only major elements are reported here and are as weight percent oxide (SiO_2, TiO_2, Al_2O_3, Fe_2O_3, MnO, MgO, CaO, Na_2O, K_2O, and P_2O). Total volatiles loss on ignition (LOI) was determined for each sample by heating overnight in silica crucibles at 900°C. For LA-ICP-MS analysis, low dilution lithium-borate-fused glass pellets were analyzed to minimize nugget effects. Moreover, an in-house drift monitor (HAL-2A) was used, as it has similar sensitivities at all atomic numbers when compared to the standard NIST 160, which is not consistent across a wide range of atomic numbers. Hamilton Analytical Labs also uses a newer code, which was written to calculate weight means for multiple internal standards. A photon Machines Analyte 193 (G1) ablation station (UV excimer laser, 193 nm, with laminar flow frame cell) attached to a Varian 820 single quadrupole mass spectrometer was used to ablate samples and standard at Rensselaer Polytechnic University. The laser spot size is 150 μm^2 and has a 7 hz repetition rate. Helium carrier gas carried the ablated material from the laser cell toward the Varian 820 ICPMS, mixing with Ar to 20 ml before entering the plasma torch. The ICP-Ms is run in "peak-hopping, time-resolved mode" for 54 major and trace element analyses, with dwell times around 10 ms per mass (Conrey *et al*., 2019; Conrey *et al*., 2023). Major elements are reported as wt% oxide and trace element concentrations are presented as parts per million (ppm). All major, trace, and rare- earth element (REE) data are presented in

Table 3.1. Fe was split according to Le Maitre (1976) and all major element data used in diagrams and the discussion are reported as anhydrous using the split Fe data.

Radiogenic Sr-Nd-Pb Isotopes

Four MRVF samples and one Jumbo Dome sample were sent to Miami University for radiogenic Sr-Nd-Pb isotope analysis. One hundred mg of powdered sample was dissolved in concentrated HF-HNO_3. Sr, Nd, and Pb were separated from a given sample aliquot using ion exchange chromatography following the standard procedures described in Snyder (2005). Sr and Nd isotope data were then analyzed via Thermo-Finnigan Triton thermal ionization mass spectrometer (TIMS). Measured $^{87}Sr/^{86}Sr$ isotopic ratios were corrected for mass fractionation using $^{86}Sr/^{88}Sr = 0.1194$. Measured $^{143}Nd/^{144}Nd$ isotopic ratios were fractionation corrected using $^{143}Nd/^{146}Nd = 0.7219$. External precision based on long-term two standard deviation (2 S.D.) reproducibility of the NBS 987 Sr and the La Jolla standards are ± 0.000015 for $^{87}Sr/^{86}Sr$ and ± 0.000007 for $^{143}Nd/^{144}Nd$. Sr-Nd isotope data were age corrected to ca. 1 Ma based on the $^{40}Ar/^{39}Ar$ age reported for volcano #1 in Brueseke *et al*. (2023). Sr-Nd-Pb isotope data is reported in Table 3.1. εNd was calculated using $^{143}Nd/^{144}Nd = 0.512630$ and $^{147}Sm/^{144}Nd = 0.1960$ for CHUR (Bouvier *et al*., 2008).

Pb measurements were obtained for each sample on separate sample dissolutions via Nu Plasma multi-collector inductively coupled plasma mass spectrometer (MC-ICP-MS) at Miami University, using the TI-spike method to correct for instrumental mass bias based on the measured $^{205}TI/^{203}TI$ ratios. Measured $^{204}Hg/^{202}Hg$ was used to correct for the isobaric inference of ^{204}Hg on ^{204}Pb. The 2 S.D. external reproducibility of NBS 981 standard reference material during the analytical campaign was ± 0.0022 for $^{206}Pb/^{204}Pb$, ±0.0019 for $^{207}Pb/^{204}Pb$, and ± 0.0060 for $^{208}Pb/^{204}Pb$.

Mg-B Isotopic Analysis

In addition to four samples from the MRVF, four samples from the 0-30 Ma Wrangell Arc and one sample from the 1 Ma Jumbo Dome were chosen for Mg-B isotope analysis to expand the Mg-B isotopic dataset of samples from south-central Alaska and for comparison to the MRVF. The Wrangell Arc samples were picked due to the availability of their Sr-Nd-Pb isotope data. Rock powder from nine samples representing the MRVF, Jumbo Dome, and Wrangell Arc were sent to the Isotope Laboratory in the Department of Earth and Space Sciences at the University of Washington. The detailed sample dissolution, separation, and purification steps are described in Teng *et al*. (2007, 2010, 2015). The samples were analyzed for Mg isotopic content via Nu Plasma MC-ICP-MS. The measured Mg isotope ratios are reported in standard δ-notation (‰) relative to the international reference solution standard DSM3: $\delta^{25,26}Mg = [(^{25,26}Mg/^{24}Mg)_{sample}/(^{25,26}Mg/^{24}Mg)_{DSM3} - 1] \times 10^3$. The precision of the measured $^{26}Mg/^{24}Mg$ ratio for one sample solution at the 2 S.D. level, based on repeat standard analysis during a single analytical session is < 0.065 ‰, and is comparable to previous Mg isotope studies (Teng *et al*., 2010; Brewer *et al*., 2018). The reference materials BHVO-2 (Hawaiian Basalt) and BCR-2 (Colombia River Basalt) were analyzed to evaluate the accuracy and repeatability of the samples, yielding $\delta^{26}Mg$ values consistent with previously published data (e.g., Teng *et al*., 2015; Ke *et al*., 2016) (-0.23 ± 0.050 and -0.16 ± 0.064, respectively).

Nine samples were selected for analysis of B concentrations and B isotope ratios, including four MRVF samples, four samples from the Wrangell Arc, and one Jumbo Dome sample. Analyses were performed at the Istituto di Geoscienze e Georisorse of the Italian National Research Council (IGG-CNR) in Pisa, Italy via Multi-Collector ICP-MS technique after B extraction from matrix, following methods described in Agostini *et al*. (2021). Results from

the boron isotope analysis are reported in standard δ-notation ($\delta^{11}B$) which represents the ‰ deviation from the NIST SRM 951 standard, with a certified $^{11}B/^{10}B$ ratio of 4.04362, where $\delta^{11}B = [(^{11/10}B)_{sample} / (^{11/10}B)_{NIST\ RSM\ 951} - 1] \times 1000$ (‰). The accuracy of the measurement was monitored by replicate analyses of the standard NBS 951. Five replicate analyses of shelf NBS 951 gave an average $\delta^{11}B$ of -0.07 ± 0.12 (2 S.D.), which is consistent with values reported in Agostini *et al*. (2021). Two replicate analyses of NBS 951 after full chemistry gave an average $\delta^{11}B$ of 0.01 ± 0.18 (2 S.D.). For B concentrations, known concentrations of NBS 951 boron solution and internal 50 ng/g and 10 ng/g standard solutions were used to construct a calibration line, which was used to determine the unknown sample boron concentrations using the known volumes of the reagents used during sample extraction and purification.

Chapter 3 - Results

Field Relations and Physical Characteristics

Fieldwork in July of 2022 targeted volcano #2 and volcano #3 to identify vent facies, collect new samples for geochemical analysis, and determine their erupted extent. Volcano #1 was not targeted because its inaccessibility required helicopter transportation, while volcanoes #2 and #3 are located within hiking distance of the Denali Highway. Field descriptions of volcano #1 below are based on photography provided by Dr. Jeff Benowitz.

Volcano #1

Volcano #1 is located ~18 km north of the Denali Highway and ~12.5 km northeast of volcano #2 (Figure 1.2) and consists of olivine-phyric platy lavas (Figure 1.1).

Volcano #2

Volcano #2 is located ~4 km north of the Denali Highway (Figure 1.2) and consists of blocky to olvine-clinopyroxene-phlogopite-amphibole-phyric platy lavas and pyroclastic tephra

that erupted through the nearby Nikolai Greenstone unit. The lavas are platy closer to the vent and transition to a blockier morphology as they extend toward the Denali Highway and down-slope; the pyroclastic tephra is concentrated near the vent (Figure 3.2). This vent location was identified from vent-proximal pyroclastic facies (e.g., pervasively oxidized reddish-brown blocks and bombs scattered among platy lava). The flow direction of volcano #2 lavas follows paleotopography. The estimated erupted area is 1.03 km^2 and the volume is 0.095 km^3.

Volcano #3

Volcano #3 is located ~3.5 km south of the Denali Highway and roughly ~8 km south of Volcano #2 (Figure 1.2). The volcanics here consist of platy to blocky olivine-clinopyroxene-amphibole-phyric lavas as well as vent-proximal facies represented by pervasively oxidized, welded clastogenic spatter containing crustal xenoliths (Figure 3.3). The lavas appear to be benched on the eastern slide. The estimated erupted area is 0.51 km^2 and the volume is 0.030 km^3.

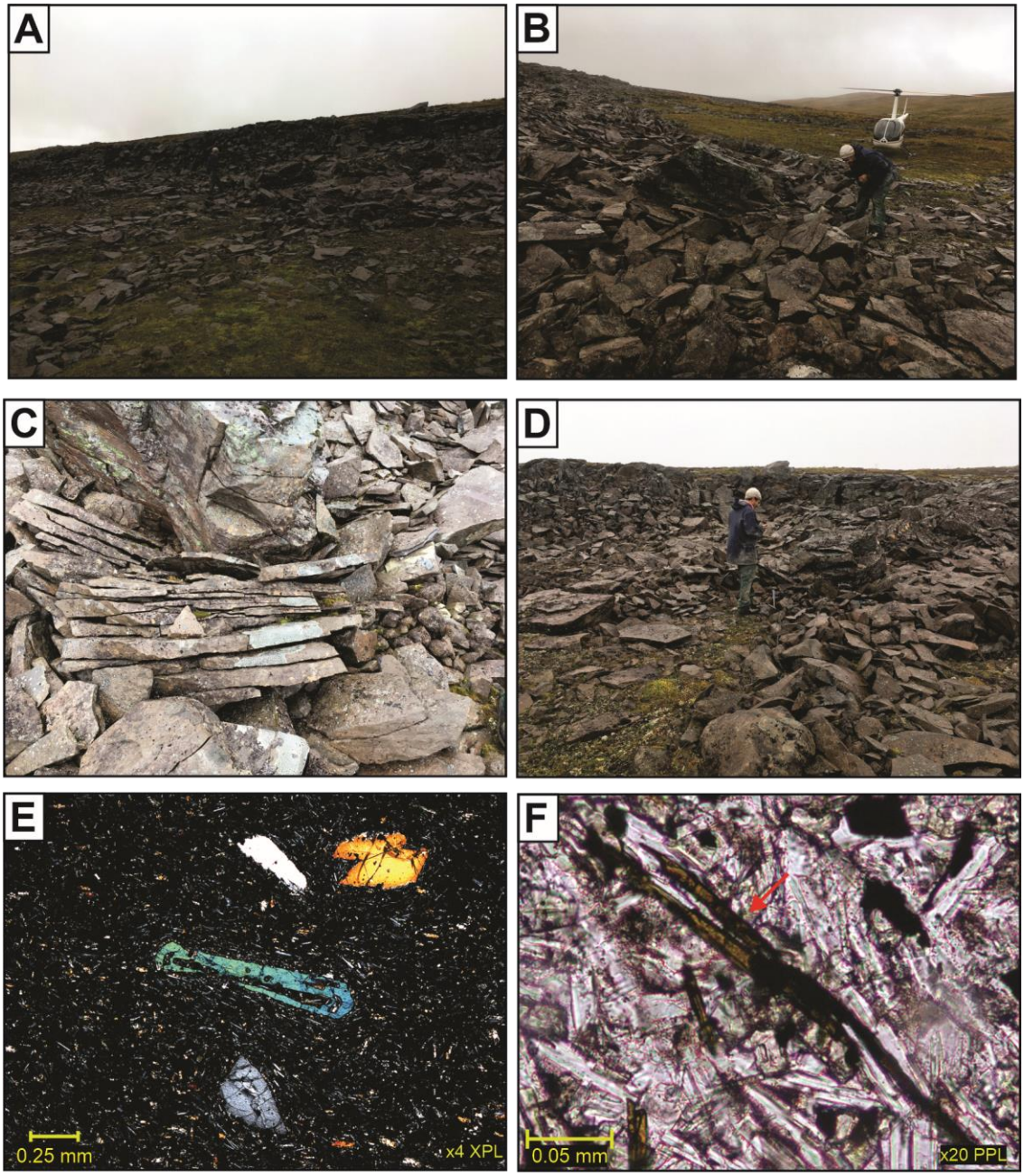

Figure 3.1: Field photos of volcano #1 and photomicrographs. (A-D) Photos of blocky volcano #1 lavas. (E) Photomicrograph of an olivine phenocryst with a swallowtail morphology. (F) Photomicrograph of a groundmass biotite microlite (denoted by the red arrow). Field photos courtesy of Dr. Jeff Benowitz.

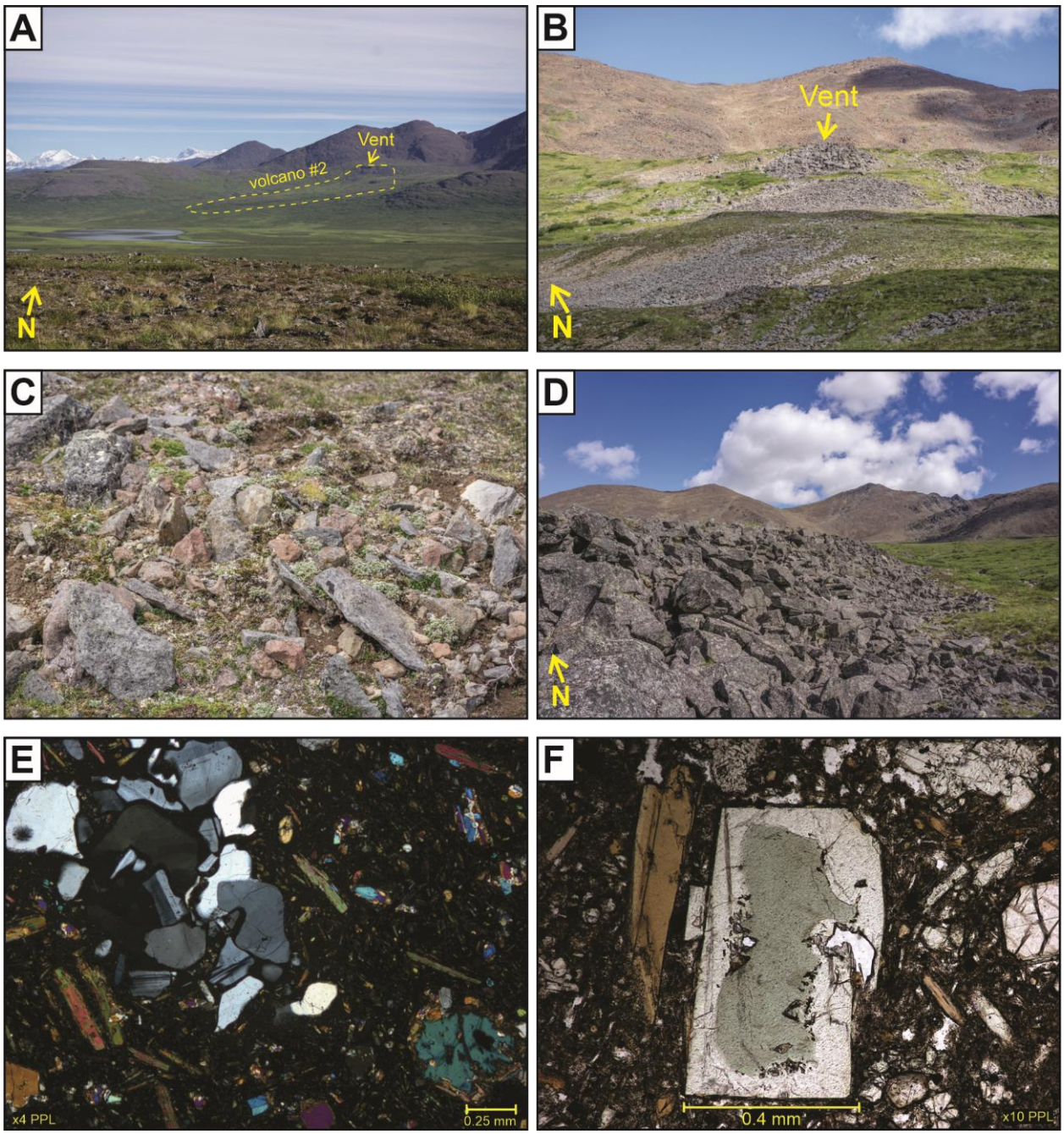

Figure 3.2: Field images of volcano #2 and photomicrographs. (A) view of volcano #2 and its erupted extent from south of the Denali Highway. The yellow dashed lines highlight the approximate erupted extent (B) and (C) volcano #2's vent location and vent-proximal pyroclastic facies consisting of reddish-brown blocks and bombs scattered among volcano #2's platy lava. (D) Blocky lava from volcano #2. (E) Photomicrograph of a granitic xenolith in sample DEN20-13 with phlogopite and olivine phenocrysts nearby. (F) Photomicrograph of a clinopyroxene phenocryst with aegirine core.

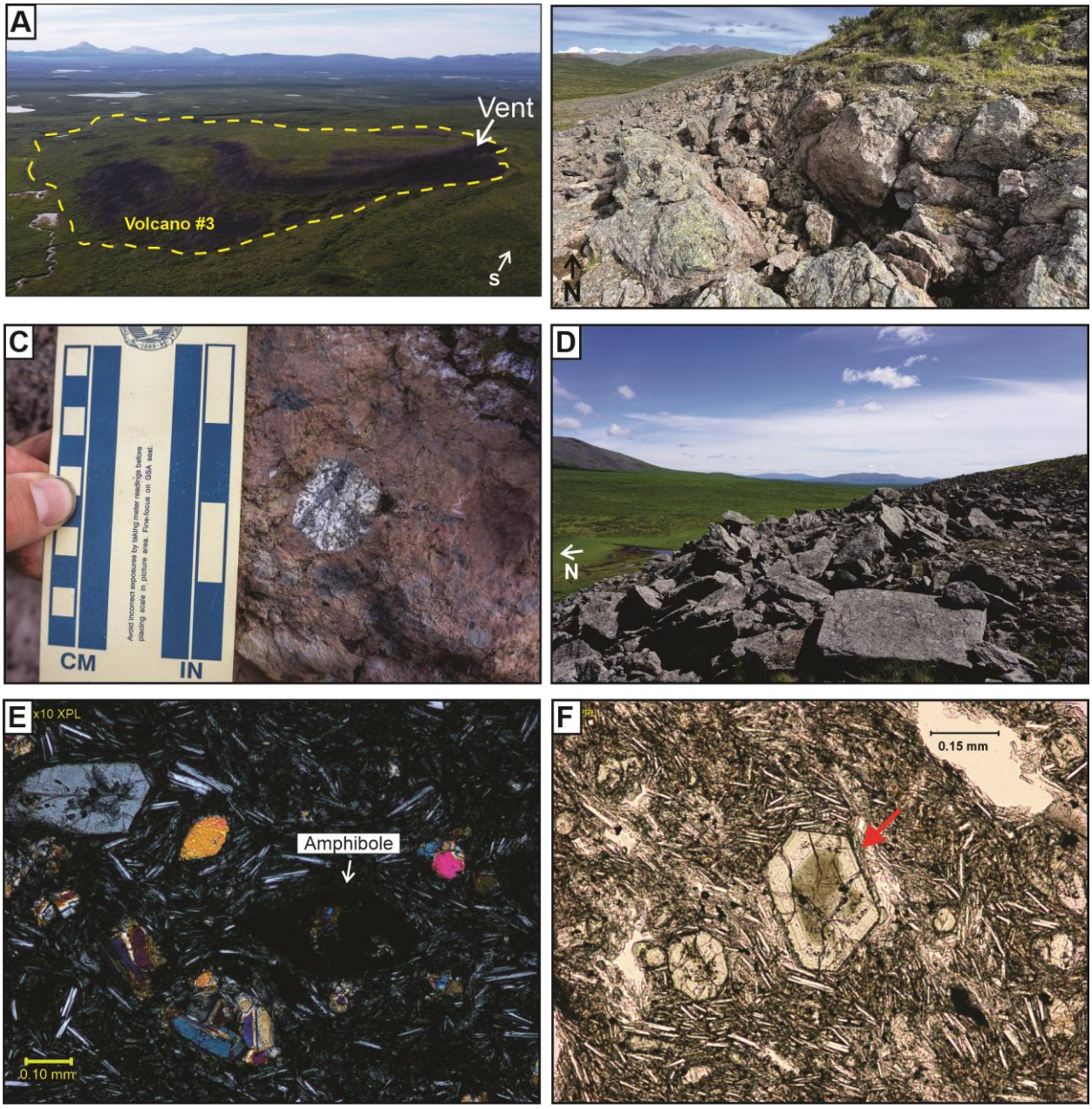

Figure 3.3: Field images of volcano #3 and photomicrographs. (A) Aerial imagery of volcano #3 with yellow dashed line denoting the approximate erupted extent. (B) and (C) View of volcano #3's vent and vent-proximal pyroclastic facies consisting of pervasively oxidized, welded clastogenic spatter with crustal xenoliths. (D) Platy lava on the eastern side of volcano #3. (E) Photomicrograph of volcano #3's mineralogy with an opacitic amphibole crystal. (F) A clinopyroxene phenocryst with an aegerine core observed in sample AB22-4.

Petrography

Volcano #1

Volcano #1 lavas are holocrystalline and porphyritic, consisting of subhedral olivine phenocrysts (0.27 – 1.18 mm) set within a finer-grained, intersertal glassy groundmass consisting of plagioclase, clinopyroxene, oxides, and biotite microlites. Groundmass crystals are less than > 0.21 mm in size, with larger plagioclase and clinopyroxene, and smaller biotite and oxides (Figure 3.1E-F). These groundmass crystals are generally subhedral. Olivine phenocrysts commonly host spinel inclusions and display resorbed margins. Groundmass plagioclase ranges from pilotaxitic to felty flow textures. Alteration is restricted to partial iddingsitization of olivine along fractures and grain boundaries.

Volcano #2

Volcano #2 consists of lavas and pyroclastic rocks that are highly phyric (18 – 27% phenocryst content), consisting of olivine-clinopyroxene-amphibole-phlogopite phenocrysts. Phenocrysts range in size from 0.25 – 1.6 mm with larger olivine, clinopyroxene and phlogopite, and smaller amphibole. In the pyroclastic tephra, these phenocrysts are set within a finer-grained, glassy groundmass of plagioclase, olivine, phlogopite, clinopyroxene, amphibole and oxides. In the lavas, these phenocrysts are set within a more crystal-rich, groundmass consisting of plagioclase laths, olivine, phlogopite, clinopyroxene, and oxides. Groundmass crystals range from 0.005 – 0.20 mm with all minerals encompassing this size range.

Slight alteration is found within the groundmass, olivine, phlogopite, and amphibole. Olivines display partial iddingsitization along fractures and grain boundaries. Phlogopite and amphibole are rarely altered to chlorite. Volcano #2 rocks are glomeroprophyritic with glomerocrysts of olivine-clinopyroxene-phlogopite. These samples also contain quartz-

plagioclase-microcline xenocrysts and xenoliths (0.40 – 4.95 mm) that are commonly partially resorbed. Quartz xenocrysts may display clinopyroxene and plagioclase reaction rims. Phenocrysts of olivine and clinopyroxene also display evidence of resorption and have sieve textures. Some phlogopite phenocrysts exhibit black/brown opacitic rims with sieve textures and resorption. Plagioclase and clinopyroxene phenocrysts display oscillatory zoning. Notably, sample DEN20-13 contains a clinopyroxene with a resorbed aegirine core (Figure 3.2F).

Volcano #3

Volcano #3 rocks consists of hypocrystalline, porphyritic lavas with olivine, clinopyroxene and opacitic amphibole phenocrysts suspended in a finer-grained, microcrystalline/ cryptocrystalline groundmass consisting of plagioclase laths, olivine, clinopyroxene, opacitic amphibole, oxides and microlites of biotite (> 0.2 mm). Phenocrysts range in size from 0.30 to 0.82 mm with larger olivine and clinopyroxene and smaller amphibole. Groundmass crystals are less than 0.25 mm in size. Alteration is restricted to the biotite microlites and iddingsitized olivine. Olivine and clinopyroxene phenocrysts display evidence of resorption and sieve textures. The lavas are also glomeroporphyritic with olivine-pyroxene-plagioclase glomerocrysts. Groundmass plagioclase crystals are pilotaxitic, with few displaying a variolitic texture. Clinopyroxene phenocrysts are commonly compositionally zoned. Sample AB22-4 contains a clinopyroxene phenocryst with a resorbed aegirine core (Figure 3.3F).

Xenoliths and xenocrysts are present in the form of siliciclastic lithics (0.40 –0.81 mm) and granitic chunks of plagioclase, potassium feldspar, and quartz (0.3 - 1 mm). These granitic xenoliths and xenocrysts commonly display sieve textures and evidence of resorption.

Whole Rock Geochemistry

Bulk Rock Geochemistry and Geochemical Classification

MRVF geochemical composition clusters in three groups, consistent with their monogenetic nature (Brueseke *et al*., 2023; this study; Table 3.1; Figures 3.3, 3.4). On a total alkali vs. silica diagram (TAS) (LeBas *et al*., 1986), rocks from volcano #1 plot as sub-alkaline basaltic andesites (Figure 3.3A). On a wt% K_2O vs. wt% SiO_2 discrimination diagram (Pecerillo and Taylor, 1976) these rocks plot as high-K calc-alkaline (Figure 3.3B). Volcano #1 rocks also plot as calk-alkaline on an alkali-iron-magnesium (AFM) diagram (Irvine and Barager, 1971) and are more enriched in wt% FeO* and wt% TiO_2 than volcano #2 and #3 (Figure 3.4 and Figure 3.5; Table 3.1). These rocks are the least primitive of the MRVF with Mg# of ~57 (Table 3.1; where Mg# = 100* (MgO/40.32)/((MgO/40.32) + (FeO/71.85)).

In contrast, rocks from volcano #2 are more primitive, plotting as alkaline basalts and trachybasalts on Figure 3.3A. The trachybasalts may be subdivided and classified as potassic trachybasalts after Le Maitre *et al*. (2002) (wt% Na_2O – 2.0 < wt5 K_2O). On a plot of wt% K_2O vs. wt% SiO_2, rocks from volcano #2 plot within the shoshonitic series (Figure 3.3B). Rocks from volcano #2 bear similar mineralogy to shoshonites (e.g., olivine and clinopyroxene phenocrysts) but lack potassium feldspar, thus here these rocks are defined as shoshonite-like to refer to their high-K, shoshonitic geochemical affinity. Volcano #2 rocks plot as calc-alkaline on an AFM diagram but are less differentiated than volcano #1 and #3 (Figure 3.4). Volcano #2 rocks are also the most enriched in wt% CaO, K_2O, MgO and least enriched in wt% Al_2O_3 (Figure 3.5). Volcano #2 rocks are the most primitive within the MRVF and have Mg#s ranging between ~70 – 72 (Table 3.1).

Finally, rocks from volcano #3 are subalkaline/transitional and plot on the border between basaltic-trachyandesites, trachyandesites, and andesites (Figure 3.3A). These rocks are calc-alkaline on both a wt% K_2O vs. wt% SiO_2 and AFM diagram (Figure 3.3B and Figure 3.4). On the Harker diagrams of Figure 3.5, rocks from volcano #3 have the highest concentrations of wt% Na_2O and wt% Al_2O_3, and lowest concentrations of the other major oxides when compared to the other MRVF volcanoes.

Trace element values for MRVF rocks show the same geochemical arrays and groups as their major element characteristics (Figure 3.6 and Figure 3.7). All MRVF rocks display high Sr (617 - 3080 ppm), Ba (695 – 3196 ppm), Cr (210 – 500 ppm), and Ni concentrations (140 – 330 ppm), but rocks from volcano #2 are most enriched in these elements. Furthermore, all MRVF rocks exhibit decreasing values of large ion lithophile elements (LILE; Rb, Ba, U, Th, Pb, and Cs) with increasing SiO_2, except for sample DEN20-13 from volcano #2. Rocks from all MRVF volcanoes are characterized by LILE enrichments and high field strength (HFSE) depletions, with differences between the three sample suites (Figure 3.7; Brueseke *et al*., 2023). Notably, samples from volcano #2 are enriched in most trace elements in comparison to rocks from the other MRVF volcanoes (Figure 3.7).

Sample	DEN20-10*	DEN20-11*	DEN20-1*	DEN20-3*	DEN20-4*	DEN20-12*	DEN20-13*	DEN20-14*	AB22-1
Unit	V#1	V#1	V#2	V#2	V#2	V#2	V#2	V#2	V#2
Type	Lava	Lava	Scoria	Lava	Lava	Scoria	Scoria	Scoria	Lava
Lat. N°	63.2357	63.2368	63.1358	63.1371	63.1286	63.1364	63.1364	63.1364	63.1251
Long. W°	-146.1944	-146.1924	-146.3252	-146.3217	-146.3224	-146.3199	-146.3199	-146.3199	-146.3333
SiO_2	53.82	48.28	49.11	48.88	49.24	48.28	45.73	48.10	49.26
TiO_2	2.08	1.18	1.20	1.18	1.16	1.18	1.21	1.18	1.16
Al_2O_3	14.59	12.63	12.89	12.61	12.78	12.63	14.05	12.86	12.45
FeO*	9.23	7.36	7.40	7.36	7.24	7.36	8.01	7.76	7.28
MnO	0.135	0.131	0.14	0.129	0.131	0.131	0.144	0.134	0.134
MgO	6.91	10.84	10.46	10.51	10.28	10.84	10.75	10.70	10.21
CaO	7.58	9.62	9.87	9.88	9.68	9.62	9.54	7.90	9.66
Na_2O	2.89	2.57	2.42	3.07	3.05	2.57	2.21	2.51	2.95
K_2O	2.06	3.19	3.22	2.87	2.78	3.19	2.16	3.11	2.86
P_2O_5	0.35	1.10	1.11	1.11	1.06	1.10	1.05	1.03	1.079
LOI	-0.39	1.58	1.83	0.88	1.00	1.58	3.75	3.02	1.17
Mg#	57.2	57.1	71.4	71.8	71.7	72.4	70.5	71	71.4
Ba	758	805	3196	3193	3075	3094	3016	2744	3062
Cr	274	270	442	454	450	500	466	462	431
Cs	0.23	0.27	0.40	0.49	0.50	0.41	0.10	0.65	1.00
Cu	268	262	141	138	135	138	141	159	132
Ga	20	20	19	19	19	19	19	19	20
Hf	8.35	8.50	7.91	7.85	7.65	7.73	8.10	7.74	3.20
Mo	1.14	1.22	0.80	1.21	0.61	1.53	0.66	1.23	3.0
Nb	18	18	21	21	20	21	22	20	22
Ni	196	194	309	308	316	331	317	331	315
Pb	4.8	4.9	20.2	19.9	19.4	21.2	16.9	20.5	20.0
Rb	48	53	52	53	53	52	22	53	57
Sc	25	24	24	23	23	23	24	24	2.0
Sr	617	629	3004	3084	2973	2840	2417	2328	2990
Ta	1.32	1.31	1.25	1.25	1.23	1.24	1.30	1.26	3.0
Th	9.1	9.8	15.5	15.6	15.0	15.6	16	15.3	21.0
U	1.8	1.8	3.9	3.9	3.6	3.9	3.7	3.8	3.0
V	334	319	209	226	191	230	183	215	183
Y	23	23	22	22	21	22	22	22	22
Zn	99	98	99	97	98	99	102	103	---
Zr	321	324	307	307	297	305	317	303	298
La	52.3	52.0	103.6	104.3	100.0	103.2	97.4	98.4	109
Ce	101.7	100	205.7	208.5	198.9	205.7	196.4	197.9	190
Pr	11.1	11.1	25.0	25.4	24.4	25.0	23.5	24.1	---
Nd	38.6	38.5	96.1	97.0	93.1	96	88.9	91.6	88
Sm	6.46	6.38	14.84	14.95	14.22	14.82	14.04	14.50	15.5
Eu	1.91	1.85	3.72	3.78	3.60	3.74	3.61	3.66	---
Gd	5.66	5.48	9.20	9.27	9.01	9.18	8.93	9.11	---
Tb	0.79	0.80	1.01	1.02	0.99	1.02	0.98	0.99	---
Dy	4.51	4.31	4.69	4.65	4.52	4.62	4.65	4.74	6.6
Ho	0.84	0.84	0.80	0.78	0.76	0.77	0.79	0.78	---
Er	2.29	2.30	1.96	1.92	1.89	1.91	1.96	1.93	---
Tm	0.33	0.32	0.26	0.25	0.26	0.25	0.27	0.26	---
Yb	1.94	1.94	1.58	1.53	1.52	1.57	1.64	1.55	2.20
Lu	0.29	0.28	0.23	0.22	0.23	0.22	0.25	0.22	---
$^{87}Sr/^{86}Sr_m$	0.703434				0.704007				
$^{87}Sr/^{86}Sr_i$	0.703430				0.704006				
$^{143}Nd/^{144}Nd_m$	0.512928				0.512856				
$^{143}Nd/^{144}Nd_i$	0.512928				0.512856				
εNd	5.71				4.31				
$^{206}Pb/^{204}Pb$	18.785				18.929				
$^{207}Pb/^{204}Pb$	15.522				15.559				
$^{208}Pb/^{204}Pb$	38.369				38.483				

Note: All major element data expressed as raw weight % oxide; FeO* is total Fe; trace element concentrations in ppm. N.d. = not determined. Samples with an asterisk are from Brueseke *et al*. (2023). Sr-Nd data reported as measured and initial values, age corrected to 1 Ma.

Table 3.1 (continued on next page): Results from geochemical analysis of MRVF rocks. V#1 = volcano #1; V#2 = volcano #2 V#3 = volcano #3.

Sample	DEN20-5*	DEN20-6*	DEN20-7*	AB22-3	AB22-4
Unit	V#3	V#3	V#3	V#3	V#3
Type	Lava	Lava	Lava	Lava	Lava
Lat. N°	63.0553	63.0578	63.0547	63.0577	63.0589
Long. W°	-146.3132	-146.3132	-146.3110	-146.3046	-146.3045
SiO_2	56.78	56.31	56.89	56.49	56.51
TiO_2	0.95	0.96	0.95	0.95	0.95
Al_2O_3	16.60	16.69	16.64	16.50	16.59
FeO*	5.18	5.42	5.22	5.22	5.31
MnO	0.098	0.102	0.099	0.099	0.099
MgO	6.38	6.32	6.34	6.33	6.36
CaO	6.88	6.98	6.93	6.94	6.98
Na_2O	4.30	4.26	4.35	4.18	4.27
K_2O	1.69	1.62	1.67	1.67	1.62
P_2O_5	0.262	0.272	0.270	0.267	0.269
LOI	0.21	0.08	-0.19	0.61	0.10
Mg#	68.7	67.5	68.4	68.3	68.0
Ba	704	695	698	685	698
Cr	219	210	215	210	212
Cs	0.44	0.48	0.32	n.d.	0.00
Cu	45	42	43	48	45
Ga	18	18	18	18	18
Hf	3.59	3.71	3.55	2.5	2.0
Mo	1.62	1.67	1.62	2.0	1.0
Nb	27	25	25	27	25
Ni	149	140	146	145	143
Pb	6.3	6.2	6.2	3.0	4.0
Rb	31	28	30	30	26
Sc	17	17	17	5.0	3.0
Sr	993	958	993	999	1002
Ta	1.61	1.58	1.61	2.0	1.0
Th	5.41	5.33	5.42	8.0	8.0
U	1.3	1.4	1.4	0.0	n.d.
V	129	139	136	128	136
Y	14	15	14	15	16
Zn	61	62	59	---	---
Zr	147	150	150	148	148
La	27.2	27.1	28.1	24	30
Ce	501	51.1	51.8	56	56
Pr	5.7	5.7	5.8	---	---
Nd	21	21.2	21.6	24	22
Sm	3.77	3.77	3.86	4.8	4.0
Eu	1.19	1.18	1.18	---	---
Gd	3.13	3.27	3.27	---	---
Tb	0.44	0.46	0.47	---	---
Dy	2.50	2.73	2.64	3.0	3.0
Ho	0.49	0.52	0.50	---	---
Er	1.32	1.46	1.43	---	---
Tm	0.20	0.21	0.20	---	---
Yb	1.27	1.31	1.27	1.30	1.30
Lu	0.19	0.19	0.19	---	---
$^{87}Sr/^{86}Sr_m$			0.703469		
$^{87}Sr/^{86}Sr_i$			0.703467		
$^{143}Nd/^{144}Nd_m$			0.512949		
$^{143}Nd/^{144}Nd_i$			0.512948		
εNd			6.12		
$^{206}Pb/^{204}Pb$			18.823		
$^{207}Pb/^{204}Pb$			15.54		
$^{208}Pb/^{204}Pb$			38.377		

Note: All major element data expressed as raw weight % oxide; FeO* is total Fe; trace element concentrations in ppm. N.d. = not determined. Samples with an asterisk are from Brueseke *et al*. (2023). Sr-Nd data reported as measured and initial values, age corrected to 1 Ma.

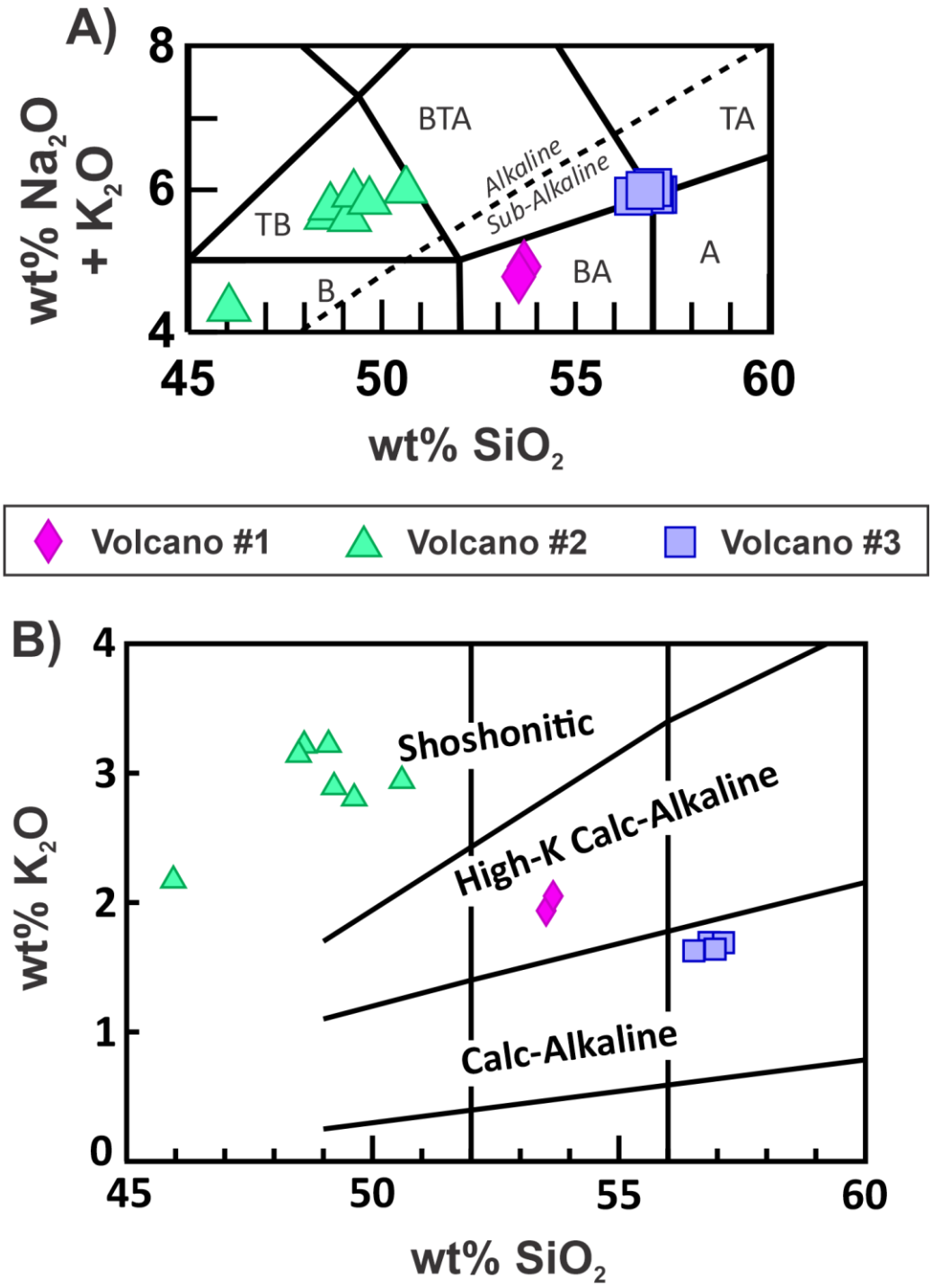

Figure 3.4: (A) Total alkalis vs. silica diagram after Le Bas et al. (1986) with subdivisions between alkalic and sub-alkalic magma series after Irvine and Baragar (1971). (B) K_2O vs. SiO_2 discrimination diagram after Peccerillo and Taylor (1976). B = basalt, TB = trachybasalt, BTA = basaltic trachyandesite, BA = basaltic andesite, TA = trachyandesite, A = andesite.

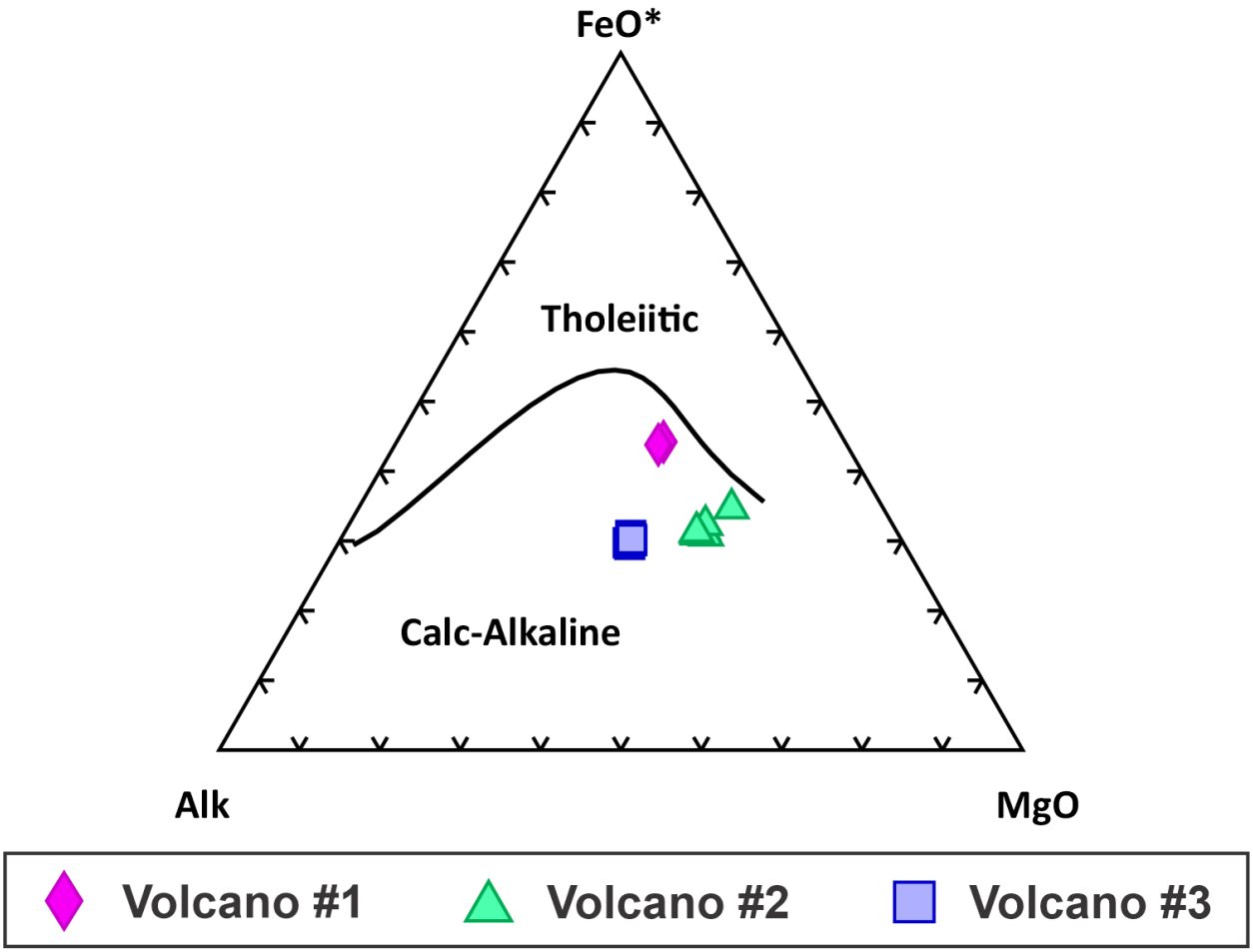

Figure 3.5: AFM discrimination diagram after Irvine and Barager (1971).

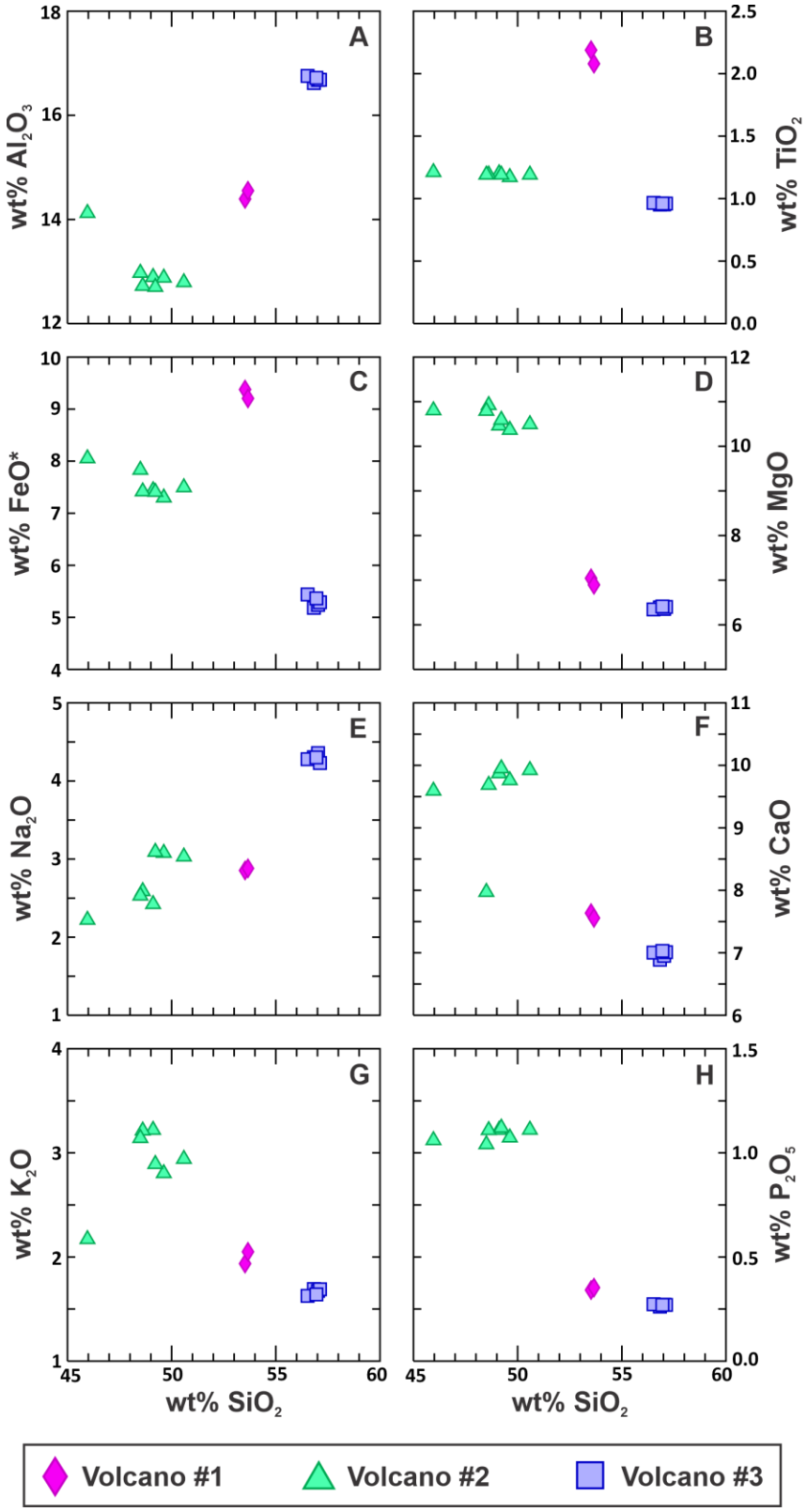

Figure 3.6: Harker diagrams illustrating major element variations with wt% SiO_2.

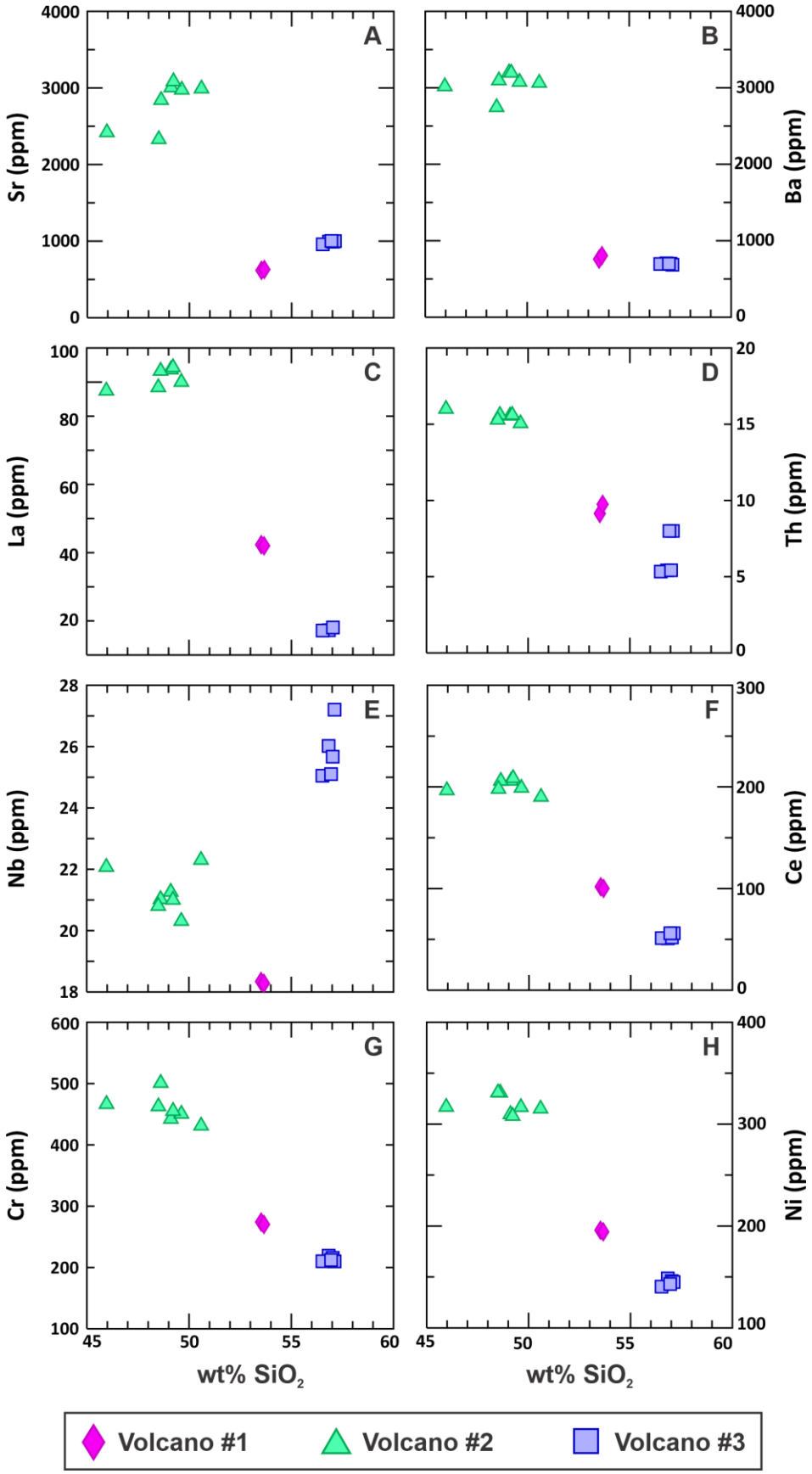

Figure 3.7: Harker diagrams illustrating select MRVF trace element variations with wt% SiO_2.

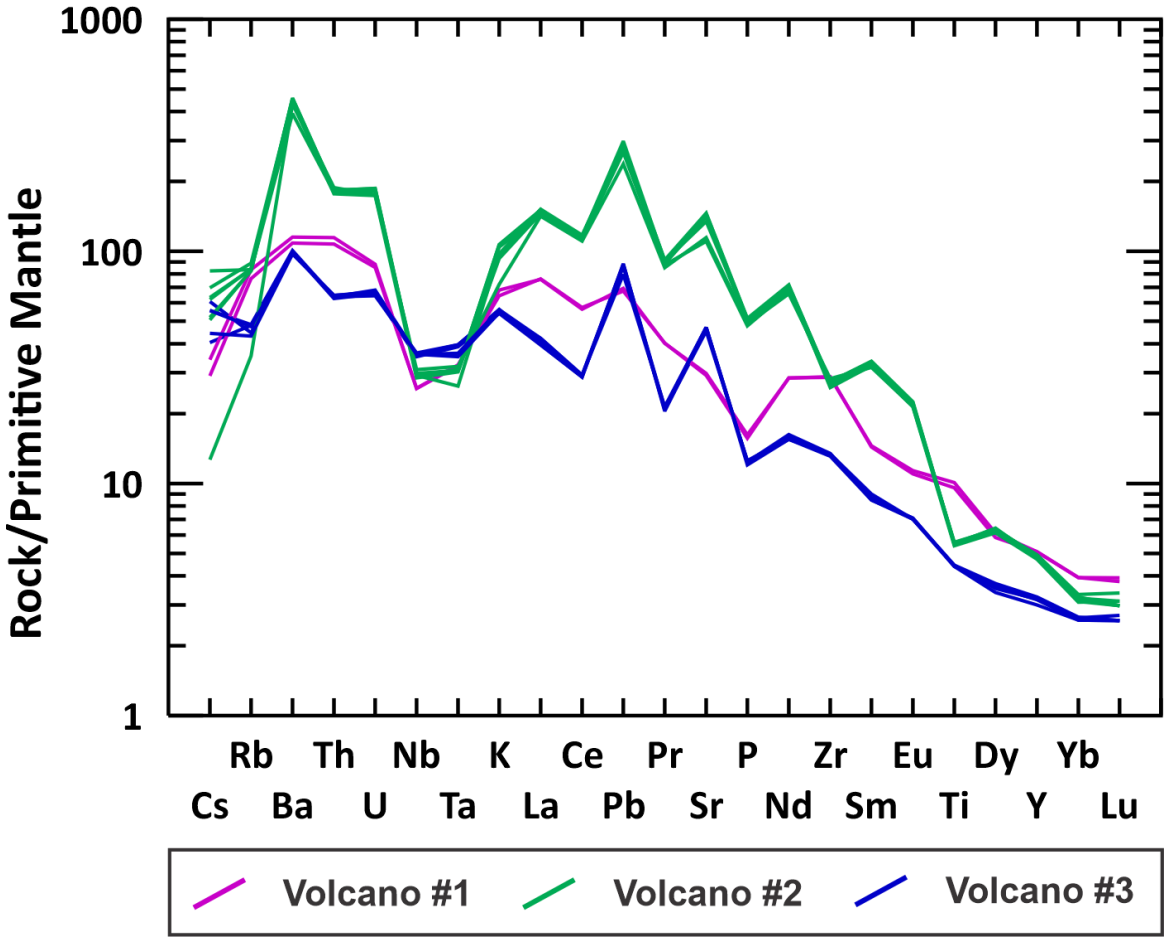

Figure 3.8: Primitive mantle-normalized (Sun and McDonough, 1989) trace element variations of MRVF rocks.

Sr-Nd-Pb Radiogenic Isotope Results

Figures 3.8 to 3.12 illustrate the $^{87}Sr/^{86}Sr_i$, εNd_i, $^{206}Pb/^{204}Pb$, $^{207}Pb/^{204}Pb$, and $^{208}Pb/^{204}Pb$ variations observed in MRVF samples from volcano #1, volcano #2, and volcano #3. MRVF isotope ratios are provided in Table 3-1. Sr and Nd ratios are age-corrected to 1 Ma and are considered the initial ratios. Regional and local bedrock units are plotted for reference and are age-corrected to 1 Ma.

$^{87}Sr/^{86}Sr_i$ values range from 0.70343-0.70401 and εNd_i values range from 4.31 – 6.12 (Table 3-1). All MRVF volcanoes plot within the field for the Triassic Nikolai formation (Greene *et al*. 2008; 2009), the Jurassic Talkeetna arc (Clift *et al*. 2005; Rioux *et al*., 2007), and Canadian Terranes (Sampson *et al*., 1989). Volcano #1 and volcano #3 are isotopically similar and generally plot within the field for modern Aleutian and Wrangell Arc magmas (Preece 1997; Snyder and Hart 2007) (Figure 3.8). These volcanoes also plot within the field for the Siletzia terrane (Wells *et al*., 2014). Isotope data from Siletzia basalts are considered here as a proxy for the isotope (and chemical) characteristics of the Yakutat terrane, given their likely common origin (Wells *et al*., 2014) and lack of any published isotope or geochemical data from Yakutat basalts. Volcano #2 displays more radiogenic $^{87}Sr/^{86}Sr_i$ values and lower εNd_i values in comparison to other MRVF volcanoes and is similar to the Holocene, Buzzard Creek maar (Andronikov and Mukasa 2010; Figure 3.8).

MRVF $^{206}Pb/^{204}Pb$ values range from 18.785 – 18.929, $^{207}Pb/^{204}Pb$ from 15.522 – 15.559, and $^{208}Pb/^{204}Pb$ from 38.369 – 38.483 (Table 3-1, Figures 3.9 – 3.12). On a plot of $^{87}Sr/^{86}Sr_i$ vs. $^{206}Pb/^{204}Pb$, MRVF rocks form an array towards higher, more radiogenic $^{87}Sr/^{86}Sr_i$ and $^{206}Pb/^{204}Pb$ values (Figure 3.9). All MRVF rocks plot within the field for < 5 Ma Wrangell Arc magmas and generally within the field for modern Aleutian Arc magmas (Figure 3.9). Volcano

#2 displays more radiogenic $^{206}Pb/^{204}Pb$ values in comparison to volcano #1 and volcano #3. Moreover, volcano #2' plots generally within the field for the Triassic Nikolai Greenstone and is similar to Buzzard maar. Volcano #1 and volcano #3 plot generally within the fields for Siletzia terrane and the <ca. 30 Ma Chisana lavas of the Wrangell arc (Berkelhammer 2017).

On a plot of $^{207}Pb/^{204}Pb$ vs. $^{206}Pb/^{204}Pb$, MRVF volcanoes form an array towards more radiogenic $^{207}Pb/^{204}Pb$ and $^{206}Pb/^{204}Pb$ values (Figure 3.10). Volcano #1 and volcano #3 plot within the field for Aleutian Arc magmas and Chisana lavas. Volcano #2 and volcano #3 plot within the field for <5 Ma Wrangell Arc magmas. Volcano #2 displays the most radiogenic $^{207}Pb/^{204}Pb$ and $^{206}Pb/^{204}Pb$ values and plots within the field for Nikolai Greenstone and Gravina-Nutzotina-Kahiltna strata (Aleinikoff *et al.* 1987; 2000). All volcanoes plot within or along the edge for the Siletzia terrane endmember.

On a plot of $^{208}Pb/^{204}Pb$ vs. $^{206}Pb/^{204}Pb$, MRVF rocks form an array towards more radiogenic ^{208}Pb and ^{206}Pb values (Figure 3.11). All MRVF rocks plot within the fields for modern Aleutian and Wrangell Arc magmas, Siletzia terrane, and Triassic Nikolai Greenstone. Volcano #1 and volcano #3 overlap with the most radiogenic portion of the Pacific MORB field. Volcano #2 is the most radiogenic and plots within the field for Gravina-Nutzotina-Kahiltna strata while volcano #3 plots along the edge of this field.

Figure 3.9 (next page): $^{87}Sr/^{86}Sr$ vs. εNd for three MRVF samples and two Buzzard Creek Maar samples. MRVF data are age-corrected to the 1 Ma based on $^{40}Ar/^{39}Ar$ geochronology reported in Brueseke *et al*. (2023). The fields of reference data are age-corrected to 1 Ma. εNd was calculated using $^{143}Nd/^{144}Nd = 0.512630$ and $^{147}Sm/^{144}Nd = 0.1960$ for CHUR (Bouvier *et al*., 2008). Mantle reservoirs are from Stracke (2012). Fields for reference data are from: Aleinikoff *et al*. (1987; 2000), Andronikov and Mukasa (2010), Berkelhammer (2017), Chan *et al*. (2012), Chauvel and Blichert-Toft (2001), Clift *et al*. (2005), Ciborowski *et al*. (2020), Cole and Stewart (2009), Greene *et al*. (2008; 2009), Hyeong *et al*. (2011), Jicha *et al*. (2004), Lassiter *et al*. (1995), McLennan *et al*. (1990), Plank and Langmuir (1998), Preece (1997), Rioux *et al*. (2007), Samson *et al*. (1989), Snyder and Hart (2007), Von Drach *et al*. (1986), White *et al*. (1987), Wirth *et al*. (2002). BSE = bulk silicate earth, DMM = depleted mid-ocean ridge basalt mantle, PREMA = prevalent mantle, EMI = enriched mantle I, EMII = enriched mantle II, HIMU = high μ ($^{238}U/^{204}Pb$) mantle, NHRL = Northern Hemisphere Reference Line; Y-T = Yukon-Tanana Terrane.

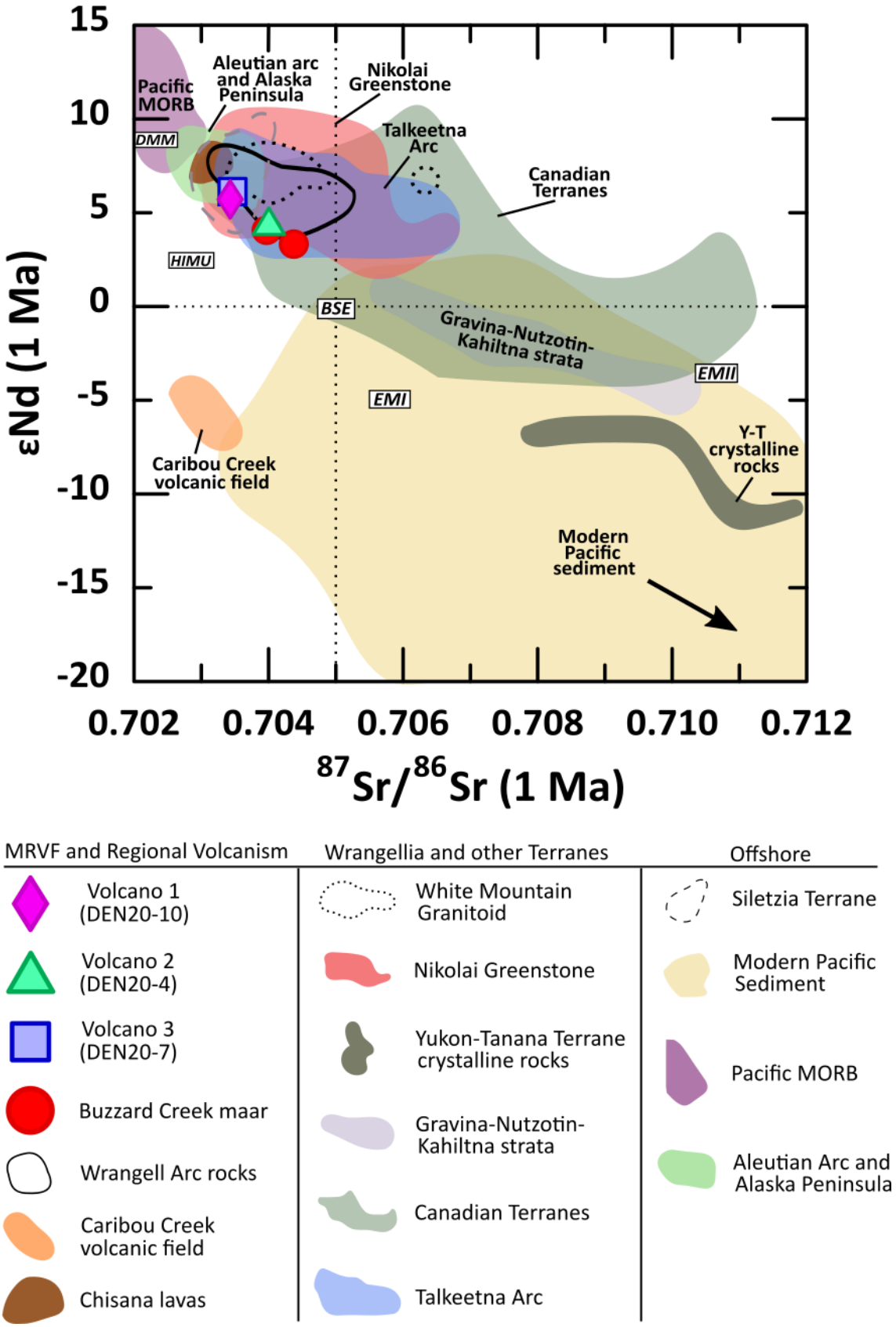
15
10
5
0
-5
-10
-15
-20
εNd (1 Ma)
0.702
0.704
0.706
0.708
0.710
0.712
87Sr/86Sr (1 Ma)
Pacific MORB
Aleutian arc and Alaska Peninsula
Nikolai Greenstone
Talkeetna Arc
Canadian Terranes
DMM
HIMU
BSE
EMI
EMII
Gravina-Nutzotin-Kahiltna strata
Caribou Creek volcanic field
Y-T crystalline rocks
Modern Pacific sediment
MRVF and Regional Volcanism
Volcano 1 (DEN20-10)
Volcano 2 (DEN20-4)
Volcano 3 (DEN20-7)
Buzzard Creek maar
Wrangell Arc rocks
Caribou Creek volcanic field
Chisana lavas
Wrangellia and other Terranes
White Mountain Granitoid
Nikolai Greenstone
Yukon-Tanana Terrane crystalline rocks
Gravina-Nutzotin-Kahiltna strata
Canadian Terranes
Talkeetna Arc
Offshore
Siletzia Terrane
Modern Pacific Sediment
Pacific MORB
Aleutian Arc and Alaska Peninsula

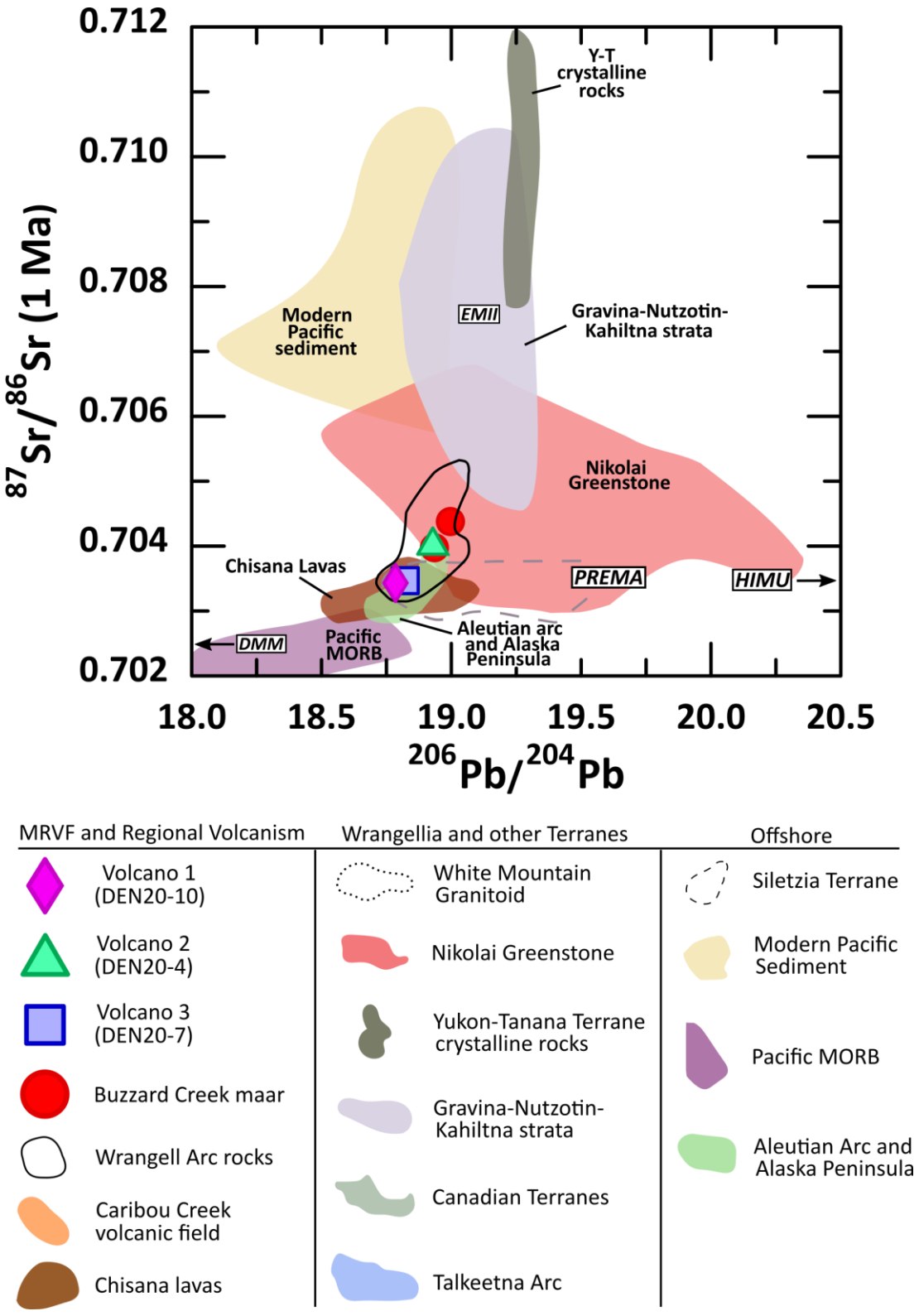

Figure 3.10: $^{87}Sr/^{86}Sr$ vs. $^{206}Pb/^{204}Pb$ for three MRVF samples. Fields of reference data are from the same citations as Figure 3.4.

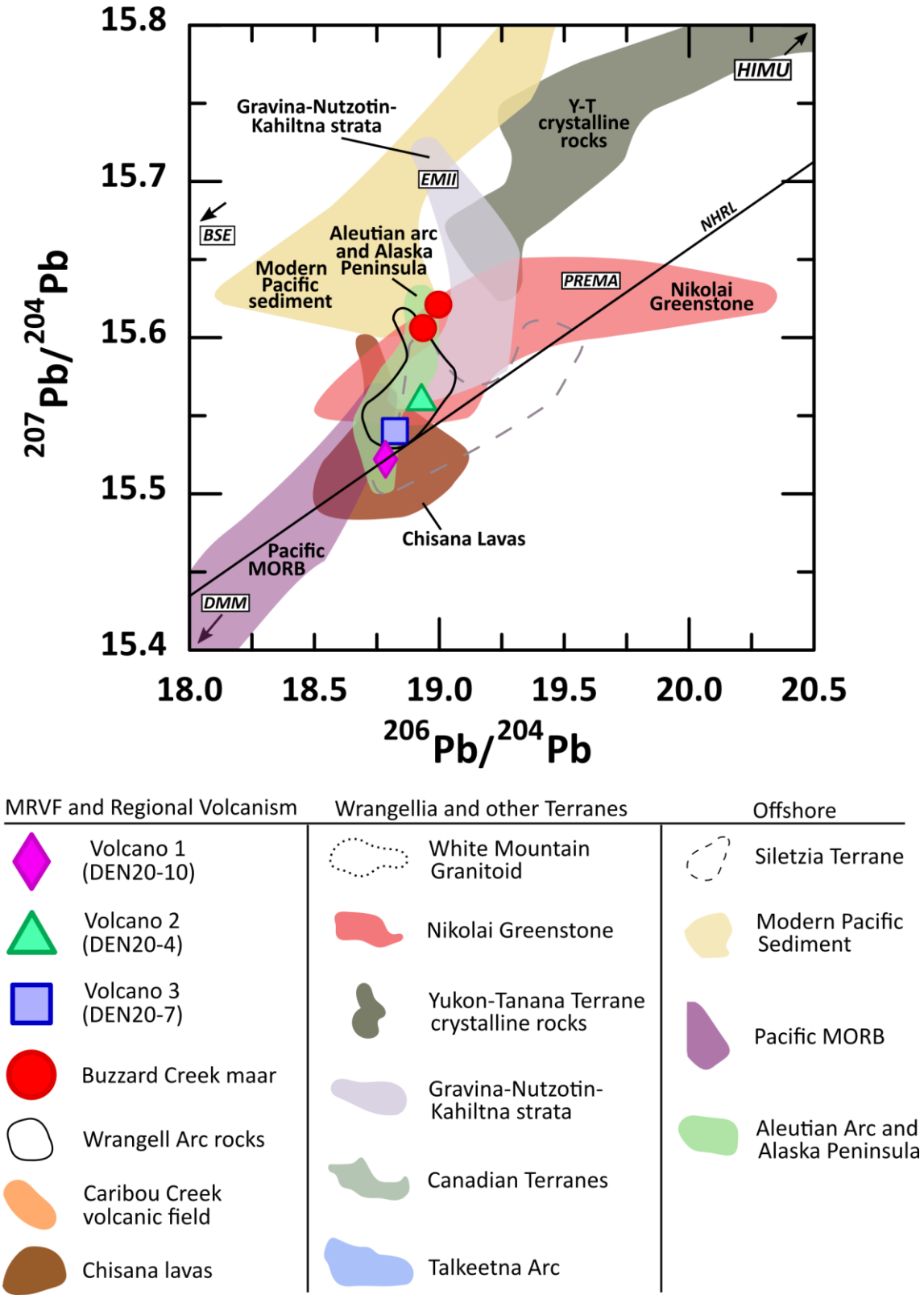

Figure 3.11: $^{207}Pb/^{204}Pb$ vs. $^{206}Pb/^{204}Pb$ for three MRVF samples. Fields of reference data are from the same citations as Figure 3.4.

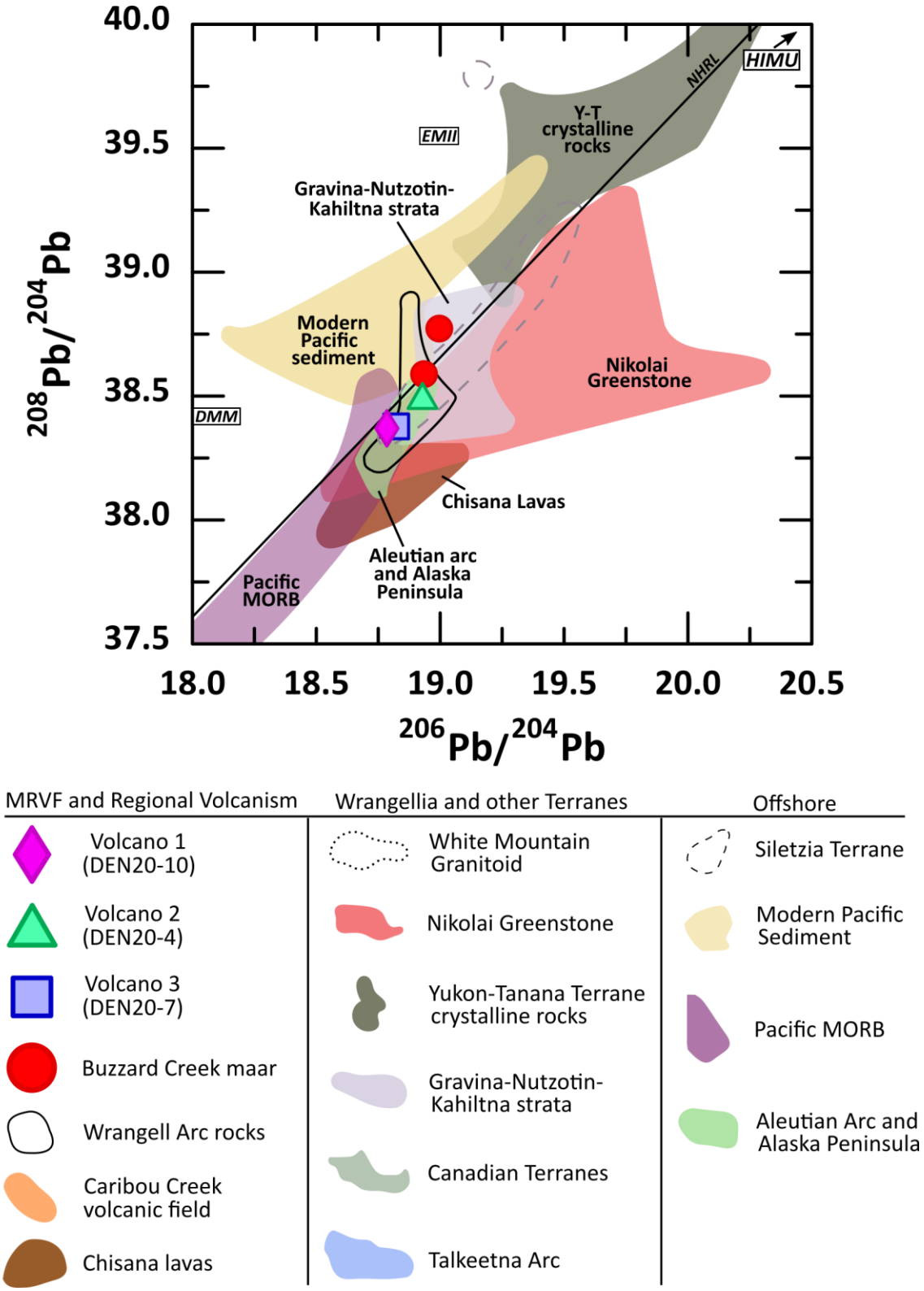

Figure 3.12: $^{208}Pb/^{204}Pb$ vs. $^{206}Pb/^{204}Pb$ for three MRVF samples. Fields of reference data are from the same citations as Figure 3.4.

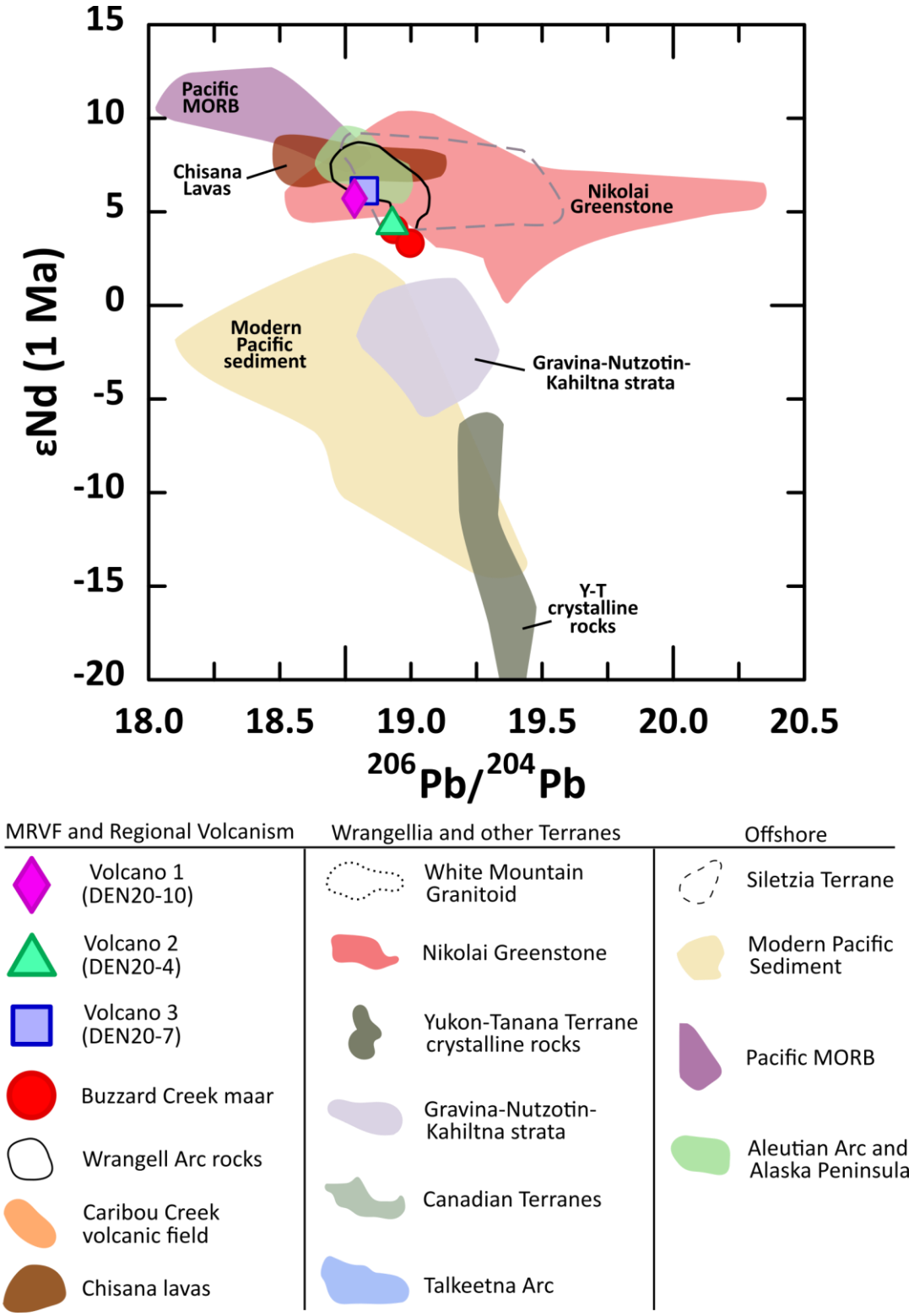

Figure 3.13: εNd vs. $^{206}Pb/^{204}Pb$ for three MRVF rocks. Fields of reference data are from the same citations as Figure 3.4.

Mg-B Stable Isotope Results

Rock samples from the MRVF have δ^{26}Mg values that range from -0.20 to -0.29 (± 0.064‰, 2 S.D.; Figure 3.14; Table 3.2); Jumbo Dome has a δ^{26}Mg value of -0.22 (± 0.064‰, 2 S.D.); Sonya Creek volcanic field samples range from -0.17 to -0.36 (± 0.050‰, 2 S.D.); and Mt. Drum has a δ^{26}Mg of -0.24 (± 0.064‰, 2 S.D.). Generally, all samples are isotopically similar to primitive mantle (-0.25 ± 0.04‰; Teng, 2017), with one sample from the Sonya Creek volcanic field displaying a lower δ^{26}Mg value than the primitive mantle (-0.36; sample SB15-39). All samples also fall within the isotopic range of continental arc basalts and island arc basalts (Teng et al. 2016; Li et al. 2017; Brewer et al. 2018). No trends between wt% SiO_2 and δ^{26}Mg are observed for the sample suite (Figure 3.15A). On the plot of wt% MgO vs. δ^{26}Mg, no trends are observed for our sample suite; however, samples from the SCVF, volcano #1, and volcano #3 form an array with decreasing δ^{26}Mg values as wt% MgO increases (Figure 3.15B).

δ^{11}B values of MRVF rock samples range from -8.02 to -5.03 (± 0.19-0.14‰, 2 S.D.; Figure 3.16; Table 3.2); Jumbo dome has a δ^{11}B value of -9.6 (± 0.25‰, 2 S.D.), Sonya Creek volcanic field samples have δ^{11}B values ranging from -10.5 to -7.06 (± 0.33 to 0.08‰, 2 S.D), and Mt. Drum has a δ^{11}B of -6.2 (± 0.1‰, 2 S.D.). Volcano #1, volcano #2, and Mt. Drum are isotopically similar to the depleted mantle (-7.1 ± 0.9; Marshall *et al*., 2017), although sample DEN20-13 from volcano #2 has a lower δ^{11}B while Mt. Drum is slightly more isotopically positive in comparison to the depleted mantle. Volcano #3 is more isotopically positive than the depleted mantle and overlaps with the most negative δ^{11}B values of altered oceanic crust. Jumbo Dome and a sample from the Sonya Creek volcanic field are more isotopically negative than the depleted mantle. Jumbo Dome, the SCVF, and volcano #1 and #2 also occupy similar B isotopic space to OIBs (Walowski *et al*., 2021).

Sample	Location	δ^{26}Mg (‰)	2 S.D.	δ^{25}Mg (‰)	2 S.D.	δ^{11}B (‰)	2 S.D.	B (ppm)
DEN20-10	V#1	-0.25	0.064	-0.13	0.038	-6.34	0.15	1.24
DEN20-4	V#2	-0.20	0.064	-0.10	0.038	-6.92	0.14	1.11
DEN20-13	V#2	-0.29	0.064	-0.15	0.038	-8.02	0.19	0.5
DEN20-7	V#3	-0.26	0.064	-0.13	0.038	-5.03	0.15	1.97
05JDDS02	Jumbo Dome	-0.22	0.064	-0.11	0.038	-9.6	0.25	2.01
SB15-31	SCVF	-0.17	0.050	-0.10	0.041	-7.06	0.16	2.97
SB15-39	SCVF	-0.36	0.050	-0.20	0.041	-9.97	0.08	0.85
15JB25LA	SCVF	-0.29	0.050	-0.14	0.041	-10.52	0.33	1.4
73ARh21	Mt Drum	-0.24	0.064	-0.13	0.038	-6.2	0.1	0.43

Table 3.2: Results from Mg and B isotope analysis on MRVF, Jumbo Dome, and Wrangell Arc rocks.

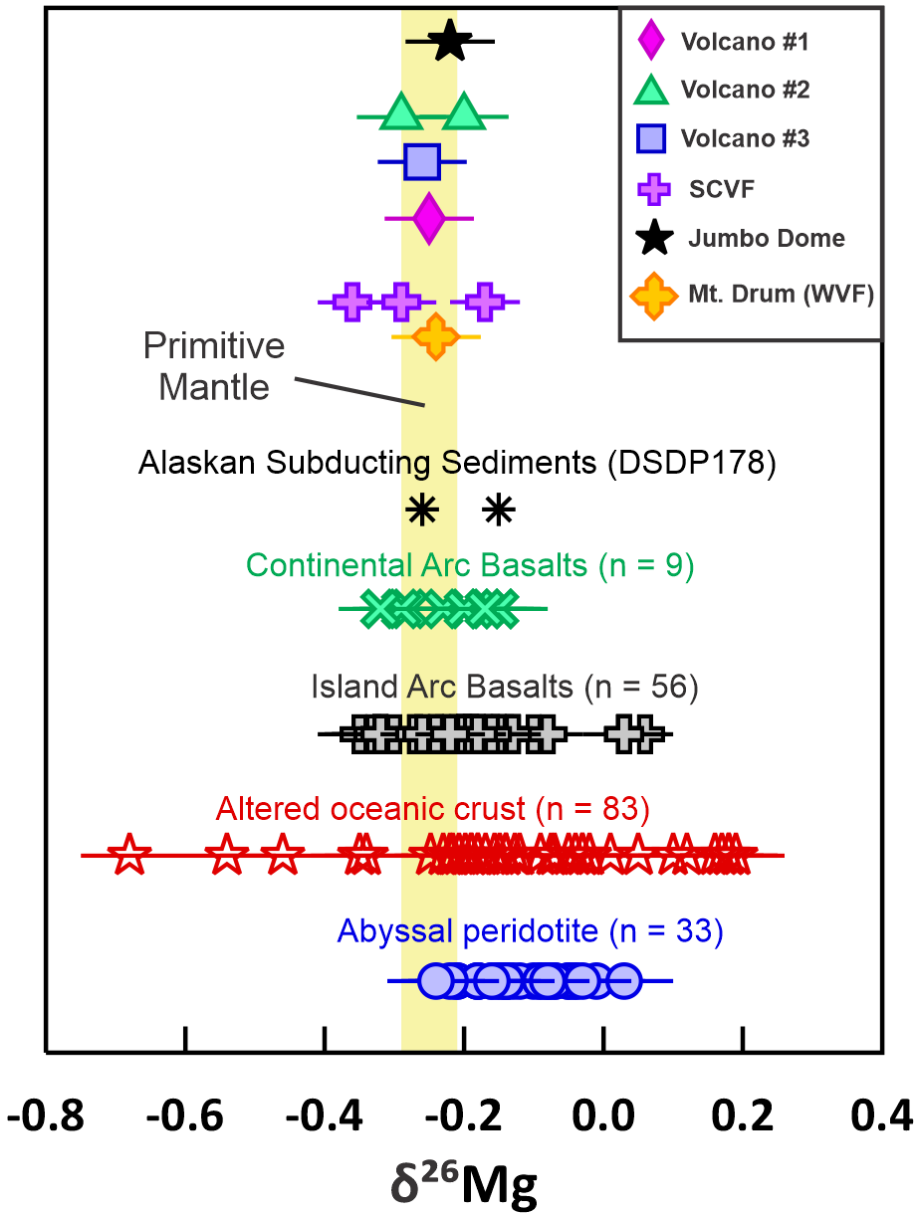

Figure 3.14: Magnesium isotope composition of MRVF, Jumbo Dome, and Wrangell arc rocks compared to potential reservoirs. Data sources are as follows: primitive mantle (Teng *et al*., 2010; Teng 2017), subducting Alaskan sediments (Hu *et al*., 2017), altered oceanic crust (Huang *et al*., 2015; 2018; Zhong *et al*., 2017), continental arc basalts (Brewer *et al*., 2018), island arc basalts (Teng *et al*., 2016; Li *et al*., 2017), and abyssal peridotites (Liu *et al*., 2017). Modified from Zhang *et al*., (2022). SCVF = Sonya Creek volcanic field; WVF = Wrangell volcanic field. Error bars represent the 2 S.D. for all samples. Yellow bar represents the Primitive Mantle.

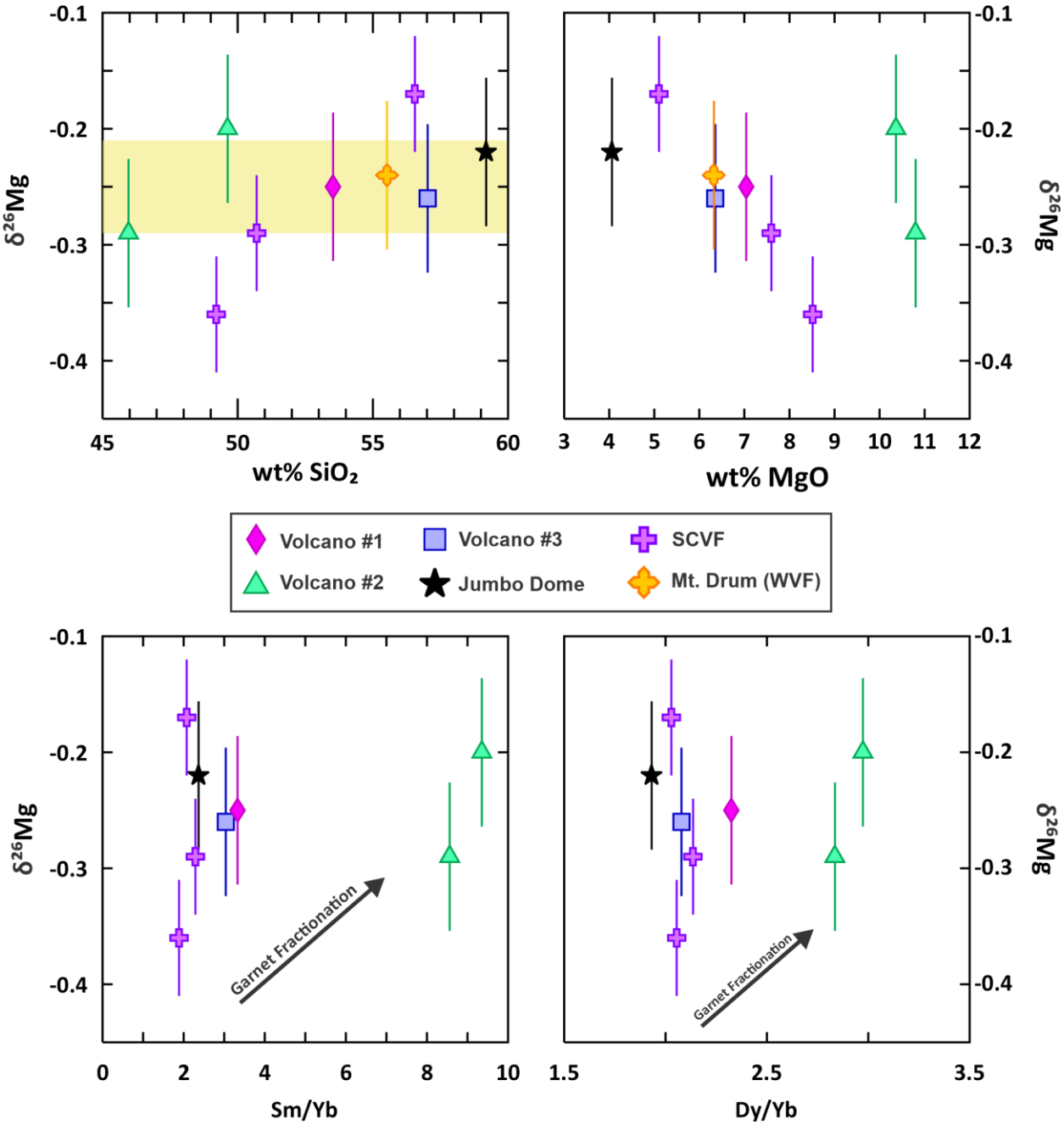

Figure 3.15: (A) Variation of δ^{26}Mg with wt% SiO_2. The yellow bar represents the primitive mantle composition based on peridotite xenoliths (δ^{26}Mg = -0.25 ± 0.04‰) from Teng *et al.* (2010). (B) Variation of δ^{26}Mg with wt% MgO. (C) and (D) variation of δ^{26}Mg with Sm/Yb and Dy/Yb ratios, modified from Brewer *et al.* (2018). Error bars represent the 2 S.D. for all samples.

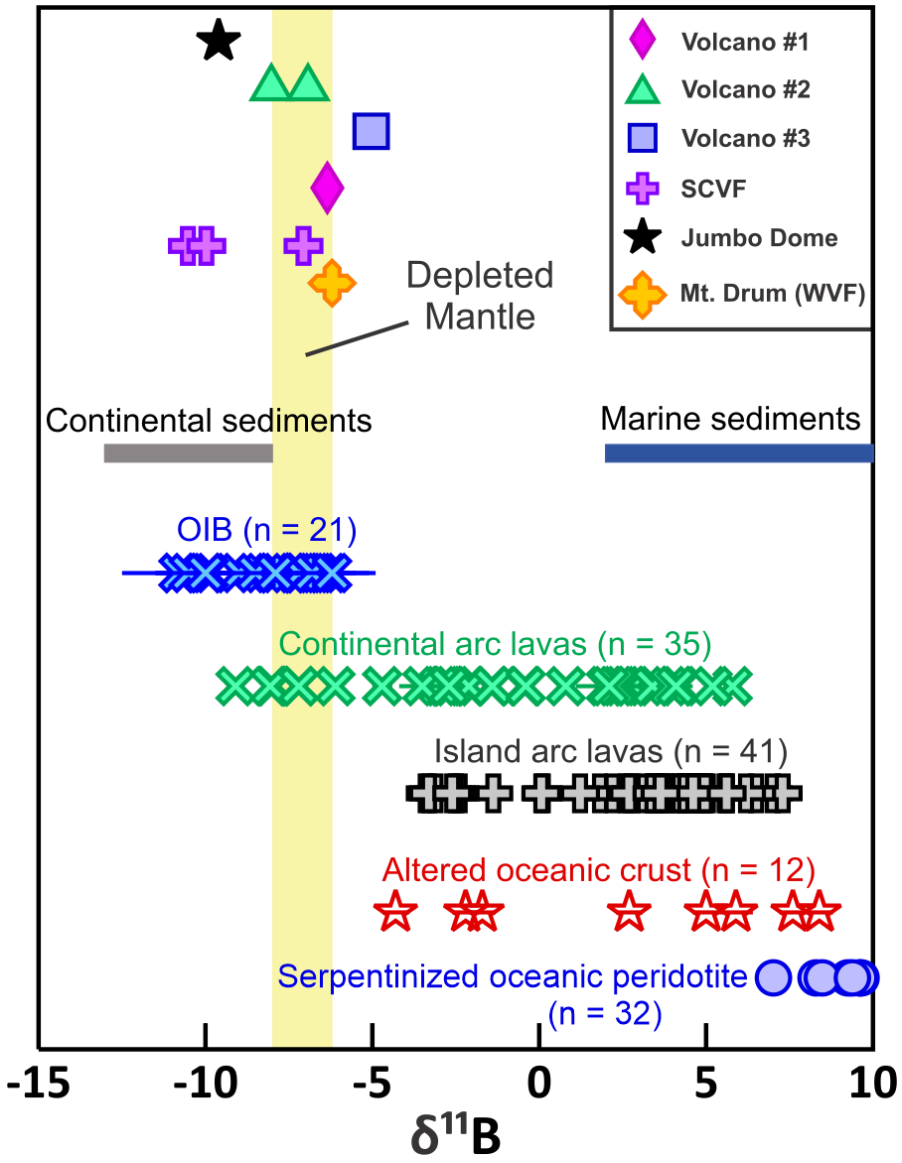

Figure 3.16: Boron isotope composition of MRVF, SCVF, Jumbo Dome, and Wrangell arc rocks compared to potential isotopic reservoirs. Data sources are as follows: depleted mantle (Marshall *et al*., 2017), continental and marine sediments (De Hoog and Savov, 2018 and references therein), altered oceanic crust (Smith *et al*., 1995), continental arc lavas (Rosner *et al*., 2003; Leeman *et al*., 2004; Tonarini *et al*., 2007), island arc lavas (Ishikawa and Nakamura, 1994; Ishikawa and Tera, 1997; 1999; Ishikawa *et al*., 2001; Moriguti *et al*., 2004), Ocean island basalts (Walowski *et al*., 2021), and serpentinized oceanic peridotites (Spivack and Edmond, 1987; Boschi *et al*., 2008; Harvey *et al*., 2014). SCVF = Sonya Creek volcanic field; WVF = Wrangell volcanic field. Error bars represent the 2 S.D. for all samples.

Chapter 4 - Discussion

The Role of Crustal Contamination on the Trace Element Geochemistry and Radiogenic Isotopic Signature of MRVF Magmas

One of the goals of this research is to constrain the source of MRVF magmas; however, volcano #2 and #3 display evidence of crustal contamination observed in both the field and microscopic scale (e.g., granitoid xenoliths; Figure 3.2 and Figure 3.3). Therefore, any potential influence of crustal contamination on the geochemical and Sr-Nd-Pb isotopic signatures of MRVF magmas must be investigated before constraining their sources of MRVF.

Assimilation and Fractional Crystallization Models

The assimilation and fractional crystallization (AFC) equation of DePaolo (1981) was used to simulate the effect of crustal contamination and fractional crystallization on the trace element geochemistry of MRVF magmas. The results from assimilation and fractional crystallization modeling are presented in Figure 3.1 and Table 3.1. For these calculations, a primitive Wrangell Arc basalt (SB15-39) described in Berkelhammer et al. (2019) was used as a proxy for a regional mantle wedge-derived melt with a crystallizing assemblage of olivine + clinopyroxene + plagioclase + magnetite. An ~35 Ma granitoid described in Green *et al*. (2008) (N Hwy TP) along with a Nikolai Greenstone sample (Green *et al*. 2008) were selected to represent regional contaminants due to their proximity to volcano #2 and #3. A Cretaceous-aged granitoid (RS91-8A) from northern Nevada was used as an additional contaminant to serve as a proxy for a typical granitoid geochemistry like the Cretaceous granitoids that are present across south-central Alaska that reflect prior arc volcanism (Brown *et al*., 2018; Manselle et al., 2020). Two MRVF rocks, one from volcano #2 and one from volcano #3, were selected for comparison with model results. DEN20-13 from volcano #2 was selected to represent the most primitive

MRVF magmatic product for comparison with model calculations. Sample DEN20-7 from volcano #3 was selected due to the availability of Sr-Nd-Pb radiogenic isotopic data reported in this study. For all models in Figure 3.1, the F value (% of liquid magma remaining) is 0.8 and the r values (mass assimilant / mass crystallized) are 0.01, 0.05, and 0.1. Bulk partition coefficient values (D) are shown in Table 4.1.

The AFC modeling indicates that fractional crystallization and assimilation of the local North Highway granitic pluton (N Hwy TP), Nikolai Greenstone, and the granitic crustal proxy do not sufficiently change the trace element geochemistry of a primitive mantle-derived melt to replicate the values observed in volcano #2 and volcano #3. Although xenoliths are found in rock samples from volcano #2 and #3, these were likely incorporated during late-stage ascent of their magmas and had minimal effect on the trace element geochemistry of volcano #2 and #3 magmas.

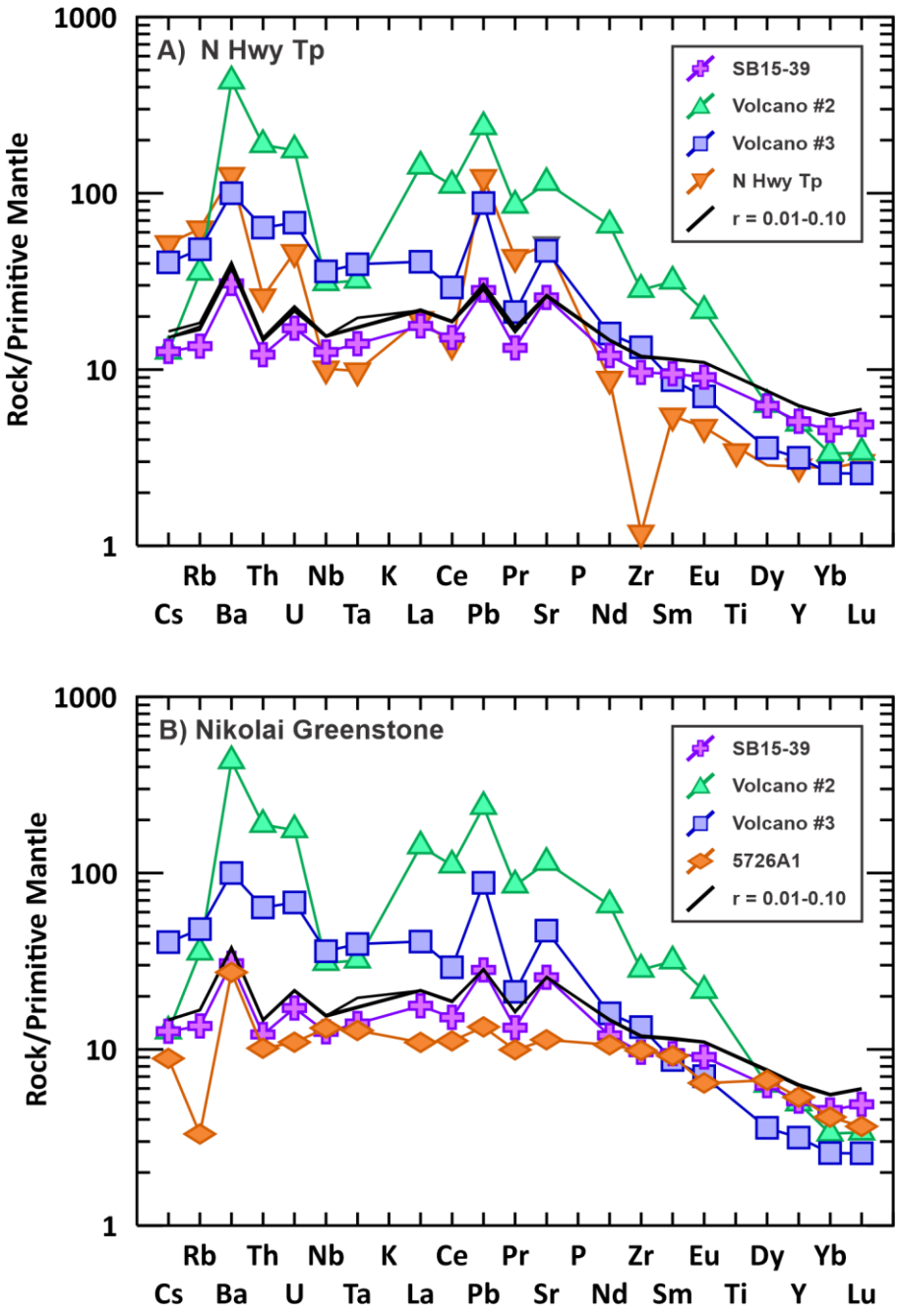

Figure 4.1: Results from AFC modeling (after DePaolo 1981) between a primitive Wrangell Arc basalt (SB15-39) and potential regional contaminants (A and B). SB15-39 data is from Berkelhammer (2017) and Nikolai Greenstone (5726A1) data is from Greene et al. (2008).

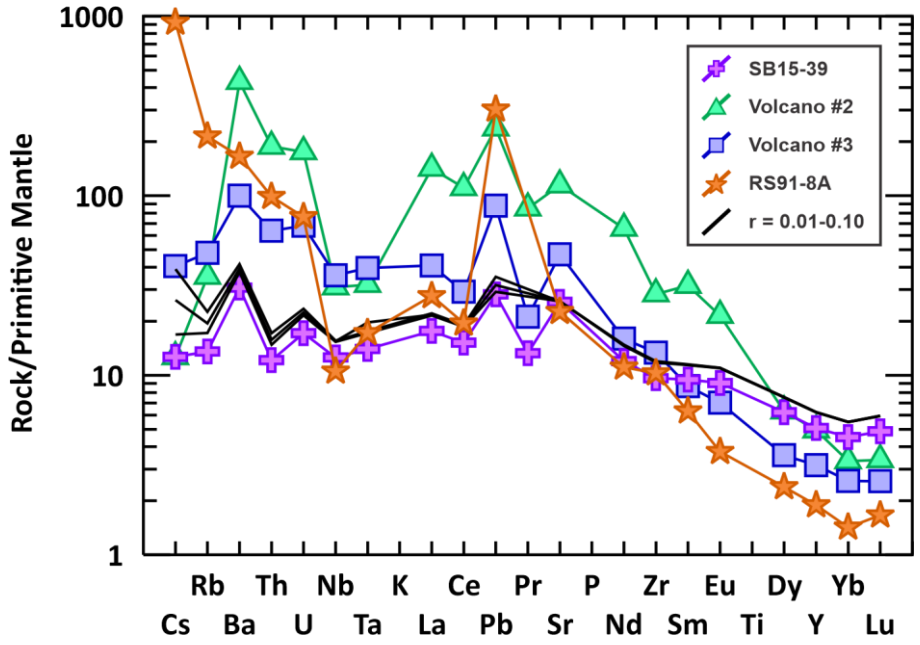

Figure 4.2: Results from AFC modeling (after DePaolo 1981) between a primitive Wrangell Arc basalt (SB15-39) and RS91-8A (a Cretaceous granitoid from Nevada as a proxy for Mesozoic granitoids in south-central Alaska). SB15-39 data is from Berkelhammer et al. (2019) and RS91-8A data is from Brown *et al.* (2018).

Name	SB15-39	DEN20-13	DEN20-7	RS91-8A	N Hwy Tp	5726A1	
Location	WVF	Volcano #2	Volcano #3	Santa Rosa-Calico volcanic field	Proximal to volcano #2	Nikolai Greenstone	Bulk Partition Coefficient
	Source			Contaminant	Contaminant	Contaminant	
Cs	0.1	0.1	0.32	7.3	0.41	0.07	0.352
Rb	8.6	22.5	30.5	128	39.9	2.1	0.067
Ba	215	3016	698	1130	884	191	0.146
Th	1.03	15.99	5.42	8.4	2.2	0.86	0.183
U	0.36	3.68	1.43	1.6	0.97	0.23	0.011
Nb	8.94	22.07	25.6	12	7.19	9.4	0.10
Ta	0.57	1.3	1.61	0.7	0.4	0.52	0.091
La	12.1	97.4	28.0	20	13.23	7.52	0.124
Ce	26.9	196	51.8	39	24.55	19.8	0.097
Pb	2.00	16.9	6.24	21.5	8.74	0.95	0.944
Pr	3.66	23.48	5.84	N.R.	11.9	2.74	0.098
Sr	540	2417	992	435	1077	239	0.961
Nd	16.2	88.9	21.6	15	11.9	14.3	0.133
Zr	107	317	149	95	13	110	0.104
Sm	4.20	14.04	3.86	2.8	2.42	4.07	0.173
Eu	1.52	3.61	1.18	0.63	0.79	1.08	0.152
Dy	4.58	4.65	2.64	1.76	2.11	4.92	0.147
Y	23.1	22.4	14.3	10	12.8	24.3	0.101
Yb	2.23	1.64	1.27	0.8	1.36	2.03	0.141
Lu	0.36	0.25	0.19	0.123	0.22	0.27	0.118
Mineral Modes (%)	**Olivine**	**Clinopyroxene**	**Plagioclase**	**Oxide**			
	16.8	0.092	59	4			

Table 4.1: Results from AFC Modeling. WVF = Wrangell volcanic field. Mineral modes from Berkelhammer (2017). Trace element geochemistry references are as follows: SB15-39 (Berkelhammer 2017); RS91-8A (Brown *et al*., 2018); 5726A1 (Greene *et al*., 2008), DEN20-13 and DEN20-7 (Brueseke *et al*., 2023), N Hwy Tp (this study). N.R. = not reported.

Sr-Nd-Pb Binary Mixing Models

As mentioned previously, eroded sediment from the Insular terrane, Yukon-Tanana terrane, and Gravina-Nutzotin-Kahiltna sedimentary strata was likely subducted with the Yakutat microplate over the past 30 Ma and could contribute to mantle modification beneath the MRVF and influence the isotopic signature of MRVF magmas. Figure 4.3 displays results of binary mixing models that investigate the contributions of potential subduction inputs (e.g., subducted slab and sediments) to the mantle wedge and their relationship to MRVF rocks. Isotope ratios and elemental concentrations for each isotopic endmember are displayed in Table 4.2. The mantle wedge component is represented by the depleted mantle (M). Regional crustal rocks that may act as potential contaminants include the Triassic Nikolai Greenstone (N), Cretaceous Gravina-Nutzotin-Kahiltna sedimentary strata (K), and sediments eroded from the Cretaceous granitoids that intrude the Yukon-Tanana Terrane (Y). In addition, the accreted Jurassic Talkeetna Arc is located ~200 km southwest of the MRVF and may represent an additional source of crustal input. Additionally, the isotope compositions of the Siletzia terrane (S) are used as a proxy for potential Yakutat terrane contribution to MVRF magmatism. Modern Pacific sediment (PS) represents the bulk sediment composition from the Gulf of Alaska and serves as a modern analogue to potential subducted sediments (Plank and Langmuir, 2008). Sr and Pb concentrations of endmembers were adjusted following Berkelhammer (2017) to maintain the Sr/Pb ratio of GLOSS for Yukon-Tanana Terrane (Y), Siletzia terrane (S), Pacific Sediment (PS), Nikolai Greenstone (N), and Gravina-Nutzotin-Kahiltna strata (K). and the Sr/Pb ratio of the primitive mantle for the depleted mantle (M) endmember (Table 4.3).

The mixing curve between the depleted mantle (M) and Talkeetna Arc (T) does not pass through the MRVF $^{87}Sr/^{86}Sr_i$ and εNd_i data, suggesting that the Talkeetna Arc rocks are not a likely contaminant of MRVF magmas (Figure 4.3A).

Modern Pacific sediment from the Gulf of Alaska (Plank and Langmuir, 1998) does not form a viable mixing curve with depleted mantle in Sr, Nd, and Pb isotopic space, suggesting it does not represent a likely contamination endmember (Figure 4.3). In Figure 4.3A, the mix of Pacific sediment with depleted mantle is proximal to the MRVF array, requiring 1-5% sediment to generate the $^{87}Sr/^{86}Sr_i$ and εNd_i values of volcano #1, #2, and #3. In Figure 4.3B, the mixing curve between depleted mantle and Pacific sediment better aligns with the MRVF array, requiring a 1-3% sediment mixture to generate the $^{87}Sr/^{86}Sr_i$ and $^{206}Pb/^{207}Pb$ values of the MRVF. In contrast, the Pacific sediment endmember's $^{206}Pb/^{204}Pb$ value is not high enough to match the MRVF isotopic signature in ^{206}Pb-^{207}Pb isotopic space (Figure 4.3C). However, in Figure 4.3D, a plot of $^{208}Pb/^{204}Pb$ vs. $^{206}Pb/^{204}Pb$, the mixing curve between depleted mantle and Pacific sediment is parallel to the MRVF array but does not pass through the data.

Nikolai Greenstone extends to radiogenic values of $^{87}Sr/^{86}Sr_i$, $^{206}Pb/^{204}Pb$, and $^{208}Pb/^{204}Pb$ (Figure 3.8 to 3.12). The mixing curve between the depleted mantle endmember and Nikolai Greenstone in Figure 4.3A extends along the MRVF array, particularly for volcano #1 and #3, requiring 5-20% Nikolai input. However, in Pb-Pb isotope space, the mixing curves between depleted mantle and Nikolai Greenstone require much less mixing (e.g., <1% Nikolai contributing) to fit along the MRVF array (Figure 4.3C – and Figure 4.3D). This inconsistency in percent Nikolai contribution and in combination with the mixing curves not passing through the MRVF data suggests that the Nikolai Greenstone is likely not controlling the isotopic signature of MRVF magmas. Although volcanoes #2 and #3 erupted through Nikolai Greenstone, the

mixing curves presented here suggest that crustal contamination from this unit may not have been a significant influence on the isotopic signatures of these volcanoes and this is reflected by the AFC trace element modelling presented earlier that shows Nikolai contamination did not affect the geochemistry of MRVF magmas.

It is likely that crystalline basement rocks of the Yukon-Tanana terrane as well as the Gravina-Nutzotin-Kahiltna sedimentary strata were eroded and fluvially transported offshore where they were subsequently subducted and recycled into the mantle (Berkelhammer 2017 and references therein). Thus, bedrock samples from these basement terranes were used in mixing models to determine the influence of Yukon-Tanana terrane and Gravina-Nutzotin-Kahiltna strata on the isotopic composition of the mantle wedge and lavas. Mixing curves between depleted mantle and Yukon-Tanana terrane indicate that 0.5 – 1% Yukon-Tanana is required to produce $^{87}Sr/^{86}Sr_i$, εNd_i, and $^{206}Pb/^{204}Pb$ values similar to those of the MRVF (Figure 4.3A and Figure 4.3B). However, similar to the Pacific sediment endmember, the Yukon-Tanana terrane endmember's $^{206}Pb/^{204}Pb$ value is too low for the mixing curve to overlap MRVF values in $^{207}Pb/^{204}Pb$ vs. $^{206}Pb/^{204}Pb$ isotopic space (Figure 4.3C). This inconsistency persists in on the plot of $^{208}Pb/^{204}Pb$ vs. $^{206}Pb/^{204}Pb$ (Figure 4.3D), where the mixing curve between depleted mantle and Yukon-Tanana terrane approximately aligns with the MRVF with a Yukon-Tanana input between ~0.3 – 0.5%. Although samples from volcano #2 and #3 contain granitic xenoliths and quartz xenocrysts, these mixing curves suggest that any potential isotopic influence from a Paleozoic-Mesozoic granitic source on the isotopic composition of MRVF magmas is unlikely (similar to modelled AFC results).

Mixing curves between the Gravina-Nutzotin-Kahiltna sedimentary strata and depleted mantle (M) indicate that a 1 -3% Gravina-Nutzotin-Kahiltna contribution is approximately close

to the MRVF array on a plot of $^{87}Sr/^{86}Sr$ and εNd (Figure 4.3A), and a mix of 0.5 to ~1% Gravina-Nutzotin-Kahiltna sediment passes through the MRVF values on a plot of $^{206}Pb/^{204}Pb$ vs. $^{208}Pb/^{204}Pb$ (Figure 4.3D). However, the mixing curve on Figure 4.3C does not overlap with the data, suggesting that this end member is not a likely contaminant.

On Figure 4.3A, the Siletzia – depleted mantle mixing curve approximately replicates the $^{87}Sr/^{86}Sr_i$ and εNd_i values of volcano #1 and #3 at 5-20% Siletzia input, but volcano #2 has a more radiogenic $^{87}Sr/^{86}Sr$ composition than the Yakutat terrane endmember which indicates that Siletzia did not contribute to the isotopic composition of volcano #2. Furthermore, on plots of $^{207}Pb/^{204}Pb$ vs. $^{206}Pb/^{204}Pb$ and $^{208}Pb/^{204}Pb$ vs. $^{206}Pb/^{204}Pb$ (Figure 4.3C and Figure 4.3D)., much less Siletzia input (< 0.5%) is required to pass through the MRVF array for all three volcanoes. This discrepancy indicates that the Siletzia endmember, which is a proxy for the subducted Yakutat slab, may not have single handedly influenced MRVF isotopic compositions.

In summary, the mixing models indicate that no single endmember replicates the MRVF Sr-Nd-Pb isotopic signatures. Rather, the mantle beneath the MRVF may have been metasomatized by a combination of endmembers (e.g., a mixture of Siletzia basalts and modern pacific sediment which then mixed with the depleted mantle). However, additional modeling is necessary to test this. In conjunction with the AFC modeling, these binary mixing models suggest that the crustal xenoliths observed in volcano #2 and #3 are not a major contributor to their isotopic and geochemical composition.

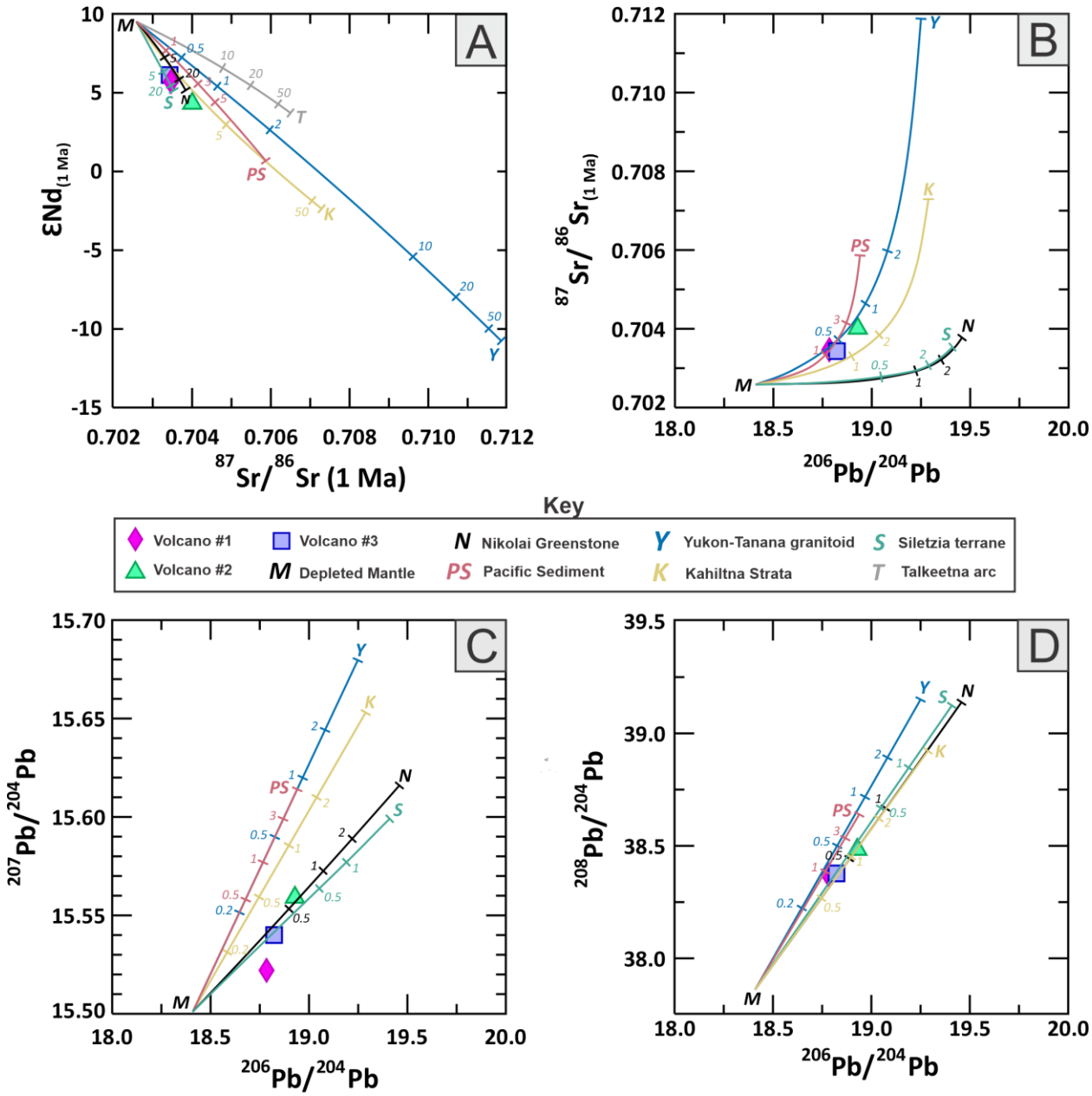

Figure 4.3: Results of binary mixing calculations between depleted mantle (M) and various endmembers, abbreviations for which are shown in the key. (A) εNd_i vs. $^{87}Sr/^{86}Sr_i$ (B) $^{87}Sr/^{86}Sr_i$ vs. $^{206}Pb/^{204}Pb$ (C) $^{206}Pb/^{204}Pb$ vs. $^{207}Pb/^{204}Pb$ (D) $^{206}Pb/^{204}Pb$ vs. $^{208}Pb/^{204}Pb$. References for isotopic endmember data given in Table 4-2 and 4-3.

Abbreviation	***M***	***Y***	***K***	***N***	***S***	***PS***	***T***
Endmember	Depleted Mantle[1]	Yukon-Tanana Granitoid[2]	Gravina-Nutzotina-Kahiltna Strata[3]	Nikolai Greenstone[4]	Siletzia (southern WA)[5]	Modern Pacific Sediment[6]	Talkeetna Arc[7]
$^{87}Sr/^{86}Sr$	0.702583	0.711856	0.707290	0.703844	0.703534	0.705874	0.706503
Sr (ppm)	9.8	277	175	239	496	289	112
εNd	9.51	-10.76	-2.37	5.31	5.14	0.67	3.71
Nd (ppm)	0.713	17.9	16.6	14.35	36.94	18.56	6.6
$^{206}Pb/^{204}Pb$	18.41	19.25	19.288	19.459	19.41	18.94	
$^{207}Pb/^{204}Pb$	15.501	15.68	15.653	15.616	15.599	15.614	
$^{208}Pb/^{204}Pb$	37.86	39.15	38.922	39.151	39.151	38.641	
Pb (ppm)	0.023	55.6	5.49	0.95	2.16	10.08	

Table 4.2: Isotope values for endmembers used in binary mixing calculations in Figure 4.3. [1]Isotope ratios from Chauvel and Blichert-Toft (2001), elemental concentrations from Salters and Stracke (2004); [2]Aleinikoff *et al*. (1987); [3]Aleinikoff *et al*. (2000); [4]Greene *et al*. (2008); [5]Chan *et al*. (2012); [6]Plank and Langmuir (1998) and Vervoort *et al*. (2011); [7]Rioux *et al*. (2007). Sr-Nd isotope ratios corrected to 1 Ma.

	PM[1]	***M***	***GLOSS[2]***	***Y***	***K***	***N***	***S***	***PS***
Sr (ppm)	21.1	9.8	327	277	175	239	496	289
Pb (ppm)	0.185	0.086	19.9	16.85	10.65	14.54	30.18	17.59
Sr/Pb	**114**	114	**16.43**	**16.43**	**16.43**	16.43	**16.43**	**16.43**

Table 4.3: Adjustment of Pb concentrations to maintain Sr/Pb ratios of PM and GLOSS. [1]PM values from Sun and McDonough (1989). [2]Gloss values from Plank and Langmuir (1998). Numbers in bold are to highlight relevant Sr/Pb ratios, and the adjusted Pb concentrations that maintain those ratios. Table adjusted from Berkelhammer (2017). Abbreviations are the same as in Table 4.2.

Potential Sources for MRVF Magmas

All volcanoes within the MRVF display a clear subduction signature with some variation in their trace element geochemistry (Figure 3.5). In continental arc settings, this subduction signature may be linked to several potential sources: (1) metasomatized continental lithospheric mantle; (2) melts or fluid derived from the subducting slab and sediments; (3) subduction-affected asthenospheric wedge; or (4) sub-slab asthenosphere. The variation in MRVF geochemistry and mineralogy suggests different mantle and/or fluid sources for volcano #1, #2, and #3. A sub-slab asthenosphere source (4) can be ruled out because MRVF rocks display LILE enrichments and HFSE depletions that differ from the trace element signatures displayed by typical ocean island basalts (OIBs; Figure 4.4), and an OIB-like signature would be expected from a melt derived from the sub-slab asthenosphere. These OIBs are not as enriched in LILEs as MRVF rocks while also having higher Nb and Ta concentrations (Fig. 4.4). The following discussion investigates: (1) the possible sources for MRVF magmas within a previously established slab tear environment; and (2) and refines the tectono-magmatic model of Brueseke *et al*. (2023) for MRVF volcanism.

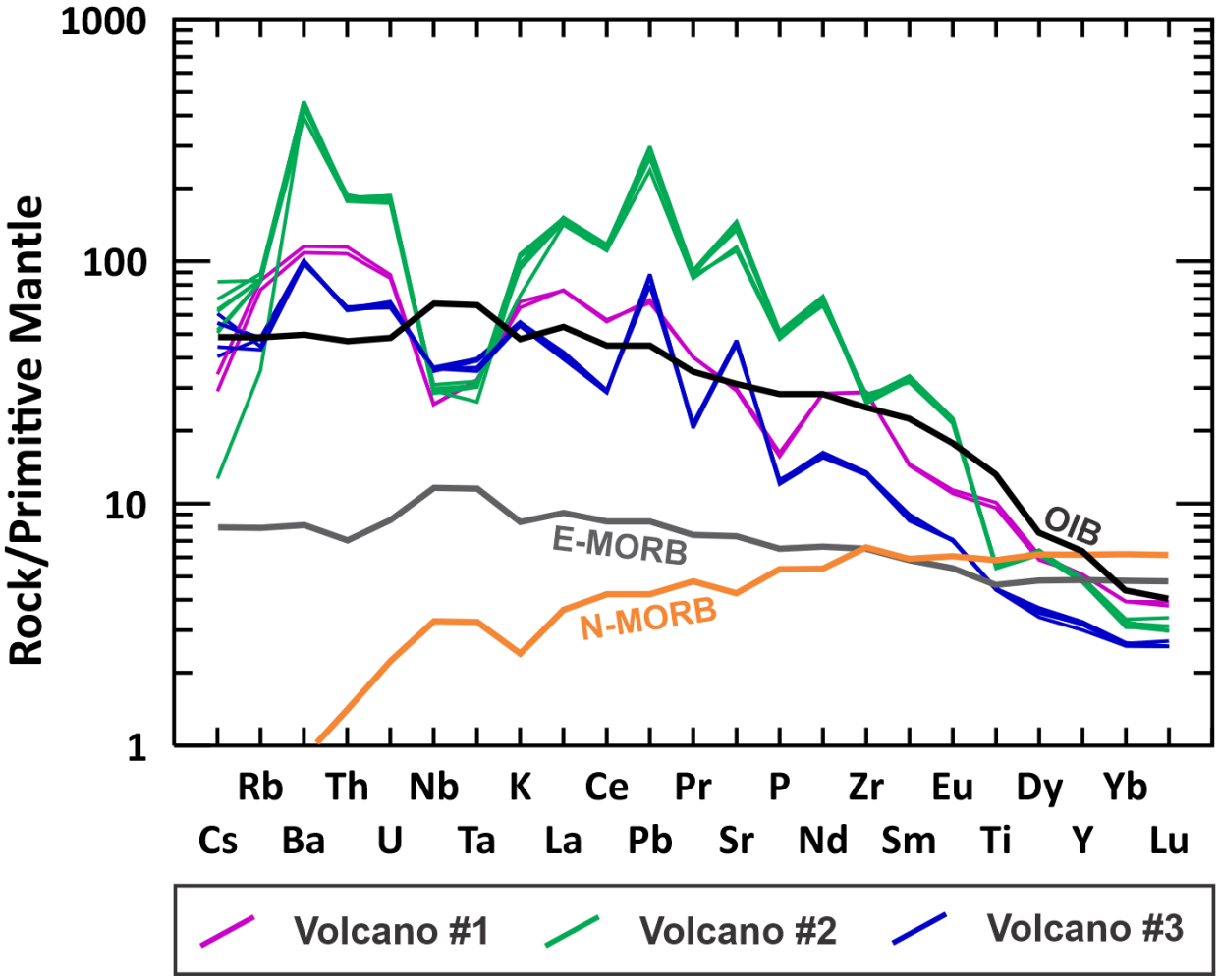

Figure 4.4: A primitive mantle-normalized multielement diagram (normalizing values from Sun and McDonough 1989) displaying rocks from the MRVF plotted with OIB, E-MORB, and N-MORB endmembers. OIB, E-MORB, and N-MORB values from Sun and McDonough (1989).

A Metasomatized Lithospheric Mantle Source for volcano #1

Rocks from volcano #1 are calc-alkaline basaltic andesites and display a typical subduction signature with LILE enrichments and HFSE depletions (Figure 3.4A, Figure 3.5, Figure 3.7). Arc magmas are commonly thought to originate via partial melting of metasomatized mantle wedge (Pearce and Peate, 1995), and the low B/Nb and moderate Th/Nd ratios of volcano #1 indicate no evidence for high fluid-metasomatism in the mantle source (e.g., Zamboni *et al*., 2016) (Figure 4.5). This is supported by the observed fluid dehydration of the Yakutat slab at shallow depths (Chuang *et al*., 2017). In combination with the low Nb/La ratio of volcano #1 (< 0.35; Figure 4.6), it is likely that volcano #1 magmas derive from a mantle wedge or subcontinental lithospheric mantle source, primarily metasomatized by sediment contribution.

Batch melting modeling was employed to test this and determine the potential mantle source and degrees of melting necessary to produce the trace element geochemistry of volcano #1 samples (Figure 4.7, Figure 4.8; Table 4.2). Given that the Yakutat microplate has subducted beneath south-central Alaska for the past 30 million years (Brueseke *et al*., 2019), it's likely that the asthenosphere underneath the MRVF is metasomatized from fluids, sediment- and slab-derived melts and resembles mantle wedge from other locations on Earth affected by flat slab subduction. Because no published geochemical data exist for mantle xenoliths from south-central Alaska (none have been reported thus far), two xenoliths were selected to serve as proxies for a mantle wedge endmember and a metasomatized subcontinental lithospheric mantle endmember.

The mantle wedge endmember is represented by a spinel lherzolite (KBJ-11) from the Klikitarik Bay in the Saint Michael volcanic field in Alaska (Wirth *et al.*, 2002 and references therein). Notably, this xenolith displays evidence of metasomatism, and its geochemistry closely resembles those of fertile upper mantle but with slightly lower wt% MgO, TiO_2, Al_2O_3, and

Na_2O_3 with higher Fe_2O_3 (Wirth *et al.*, 2002). Mineral modes for the spinel lherzolite were estimated and are presented along with its trace element geochemistry in Table 4.2. A hydrated kaersutite pyroxenite type II xenolith (PK-G-22-11) from the Geromino Volcanic Field (GVF) in Arizona, USA, was used as an analogue for a well-characterized, metasomatized subcontinental lithospheric mantle endmember (Kempton *et al*., 2022). Here, flat slab subduction of the Farallon plate between ca. 80 – 55 Ma resulted in slab dewatering and metasomatism of the subcontinental lithospheric mantle beneath the GVF (Kempton *et al*., 2022). The kaersutite pyroxenite xenolith is a product of localized partial melting and crystallization of the subcontinental lithospheric mantle (Kempton *et al*., 2022).

Results from the batch melting model indicate that the magma from volcano #1 did not derive from a hypothetical spinel lherzolite mantle wedge source (Figure 4.6). Rather, the modelling suggests that a 1-10% partial melting of a hypothetical kaersutite pyroxenite (SCLM) source produces the trace element characteristics (relative enrichments and depletions relative to primitive mantle) observed in in volcano #1 rocks (Figure 4.8; Table 4.3).

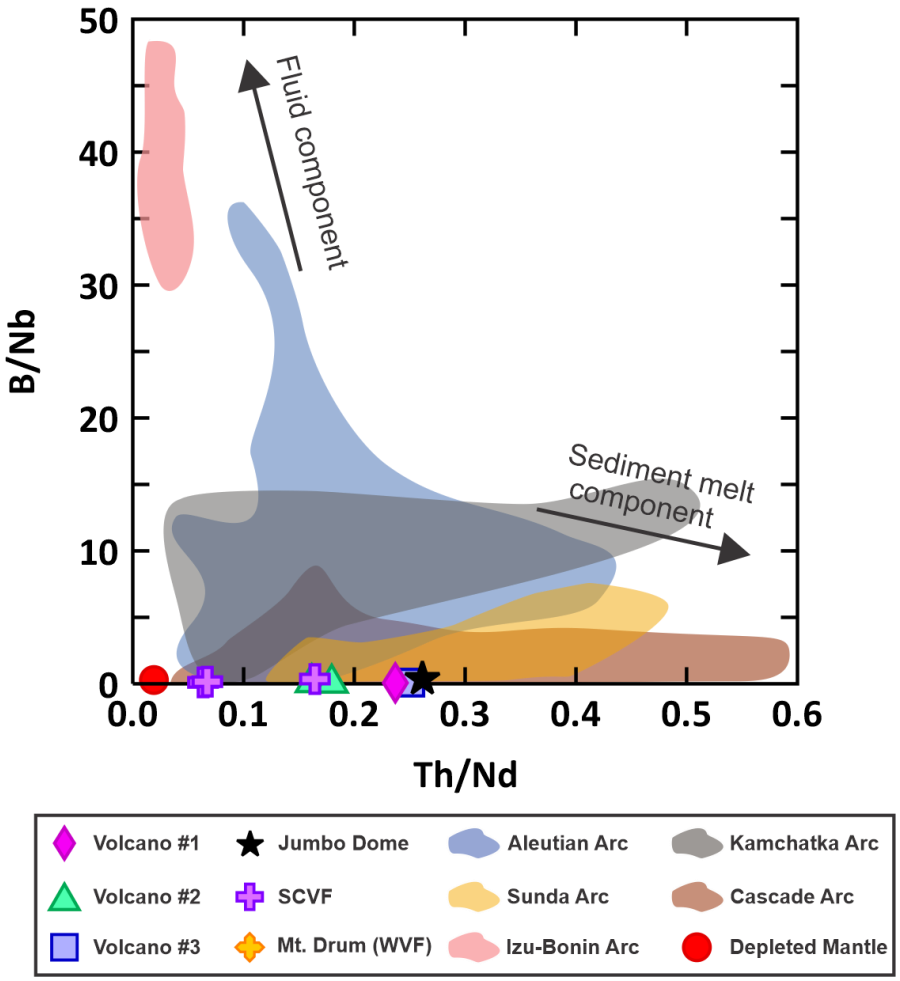

Figure 4.5: Th/Nd vs. B/Nb is used to discriminate between sediment melts and slab-fluid components for volcanic arc/arc segments. Rocks from the MRVF, Jumbo Dome, SCVF, and Mt. Drum show little influence from a slab-fluid component but display varying amounts of subducted sediment-melt influence. Global data for the Aleutians, Kamchatka, Izu-Bonin, Sunda, and Cascades are from the GEOROC geochemical database (https://georoc.mpch-mainz.gwdg.de//georoc/). Trace element data for the depleted mantle from Salters and Stracke (2004). Modified from Zomboni *et al*. (2016).

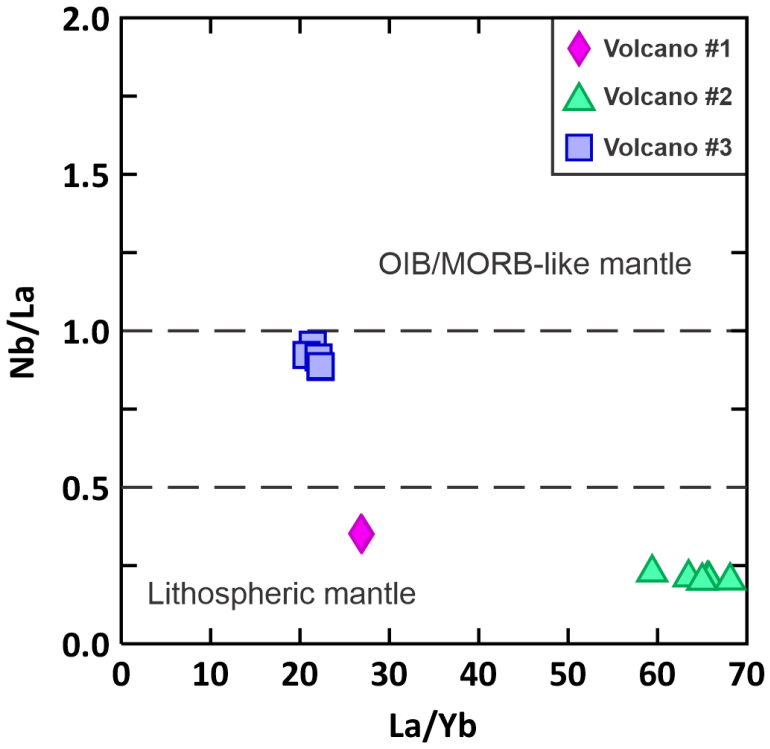

Figure 4.6: La/Yb vs. Nb/La after Smith *et al*., (1999). Low Nb/La for mafic magmas is suggestive of a lithospheric mantle source while high ratios indicate an OIB-like asthenospheric mantle source.

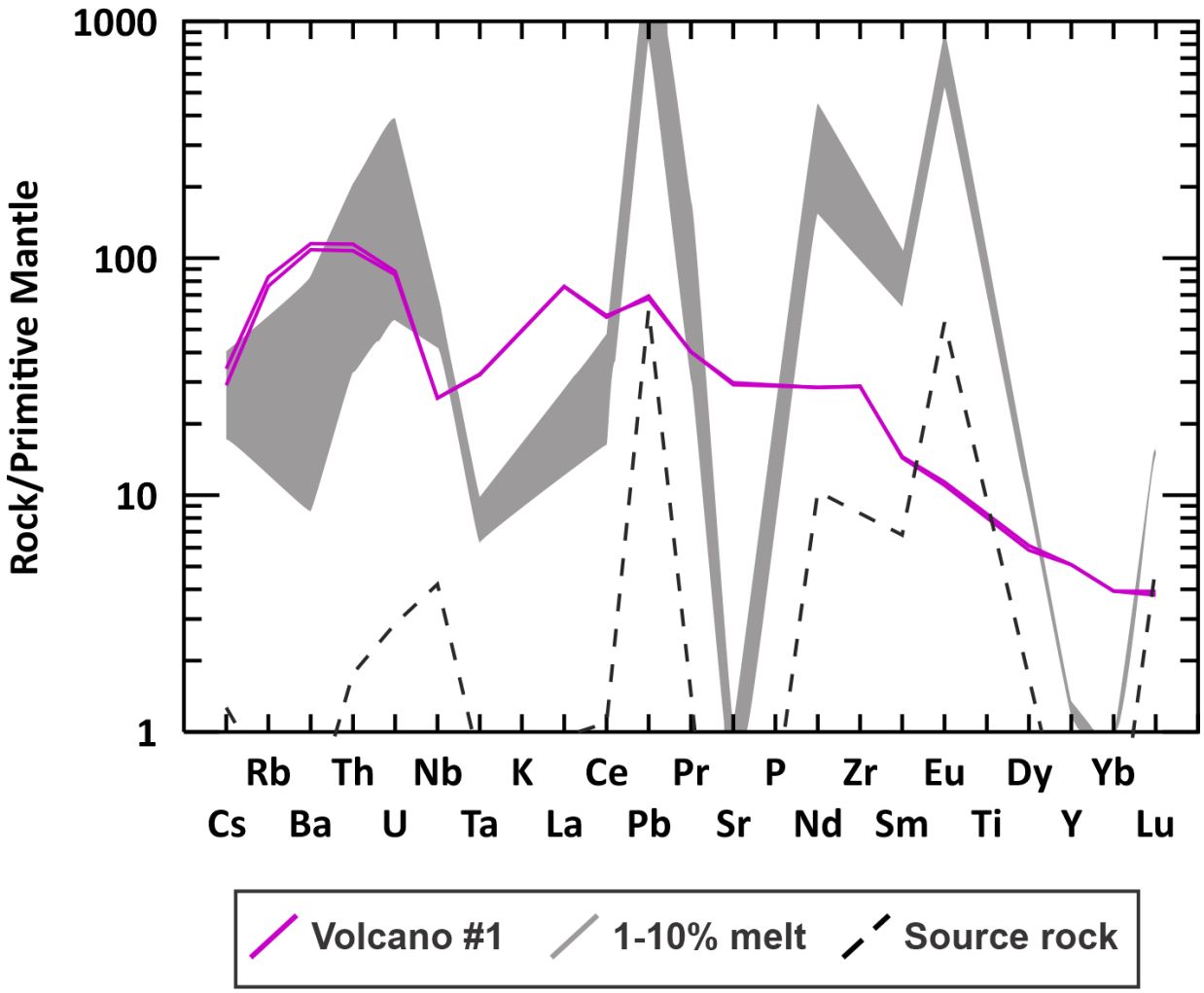

Figure 4.7: A primitive mantle-normalized multielement diagram (normalizing values from Sun and McDonough 1989) displaying rocks from volcano #1 along with the results of simple batch melt modeling of a theoretical mantle wedge endmember using geochemistry from a spinel lherzolite (KB-11J; Wirth *et al.*,2002) and estimated mineral modes. The shaded gray field represents results from 1-10% partial melt of the spinel lherzolite with the following modal mineralogy: 50% olivine, 25% orthopyroxene, 20$ clinopyroxene, 5% spinel.

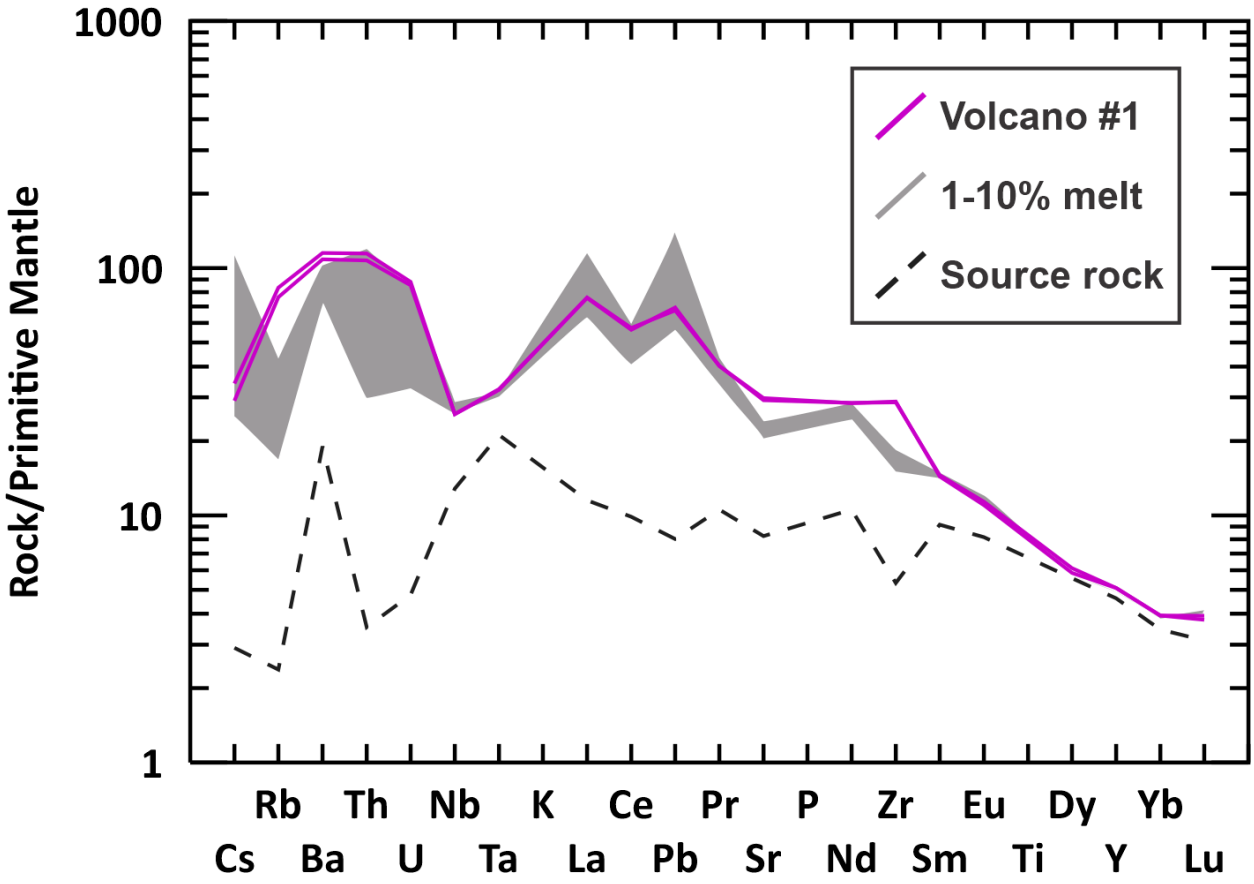

Figure 4.8: A primitive mantle-normalized multielement diagram (normalizing values from Sun and McDonough, 1989) displaying rocks from volcano #1 along with the batch melt model of a hybridized mantle wedge or SCLM endmember using a type 2 mantle xenolith (kaersutite pyroxenite) of the Geronimo Volcanic Field (PK-G-22-12; Kempton *et al.*, 2022). The shaded gray field represents results from 1-10% partial melt of the kaersutite pyroxenite.

	Kd Olv/melt	Ref	Kd Cpx/melt	Ref	Kd Amph/melt	Ref	Kd Oxide / melt	Ref	Kd Spinel/melt	Ref	Kd Rutile/melt	Ref	D	Amph. pyroxenite comp. (ppm)[7]	1% Partial Melt	10% partial Melt
Cs	0.0007	1	0.0058	3	0.03	1	0	Est.	0	Est.	0	Est.	0.016	0.055	0.89	0.20
Rb	0.00018	2	0.011	2	0.09	1	0.001	6	0.001	6	0.0076	9	0.046	5.2	27.3	10.7
Ba	0.000023	1	0.0002	4	0.385	1	0.001	6	0.001	6	0.0137	9	0.177	84	716	512
Th	0.0018	1	0.013	1	0.02	1	0.001	6	0.001	6	0.54	9	0.020	0.57	10.1	2.54
U	0.0013	1	0.006	1	0.01	1	0.01	Est.	0.01	Est.	3.8	10	0.046	0.13	1.75	0.68
Nb	0.004	1	0.0037	1	0.39	1	1	6	1	6	16	11	0.441	13	20	18
Ta	0.03	1	0.0239	1	0.335	1	1	6	1	6	40	10	0.665	3.27	1.28	1.23
La	0.000022	1	0.086	1	0.116	5	0.5	6	0.01	2	0.0031	10	0.091	8.43	78.9	43.5
Ce	0.000045	1	0.175	1	0.185	5	0.6	6	0.01	2	0.087	9	0.158	22.1	105.6	72.5
Pb	0.0013	1	0.009	1	0.095	1	0.0005	6	0.0005	Est.	0.01	Est.	0.047	0.98	10.03	4.0
Pr	0.000085	1	0.289	1	0.277	5	0.0023	6	0.01	2	0.00024	10	0.235	3.44	11.97	9.33
Sr	0.000138	1	0.088	1	0.66	1	0.001	6	0.001	6	0.036	9	0.337	220	506	431
Nd	0.0002	1	0.47	1	0.396	5	0.9	6	0.01	2	0.001	Est.	0.366	20.0	38.4	33.3
Zr	0.008	1	0.1115	1	0.37	1	0.4	6	0.4	6	3.07	9	0.283	77.7	206	168
Sm	0.000636	1	0.81	1	0.651	5	0.9	6	0.01	2	0.002	10	0.609	9.0	6.6	6.3
Eu	0.0012	1	1	1	0.657	5	0.025	8	0.01	2	0.00037	9	0.673	3.0	2.0	1.94
Gd	0.0018	1	1.04	1	0.933	5	0.0055	7	0.01	2	0.0037	9	0.815	4.90	5.58	5.47
Tb	0.00275	1	1.22	1	1	5	0.007	12	0.01	Est.	0.001	Est.	0.913	0.78	0.78	0.78
Dy	0.004	1	1.4	1	0.967	5	0.0071	6	0.01	2	0.00076	9	0.964	4.58	4.25	4.24
Y	0.00719	1	0.67	1	1.325	1	0.4	6	0.4	6	0.459	9	0.941	23	22	22
Ho	0.00643	1	1.35	1	1.03	5	0.0079	7	0.01	2	0.001	Est.	0.975	0.91	0.81	0.81
Er	0.011	1	1.34	1	0.851	5	0.0073	6	0.01	2	0.001	Est.	0.889	2.32	2.32	2.3
Tm	0.0014	1	1.38	1	0.816	5	0.0075	6	0.01	2	0.001	Est.	0.887	0.32	0.31	0.31
Yb	0.0188	1	1.42	1	0.787	5	0.018	8	0.01	2	0.0093	9	0.890	1.88	1.91	1.89
Lu	0.028	1	1.16	1	0.698	5	0.023	7	0.01	2	0.0124	9	0.753	0.27	0.30	0.30

Mineral Modes (%)	**Olivine**	**Cpx**	**Kaersutite**	**Oxide**	**Spinel**	**Rutile**
	6	37	46	1	9	1

Table 4.3: Partition coefficients, bulk partition coefficients, the initial kaersutite pyroxenite composition, results from 1-10% partial melting calculations, and mineral modes for batch melt modeling of volcano #1 seen in Figure 4.8. Partition coefficients given above are based on the following references: [1]Rollinson and Pease (2021); [2]McKensie and O'Nions (1991); [3]Hauri *et al*. (1994); [4]Hart and Dunn (1993); [5]Botazzi *et al*. (1999); [6]Rollinson (1993); [7]Nielsen *et al*. (1992); [8]Lemarchand *et al*. (1987); [9]Foley *et al*. (2000); [10]Klemme *et al*. (2005); [11]McCallum and Charette (1978); [12]Zack and Brumm (1998); kaersutite pyroxenite trace element composition modified from Kempton *et al*. (2022). Mineral modes from Kempton (pers. comm). Est = estimation Olv = olivine; cpx = clinopyroxene, amph = amphibole, Kd = partition coefficient, D = bulk partition coefficient.

.

An Enriched Subcontinental Lithospheric Mantle Source for Volcano #2

Samples from volcano #2 are alkaline, basalts and trachybasalts, are shoshonite-like, and they are most enriched in LILEs, Ni, Ba, Sr, and Cr, while also being the most primitive (e.g., Mg# 67-72; SiO_2 < 50 wt%) in comparison to the other MRVF volcanoes (Figure 3.3, Figure 3.4, Figure 3.7, Table 3.1). Volcano #2 is also distinctive relative to other MRVF volcanoes because these rocks display the most hydrated mineralogy with phlogopite and amphibole phenocrysts and groundmass crystals (Appendix B). Isotopically, these rocks display the most radiogenic Sr-Nd-Pb isotopic signatures in the MRVF which may rule out a convecting upper mantle source (Figures 3.8 – 3.12). Similar to volcano #1, the low B/Nb and moderate Th/Nd ratios of volcano #2 indicate no evidence for high degrees of fluid-metasomatism in the mantle source for these magmas (Figure 4.5). Moreover, the primitive geochemical signature of volcano #2 rocks (e.g., low SiO_2, high MgO, high Ni and Cr), low Nb/La ratios (<0.2; Figure 4.6), shoshonite-like affinity, LILE enrichments and HFSE depletions, and Sr-Nd isotopic signature indicate that their magmatic source is consistent with a an metasomatized mantle wedge or subcontinental lithospheric mantle source.

Batch melting modeling was employed to determine plausibility of a subcontinental lithospheric mantle or mantle wedge source and the degrees of melting necessary to produce the trace element geochemistry of volcano #2 rock samples (Figure 4.9, Figure 4.10). In this model, a type II xenolith from the Geromino Volcanic Field (pk-G-22-1; Kempton *et al.*, 2022) was selected and its modal mineralogy and geochemistry were slightly modified to represent an enriched subcontinental lithospheric mantle source while maintaining its classification as a kaersutite pyroxenite. The original and modified modal mineralogy and trace element data is found in Table 4.4. As mentioned earlier, type II xenoliths from the Geromino Volcanic field are

interpreted to represent the crystallization products of basaltic melts within the lithospheric mantle (Kempton *et al*., 2022 and references therein). Moreover, they are the physical representations of what could be the main type of metasomatic fluid in the mantle (Kempton *et al*., 2022 and references therein), i.e., water-rich silicate melts. Additionally, the same spinel lherzolite from the Saint Michael volcanic field was used to represent a mantle wedge source (Table 4.2). Results from the batch melting model indicate that the magma from volcano #1 did not derive from a hypothetical spinel lherzolite mantle wedge source (Figure 4.9). Rather, the modeling points to a subcontinental lithospheric mantle source given that a 1-5% partial melting of a hypothetical kaerustite pyroxenite source produces the trace element subduction affinity observed in volcano #2 rocks (Figure 4.10).

Volcano #2 rocks display a shoshonite-like K_2O affinity (Figure 3.4) and the origin of shoshonitic magmatism is commonly related to thermal events in the mantle, such as slab tear formation or slab break offs (Aldanmaz *et al*., 2000; Gasparon *et al*., 2009; Pe-Piper *et al*., 2009; Zhang *et al*., 2020). Given that the MRVF is located above the surficial projection of the imaged Yakutat slab tear (Mann *et al.*, 2022) and is interpreted to record the initiation of Yakutat slab tear formation (Brueseke *et al*., 2023), then this Yakutat tear initiation and subsequent asthenospheric upwelling likely provided the heat necessary to melt the subcontinental lithospheric mantle beneath the MRVF and generate volcano #2 magmas.

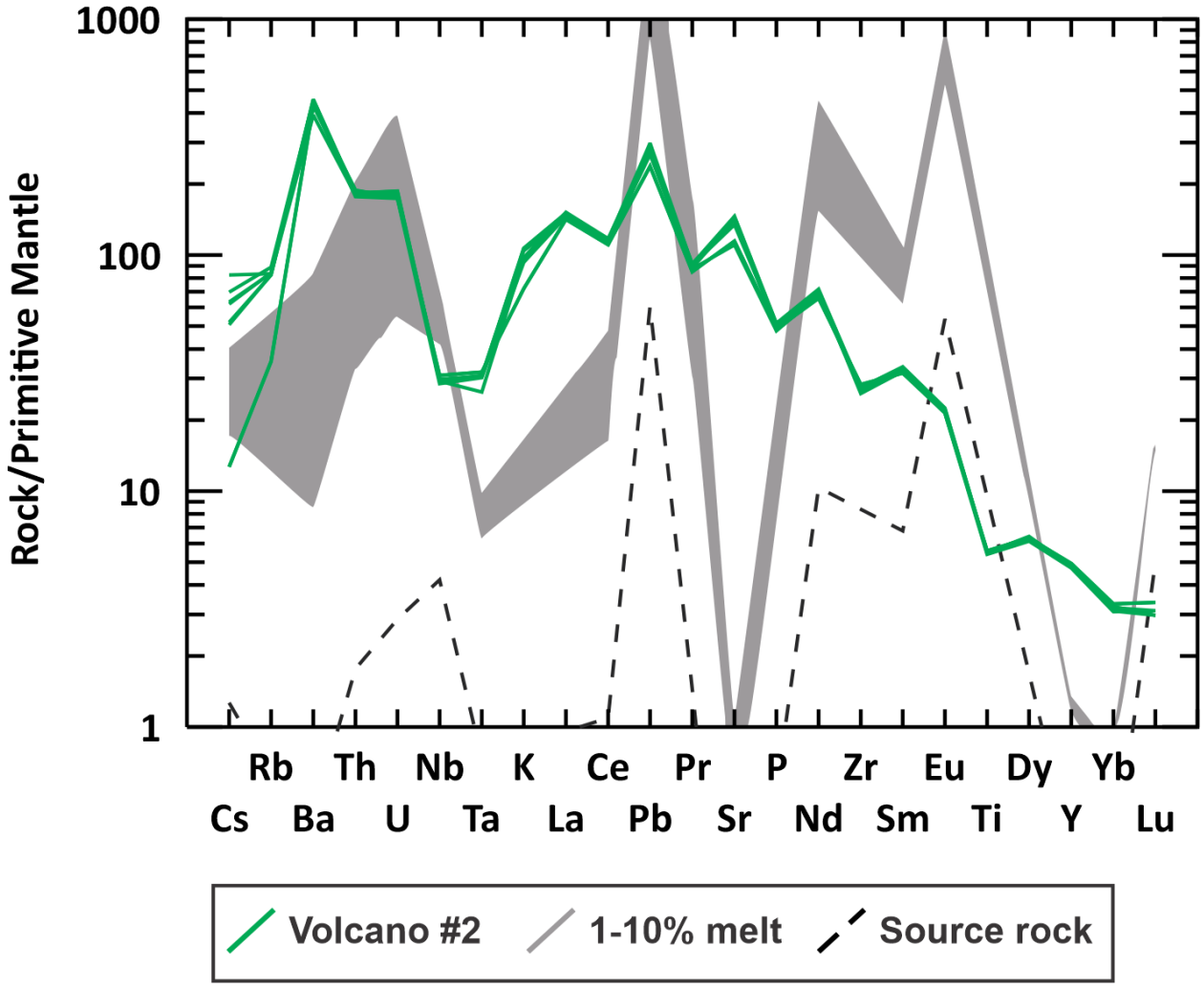

Figure 4.9: A primitive mantle-normalized multielement diagram (normalizing values from Sun and McDonough 1989) displaying rocks from volcano #2 along with the results of simple batch melt modeling of a theoretical mantle wedge endmember using geochemistry from a spinel lherzolite (KB-11J; Wirth *et al.*, 2002) and estimated mineral modes. The shaded gray field represents results from 1-10% partial melt of the spinel lherzolite with the following modal mineralogy: 50% olivine, 25% orthoproxene, 20$ clinopyroxene, 5% spinel.

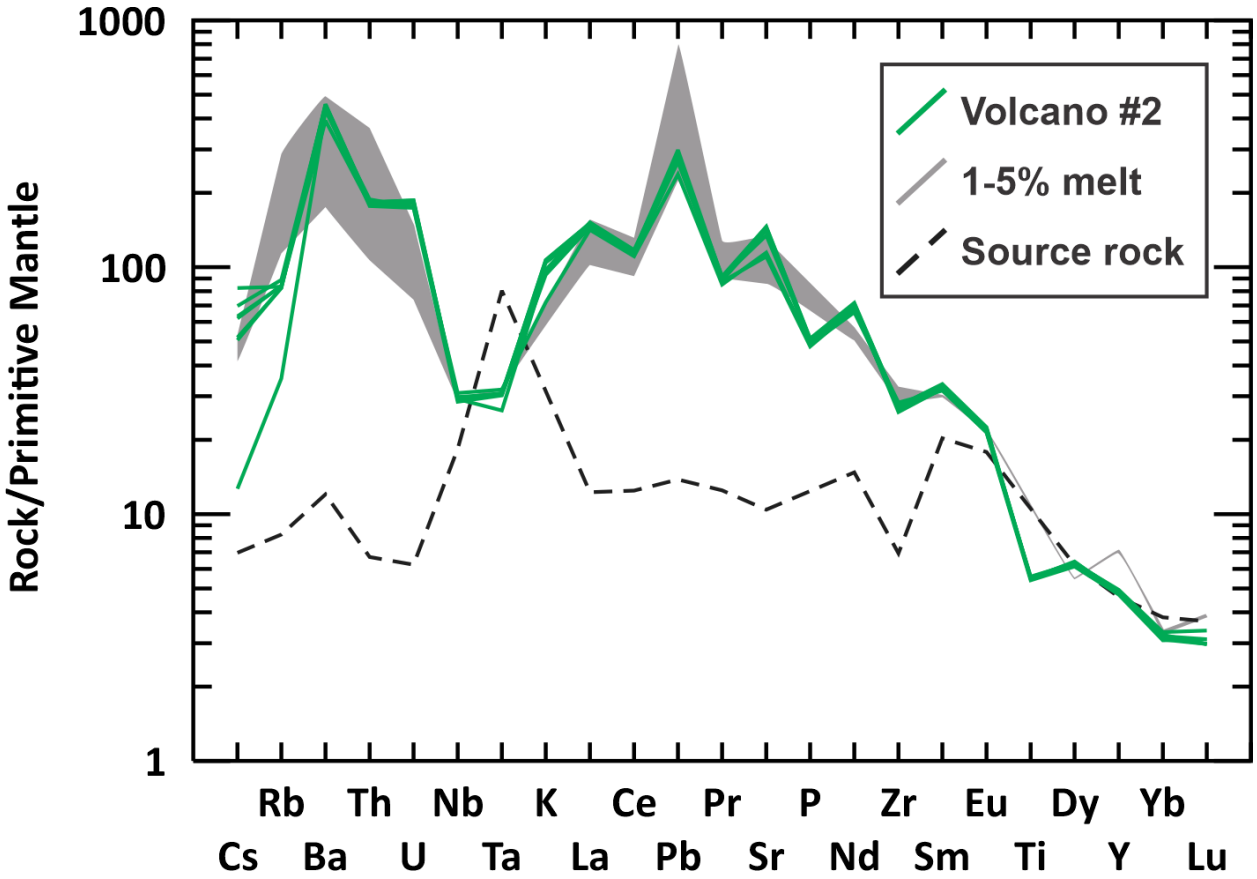

Figure 4.10: A primitive mantle-normalized multielement diagram (normalizing values from Sun and McDonough 1989) displaying rocks from volcano #2 along with the results of simple batch melt modeling of a theoretical subcontinental lithospheric mantle endmember using modified mineral modes and geochemistry from a type 2 mantle xenolith (kaersutite pyroxenite) of the Geronimo Volcanic Field (PK-G-22-1; Kempton *et al.*, 2022). The shaded gray field represents results from 1-5% partial melt of the kaersutite pyroxenite with the following modal mineralogy: 78% clinopyroxene, 10% spinel, 5% kaersutite, 5% olivine, 2% rutile.

	Kd Olv / Melt	Ref	Kd Cpx / Melt	Ref	Kd Kaersutite / Melt	Ref	Kd Spinel / Melt	Ref	Kd Rutile/ Melt	Ref	D	Kaersutite pyroxenite comp. (ppm)[12]	1% partial melt	5% partial melt
Cs	0.0007	1	0.13	3	0.5	3	0	Est.	0.001	Est.	0.1265	0.055	0.42	0.32
Rb	0.00018	2	0.011	2	0.3	6	0.001	8	0.0076	10	0.0238	5.2	182	72
Ba	0.000023	1	0.0002	4	0.385	1	0.001	8	0.0137	10	0.0195	84	3440	1225
Th	0.0018	1	0.013	1	0.02	1	0.001	8	0.1	9	0.0133	0.57	31.15	9.08
U	0.0013	1	0.006	1	0.01	1	0.01	Est.	1.5	9	0.0362	0.13	3.19	1.55
Nb	0.004	1	0.0037	1	0.39	1	1	8	25	9	0.6226	13	20	20
Ta	0.03	1	0.0239	1	0.335	1	1	Est.	120	9	2.5369	3.27	1.29	1.33
La	0.000022	1	0.086	1	0.116	7	0.01	2	0.0031	9	0.0259	8.43	107.3	71.1
Ce	0.000045	1	0.1	2	0.185	7	0.01	2	0.087	10	0.0739	22.1	233.9	163.2
Pb	0.0013	1	0.009	1	0.095	1	0.0005	11	0.01	Est.	0.0900	0.98	57.5	15.9
Pr	0.000085	1	0.1	5	0.277	7	0.01	2	0.00024	9	0.0121	3.44	35.3	24.9
Sr	0.000138	1	0.088	1	0.12	2	0.001	8	0.036	10	0.0929	220	2747	1808
Nd	0.0002	1	0.3	5	0.396	7	0.01	2	0.001	Est.	0.0755	20.0	77.3	68.5
Zr	0.008	1	0.1115	1	0.37	1	0.4	8	3.07	10	0.0440	78	368	314
Sm	0.000636	1	0.81	1	0.651	7	0.01	2	0.002	9	0.2548	9.0	13.5	13.2
Eu	0.0012	1	1	1	0.657	7	0.01	2	0.00037	10	0.2073	3.0	3.68	3.64
Gd	0.0018	1	1.04	1	0.933	7	0.01	2	0.0037	10	0.6654	4.90	5.70	5.66
Tb	0.00275	1	1.22	1	1	7	0.01	2	0.001	Est.	0.8139	0.78	0.78	0.78
Dy	0.004	1	1.4	1	0.967	7	0.01	2	0.00076	10	0.5349	4.58	4.01	4.04
Y	0.00719	1	0.67	1	1.325	7	0.4	8	0.459	9	0.8590	23	33	32
Ho	0.00643	1	1.35	1	1.03	7	0.01	2	0.001	Est.	1.0028	0.91	.82	.83
Er	0.011	1	1.34	1	0.851	7	0.01	2	0.001	Est.	1.1416	2.32	2.13	2.14
Tm	0.0014	1	1.38	1	0.816	7	0.01	2	0.001	Est.	0.7152	0.32	0.29	0.29
Yb	0.0188	1	1.42	1	0.787	7	0.01	2	0.0093	10	1.1058	1.88	1.63	1.65
Lu	0.028	1	1.16	1	0.698	7	0.01	2	0.0124	10	1.0893	0.27	0.29	0.29

Mineral Modes (%)	Olivine	Clinopyroxene	Kaersutite	Spinel	Rutile
Original Modes	6	80	10	3	0
Modified Modes	5	78	5	10	2

Table 4.4: Partition coefficients, bulk partition coefficients, the initial kaersutite pyroxenite composition, mineral modes, and results from batch melt modeling of volcano #2 seen in Figure 4.10. Partition coefficients given above are based on the following references: [1]Rollinson and Pease (2021) – Table 4.1; [2]McKensie and O'Nions (1991); [3]Villemant *et al*. (1981); [4]Hart and Dunn (1993); [5]Skulski *et al*. (1994); [6]Matsui *et al*. (1977); [7]Botazzi *et al*. (1999); [8]Rollinson (1993); [9]Klemme *et al*. (2005); [10]Foley *et al*. (2000); [11]Elkins *et al*. (2008). Kaersutite pyroxenite starting trace element composition modified from Kempton *et al*. (2022). Mineral modes adjusted from Kempton (pers. Comm.). Est = estimated, olv = olivine, cpx = clinopyroxene, Kd = partition coefficient, D = bulk partition coefficient.

The Adakite Signature of Volcano #3 From Slab Melting

The term “adakite” was originally coined by Defant and Drummond (1990) to describe the unusual geochemical affinity of the Cenozoic arc rocks associated with the subduction of young (≤) 25 Ma oceanic lithosphere at Adak Island. Adakites are geochemically characterized by $SiO_2 \geq 56$ wt%, $Al_2O_3 > 15$ wt%, MgO < 6 wt%, Y ≤ 18 ppm, Yb ≤ 1.9 ppm, Sr > 400 ppm, Sr/Y > 40, and La/Yb > 20 (Zhang *et al*., 2021). This geochemical signature was initially considered to be the product of partial-melting of MORB-like oceanic crust metamorphosed to eclogite or garnet amphibolite facies, where the presence of garnet in the source rock retains Y and Yb, resulting in the high Sr/Y, La/Yb, and low Y and Yb values observed in adakites (Defant and Drummond, 1990; Rapp *et al*., 1991). Originally, only young, hot oceanic crust was thought to melt under normal subduction conditions (Castillo, 2012); however, anomalous subduction conditions may allow old or cold oceanic lithosphere to melt. These include subduction initiation or termination (Sajona *et al*., 1993; Sajona *et al*., 1996), during highly oblique subduction (Yogodzinski *et al*., 1995), shallow subduction (Gutscher *et al*., 2000), melting due to elevated shear stress (Yogodzinski *et al*., 1995), and melting of the slab edge around a slab window or slab tear (Thorkelson and Breitsprecher, 2005; Yogodzinski *et al*., 2001).

Moreover, the adakite signature may be replicatesd by other petrogenetic processes that do not require slab melting. Thus, the term ‘adakitic’ or ‘adakite-like’ is used to distinguish rocks with geochemical similarities to adakites, with adakites being formed strictly by slab-melting (Castillo, 2012; Zhang *et al*. 2021). Adakitic or adakite-like rocks may be formed by partial melting of lower crust, in the garnet-amphibolite to eclogite facies, that has been underplated by basaltic magma (e.g., Atherton and Petford, 1993); or produced through fractional crystallization of garnet-bearing assemblages of a parental arc basaltic magma (Macpherson *et al*., 2006).

Adakites and adakitic rocks have been divided into the following classifications according to Zhang *et al*., (2021): (1) high-SiO_2 adakites; (2) low-SiO_2 adakites; and (3) high-Mg# adakitic rocks. Each classification has different interpreted petrogenetic models. High-SiO_2 adakites (HSA) contain a SiO_2 content higher than 60 wt% while low-SiO_2 adakites (LSA) contain a SiO_2 content lower than 60 wt%. HSA are considered to be partial melts of subducted oceanic crust that interacted with mantle wedge peridotites during their ascent. In contrast, LSA represent mantle melts of peridotite that reacted with silicic melts of subducted oceanic crust and typically have high MgO concentrations. Zhang *et al*., (2021) found that HSA falls within the initial definition of adakites, whereas LSA can be termed adakitic rocks. High-Mg# adakitic rocks are defined as having either Mg# > 45 (e.g., Wang *et al*., 2016; Jia *et al*., 2017) or Mg# > 50 (Duan *et al*., 2015; Wang *et al*., 2017) and are indicative of a mantle peridotite signature (Castillo, 2012). These high-Mg# adakitic rocks are derived from the interaction between mantle peridotite and lower crustal materials delaminated into the mantle, or forearc crust carried down by subduction erosion (Castillo, 2012 and references therein).

Based on the geochemical criteria above, rocks from volcano #3 display a high-Mg#, low SiO_2 adakitic signature (SiO_2 > 56.5-57 wt%, Al_2O_3 = ~16.6 wt%, MgO = 6.34 - 6.39 wt%, Y = 13.6 - 14.7 ppm, Yb = 1.27 - 1.31 ppm, Sr = 957 - 993 ppm, Sr/Y = 65 - 73, and La/Yb = 20.7 - 22.1; Table 3.1 Figure 4.11). These rocks may also be defined as primitive andesites due to their high Mg# (> 60; Kelemen *et al*., 2014). Kelemen et al. (2014) proposed several petrogenetic models for these kinds of magmas, including: (1) partial melting of subducted basalt or sediment in eclogite facies, which subsequently reacted with the overlying mantle peridotite to form a hybrid melt; (2) fluid-fluxed partial melting of an enriched mantle source; and (3) mixing of primary basalt and granitic lower crustal melts.

Trace elements have been used to distinguish between melting of the subducting slab or lower crust, such as during delamination. A plot of Cr ppm vs. wt% SiO_2 indicates that samples from volcano #3 plot along the array of oceanic crust-derived adakites, when projected to higher Cr and low wt% SiO_2 (Figure 4.12). This also suggests a delamination origin for the adakite signature of volcano #3 is unlikely, which is consistent with the volcano's location over an imaged slab tear. Next, a partial melting of a fluid-fluxed mantle wedge scenario is considered. Hydrous melts have a high capacity to transport water-soluble and water-insoluble elements, whereas fluids only have a high capacity to transport water-soluble elements (Zheng 2012; Wang *et al*. 2014). Thus, incompatible trace element ratios can discriminate between slab fluid components and sediment melt components in arc magmas. For example, B/Nb is a tracer of slab fluid released during the dehydration of sediment and altered oceanic crust (Ishikawa and Tera, 1997; Zamboni *et al*., 2016), while Th/Nd is a tracer of sediment melt in arc magmas (Class *et al.*, 2000; Zamboni *et al*., 2016). Figure 4.5 shows that the mantle source of volcano #3 was not metasomatized by slab-fluids and therefore flux-melting of mantle wedge seems unlikely to have formed the magmas that erupted at volcano #3. This is further supported by the elevated Nb/La ratios (0.84-1.11; Figure 4.6) which extend toward the OIB-like asthenosphere field.

Rather, it is likely that the adakitic signature of volcano #3 reflects partial melting of subducted eclogitized oceanic crust, which subsequently reacted with overlying mantle peridotite to form a hybrid melt (Kelemen *et al*., 2014; Zhang *et al*., 2021). Although the Yakutat oceanic plateau is 50-55 Ma (Wells *et al.*, 2014) and hence old/cold, anomalous subduction conditions beneath south-central Alaska provide the right conditions to induce slab melting. For example, the Yakutat slab is subducting obliquely, which may increase the temperature of the shallowly subducting slab (Daly *et al*., 2021). At the same time, toroidal asthenospheric upwelling along

the slab edge and through the Yakutat slab tear could provide the heat source to generate a slab melt (Király *et al*., 2020).

To test this slab-melt hypothesis, batch melting models were used to simulate partial melting of a subducted eclogitized oceanic crust (Figure 4.13; Table 4.4). Due to the lack of published geochemical data from Yakutat plateau basalts, the average trace element chemistry of Siletzia basalts and basaltic andesites (< 55% wt% SiO_2) from the Siletzia oceanic plateau was used as an analogue (Ciborowski *et al*., 2020). Siletzia is considered a rifted segment of a larger plateau that formed when the Yakutat plateau rifted away, prior to it being transported northward to its current location in Alaska (Wells *et al*., 2014). Eclogite modal mineralogy was modified from an eclogite sample (36-NC-62) described in Coleman *et al*. (1965). The melt model indicates that 15% - 30% partial melting of a subducted eclogitic slab yields the trace element geochemistry observed in samples of volcano #3. Given that the limited assimilation of peridotite can raise the Mg# of slab-derived melts while having little effect on Sr/Y, La/Yb or other key element ratios (Rapp *et al*., 1999), mantle-hybridized slab melts should possess mantle-normalized, trace element abundance patterns similar to those of pristine slab melts, with the primary differences between the two being reflected in major element geochemistry (e.g., Mg# and SiO_2 content). Therefore, it is likely that a 15-30% partial melt of an eclogitic slab, consistent with the experimental slab melts of Rapp *et al*. 1999, could have interacted with overlying mantle peridotite to produce the trace element abundances and adakitic signature observed in volcano #3.

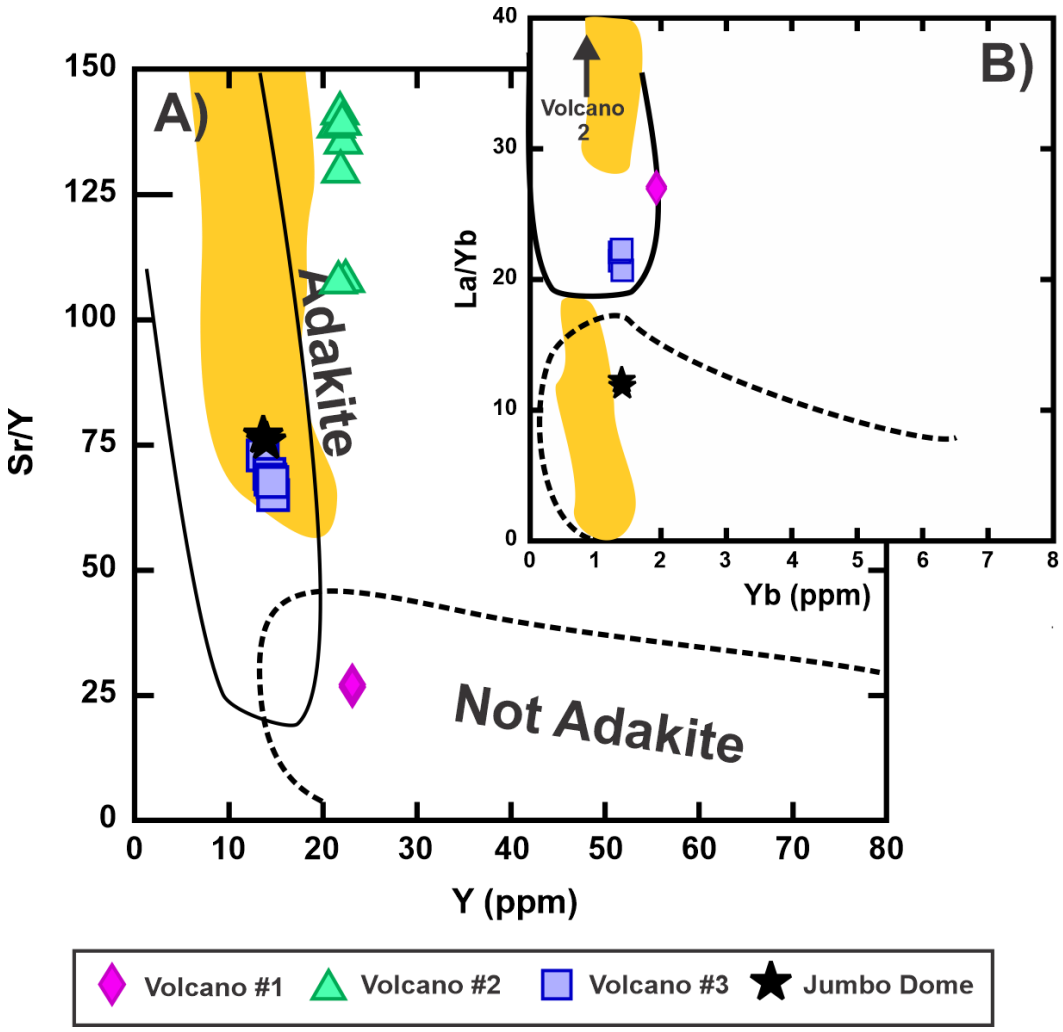

Figure 4.11: Adakite discrimination diagrams. (A) Sr/Y vs. Y plot showing fields for adakites and island arc andesite-rhyolite-dacites (labelled 'not Adakite') with MRVF and Jumbo Dome samples compared to slab melt-derived adakites from central America denoted in the orange fields (Gazel *et al*., 2011). (B) La/Yb vs. Yb with the same fields; volcano #2 samples plot off the diagram with La/Yb = 60-68. Modified from Brueseke *et al*. (2023).

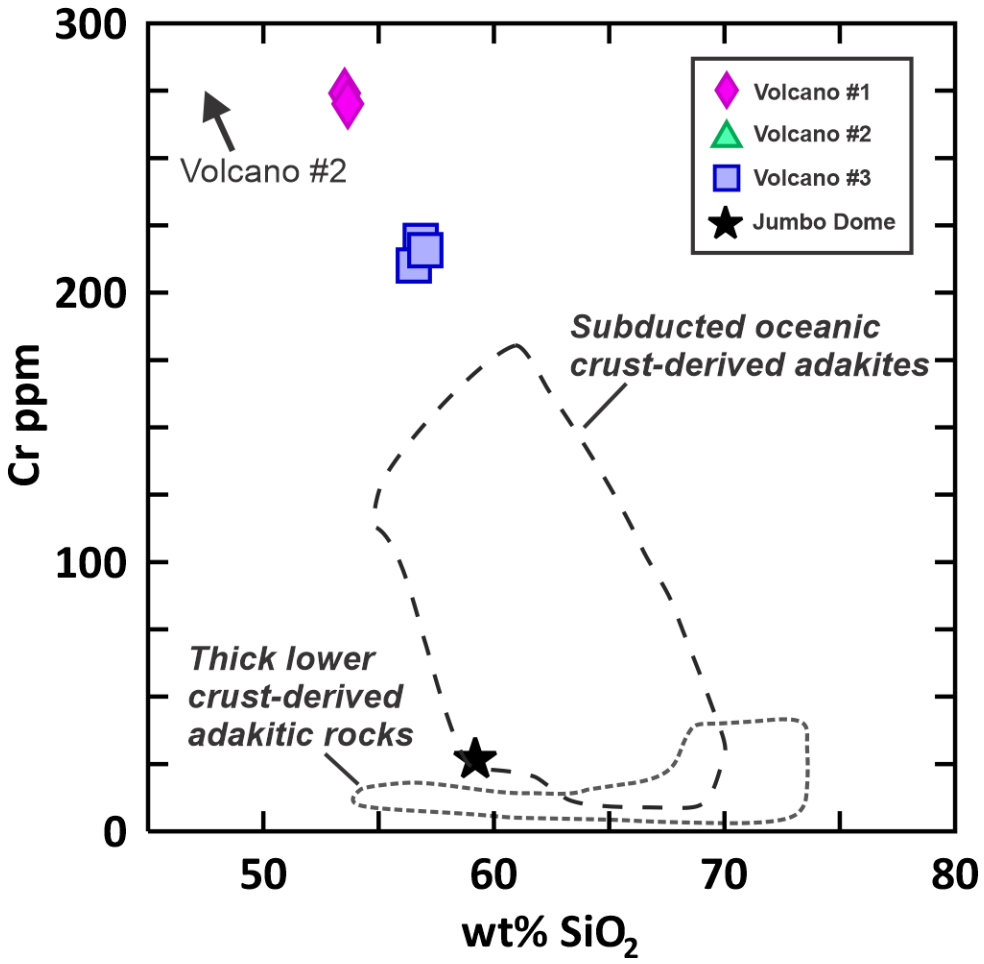

Figure 4.12: Cr vs. wt% SiO_2 variations for MRVF and Jumbo Dome rocks. Fields for subducted oceanic crust-derived adakites and thick lower crust-derived adakitic rocks are from Wang *et al*. (2006) and references therein. Modified after Berkelhammer *et al*. (2019).

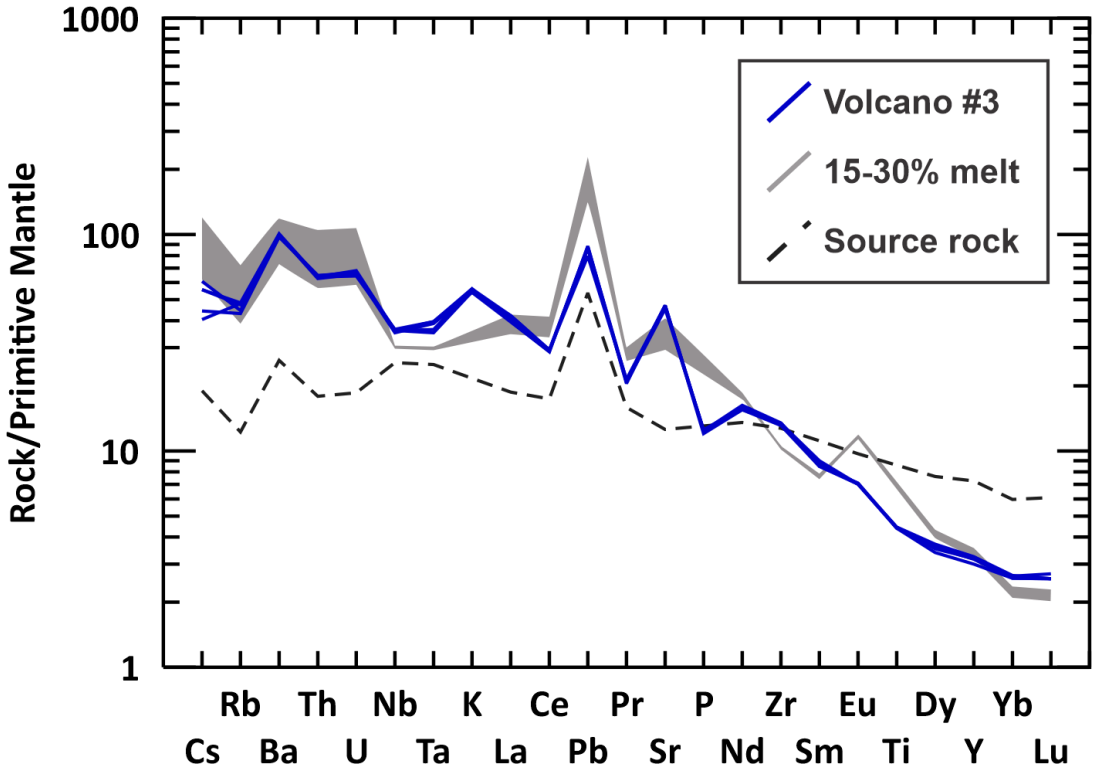

Figure 4.13: A primitive mantle-normalized multielement diagram (Sun and McDonough 1989) displaying rocks from volcano #3 along with batch melt model results of eclogite with a geochemistry similar to Siletzia terrane (Ciborowski *et al*., 2020) and modal mineralogy modified from an eclogite sample (36-NC-62) described in Coleman *et al*. (1965). The shaded gray field represents results from 15-30% partial melt of the eclogite with the following modal mineralogy: 55% clinopyroxene, 20% garnet, 19% amphibole, 4% titanite, and 2% rutile.

	Kd Cpx / Liq	Ref	Kd Garnet / Liq	Ref	Kd Amph / Liq	Ref	Kd Titanite / Liq	Ref	Kd Rutile/ liq	Ref	D	Eclogite Comp. (ppm)[7]	15% Partial Melt	30% Partial Melt
Cs	0.0058	3	0.005	Est.	0.03	2	0.002	5	0	1	0.010	0.15	0.95	0.49
Rb	0.011	4	0.0007	2	0.09	2	0.0003	5	0	1	0.023	7.8	45.8	24.6
Ba	0.02	1	0.00037	2	0.385	2	0.0023	5	0	1	0.084	183	827	510
Th	0.03	1	0.0015	2	0.02	2	0.1	5	0	1	0.025	1.5	8.9	4.8
U	0.04	1	0.01	2	0.01	2	0.1	5	0	1	0.030	0.39	2.25	1.23
Nb	0.02	1	0.005	2	0.39	2	3	5	30	1	0.806	18.2	21.8	21.1
Ta	0.0239	1	0.005	Est.	0.335	2	3	5	30	1	0.798	1.02	1.23	1.19
La	0.04	1	0.0047	2	0.2	2	7	6	0	1	0.341	12.9	29.2	23.9
Ce	0.08	1	0.0179	2	0.35	2	5	5	0	1	0.314	30.9	74.0	59.4
Pb	0.1	1	0.00034	2	0.095	2	0.7	5	0	1	0.101	3.82	16.2	10.3
Pr	0.14	1	0.0593	2	0.61	2	6	5	0	1	0.445	4.38	8.29	7.16
Sr	0.07	1	0.0074	2	0.66	2	0.5	5	0	1	0.185	265	861	616
Nd	0.2	1	0.17	2	0.73	2	10	5	0	1	0.683	18.3	25.1	25.6
Zr	0.3	1	0.73	2	0.37	2	3	5	40	1	1.301	143	113	118
Sm	0.4	1	0.87	2	1.075	2	25	6	0	1	1.598	4.95	3.28	4.49
Eu	0.45	1	1.63	2	1.13	2	0.21	6	0	1	0.797	1.63	1.98	1.91
Gd	0.6	1	2.55	2	1.37	2	10	5	0	1	1.500	5.44	3.82	4.03
Tb	0.65	1	4.2	2	1.39	2	5	5	0	1	1.662	0.89	0.57	0.61
Dy	0.7	1	6.2	2	1.405	2	5	5	0	1	2.092	5.62	2.91	3.18
Y	0.67	2	8.5	2	1.325	2	4.39	5	0	1	2.496	33	14	16
Ho	0.7	1	8.2	2	1.36	2	26	6	0	1	3.323	1.08	0.36	0.41
Er	0.7	1	9.6	2	1.275	2	5	5	0	1	2.747	3.05	1.23	1.37
Tm	1.38	2	11.1	2	1.2	2	2	5	0	1	3.287	0.47	0.16	.18
Yb	0.7	1	12.6	2	1.05	2	2	5	0	1	3.185	2.94	1.03	1.16
Lu	0.7	1	13.7	2	0.85	2	2	5	0	1	3.367	0.45	0.15	0.17

Mineral Modes (%)	**Cpx**	**Garnet**	**Amph**	**Quartz**	**Titanite**	**Rutile**	**Epidote**	**Muscovite**	**Chlorite**
Source Rock	34.4	28.9	19.9	8.2	4	2	3.9	0.7	0.5
Modified Values	55	20	19	0	4	2			

Table 4.4: Partition coefficients, bulk partition coefficients, the initial eclogite composition, mineral modes, and results from the 15-30% batch melt modeling of volcano #3 seen in Figure 4.7. Partition coefficients given above are based on the following references: [1]Kelemen *et al*. (2003); [2]Rollinson nad Pease (2021); [3]Hauri *et al*. (1994); [4]McKensie and O'Nions (1991); [5]Prowatke and Klemme (2005); [6]Adjusted from Green and Pearson (1983). The average trace element geochemistry of Siletzia basalts – basaltic andesites (< 55% wt% SiO_2) from [7]Ciborowski *et al*. (2020) were used for the eclogite endmember. Eclogite mineral modes were adjusted from sample 36-NC-62 from Coleman *et al*. (1965). Est = estimated, cpx = clinopyroxene, amph = amphibole, Kd = partition coefficient, D = bulk partition coefficient.

The Negative $\delta^{26}Mg$ Composition of MRVF rocks

The MRVF rock samples have $\delta^{26}Mg$ compositions between -0.29 and -0.20 (± 0.064) and fall within the range of Mg isotope compositions exhibited by mid-ocean ridge basalts (MORBs, $\delta^{26}Mg$ = -0.31 to -0.19‰), ocean island basalts (OIB, $\delta^{26}Mg$ = -0.35 to -0.18‰), the primitive mantle ($\delta^{26}Mg$ = -0.25 ± 0.04‰) (Teng, 2010; Teng *et al*., 2017), and the most negative abyssal peridotite/serpentinite values ($\delta^{26}Mg$ = -0.24 to 0.03; Liu *et al*., 2017). No trends between $\delta^{26}Mg$ and $^{87}Sr/^{86}Sr_i$ or εNd_i were observed for the sample suite. The lack of correlation between $\delta^{26}Mg$ and fractional crystallization indexes for MRVF rocks (e.g., SiO_2, MgO, Sm/Yb, Dy/Yb; Figure 3.16) suggests a limited role for magma differentiation on their $\delta^{26}Mg$ composition.

$\delta^{26}Mg$ has been shown to trace input from serpentinite-derived fluid and MRVF $\delta^{26}Mg$ compositions overlap with the most negative serpentinite values (Figure 3.15). However, MRVF boron compositions indicate a limited role for slab fluids on MRVF magmas (Figure 4.1) and no correlation between $\delta^{26}Mg$ and tracers of slab fluid or slab melt contribution were observed (e.g., Ba/Th, Pb/Ce, Th/Yb; Figure 4.14). Although the $\delta^{26}Mg$ data presented here do not rule serpentinite out completely, its role in the Mg isotope composition of MRVF magmas is insignificant.

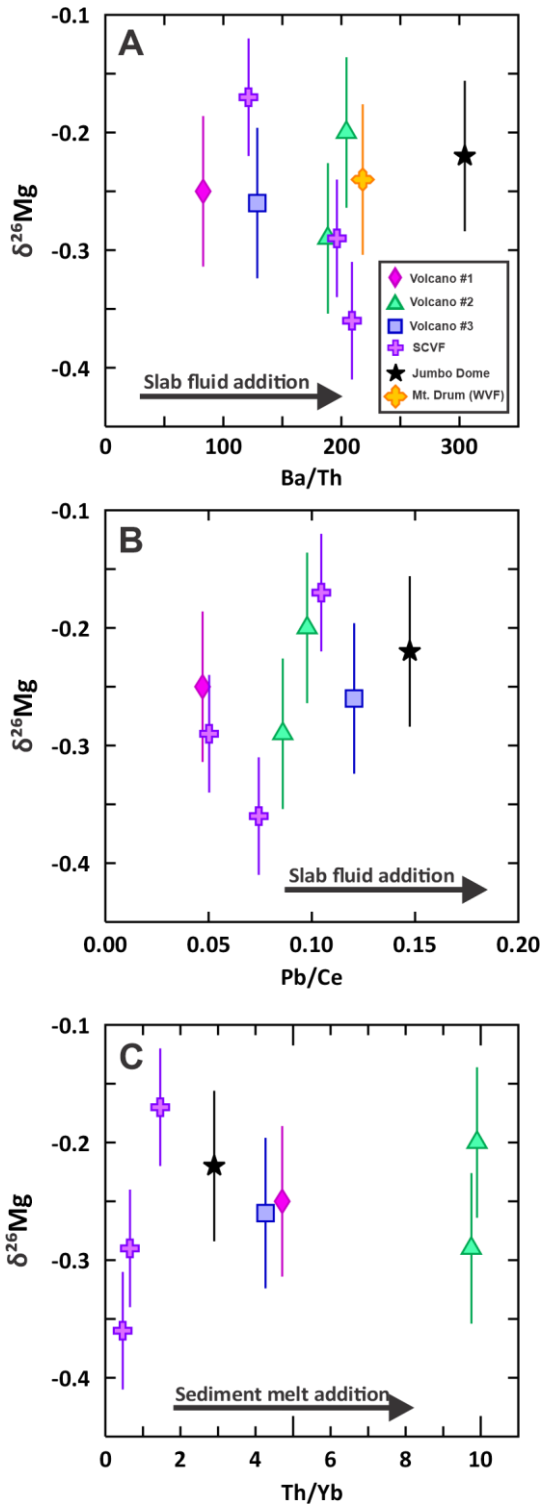

Figure 4.14: Variation of δ^{26}Mg with tracers of subduction components. (A) and (B) Ba/Th and Pb/Ce vs. δ^{26}Mg. Increases in Pb/Ce and Ba/Th ratios are typically associated with slab-derived fluid additions to the mantle. (C) Th/Yb vs. δ^{26}Mg. Subducted sediment melts are typically associated with higher Th/Yb ratios. Modified from Brewer *et al*. 2018.

MRVF Petrogenetic Model and Comparisons to Global Slab Tear Magmatism

The Yakutat slab tear is interpreted to have initiated at ca. 1 Ma due to the arrival and subsequent collision of the thickest portion of the Yakutat oceanic plateau (Worthington *et al*., 2012; Brueseke *et al*., 2023). Thus, the MRVF appears to represent the magmatic response to the Yakutat slab tear formation and directly reflects the initiation of true Yakutat slab collision. Although the geochemical signature of slab tear magmatism remains poorly characterized, as nascent slab tear volcanoes, the MRVF serves as a possible example of primary magmatism in a slab tear environment. Comparisons between the MRVF and other examples of slab tear volcanism globally are discussed below.

MRVF magmatism displays temporal-spatial age progression along ~21 km south-north transect from volcano #1 (958 ka) to volcano #2 and then volcano #3 (422 ka), and similar trenchward progressions are found in slab tear environments globally (e.g., Zhang *et al*., 2014). The Oligocene-Miocene adakitic granitoids within the Gandese arc of Southern Tibet are an excellent example of age progressive magmatism along the propagation of the Indian plate slab tear (Zhang *et al*., 2014). Here, adakitic magmatism initiated at 30-26 Ma near the eastern Himalayan syntaxis and decreases with age toward the west to 18-9 Ma, reflecting Indian slab tear initiation beneath the eastern Himalayan syntaxis and western propagation (Zhang *et al*., 2014). These rocks derive from partial melting and mixing of lower Tibetan crust with heat sourced from hot asthenosphere upwelling through the Indian slab tear.

Volcano #1 and #2 are interpreted to derive from metasomatized subcontinental lithospheric mantle. A similar scenario is observed in the Sierra de San Carlos-Cruillas Complex (SSCC) in Tamaulipas, Mexico. Here, the Hess Conjugate (a buoyant plateau-thickened slab

segment of the Farallon plate), shallowly subducted beneath Mexico before sinking and detaching from the Farallon plate (Elizondo-Pacheco *et al*., 2022). The resulting asthenospheric upwelling partially melted the overlying ancient subduction-modified subcontinental lithospheric mantle, generating the arc-like magmas far inboard of the trench (Elizondo-Pacheco *et al*., 2022).

Volcano #2 is also shoshonite-like, and shoshonitic magmatism is found elsewhere in slab tear environments. At Capraia island in the northern Tyrrhenian Sea, slab rollback of the Ionian slab resulted in a trench perpendicular slab tear that enabled upwelling asthenosphere to pass through it and partially melt the mantle, producing the Zenobito shoshonites (Rosembaum *et al*., 2008; Gasparon *et al*., 2009). These shoshonites are characterized by high HFSE and low LREE/HFSE and LREE/HREE values (e.g., La/Nb < 1.6 and Ce/Y < 3.5) which is interpreted to a stronger asthenospheric component in their source (Gasparon *et al*., 2009).

With the newly identified mantle sources for MRVF magmas, I propose a petrogenetic model for the MRVF similar to those presented above while expanding on the tectonomagmatic configuration described in Brueseke *et al.* (2023). Before 1 Ma, the buoyant Yakutat oceanic plateau obliquely subducted beneath south-central Alaska at a shallow angle with no observed volcanism within the Denali gap (Figure 4.10). By ca. 1 Ma, the thickest portion of the buoyant Yakutat oceanic plateau is introduced to the trench, marking a shift from subduction to true Yakutat oceanic plateau collision and subsequent tearing of the Yakutat slab (Brueseke *et al*., 2023). Asthenospheric upwelling through the tear may have interacted with the subduction-affected lithospheric mantle, producing the magma source of volcano #1. Heat from this upwelling asthenosphere likely provided the heat necessary to partially melt the metasomatized subcontinental lithospheric mantle (volcano #2's magma) and the eclogitic Yakutat slab which

subsequently interacted with mantle peridotite to generate the magma source of volcano #3 (Figure 4.15).

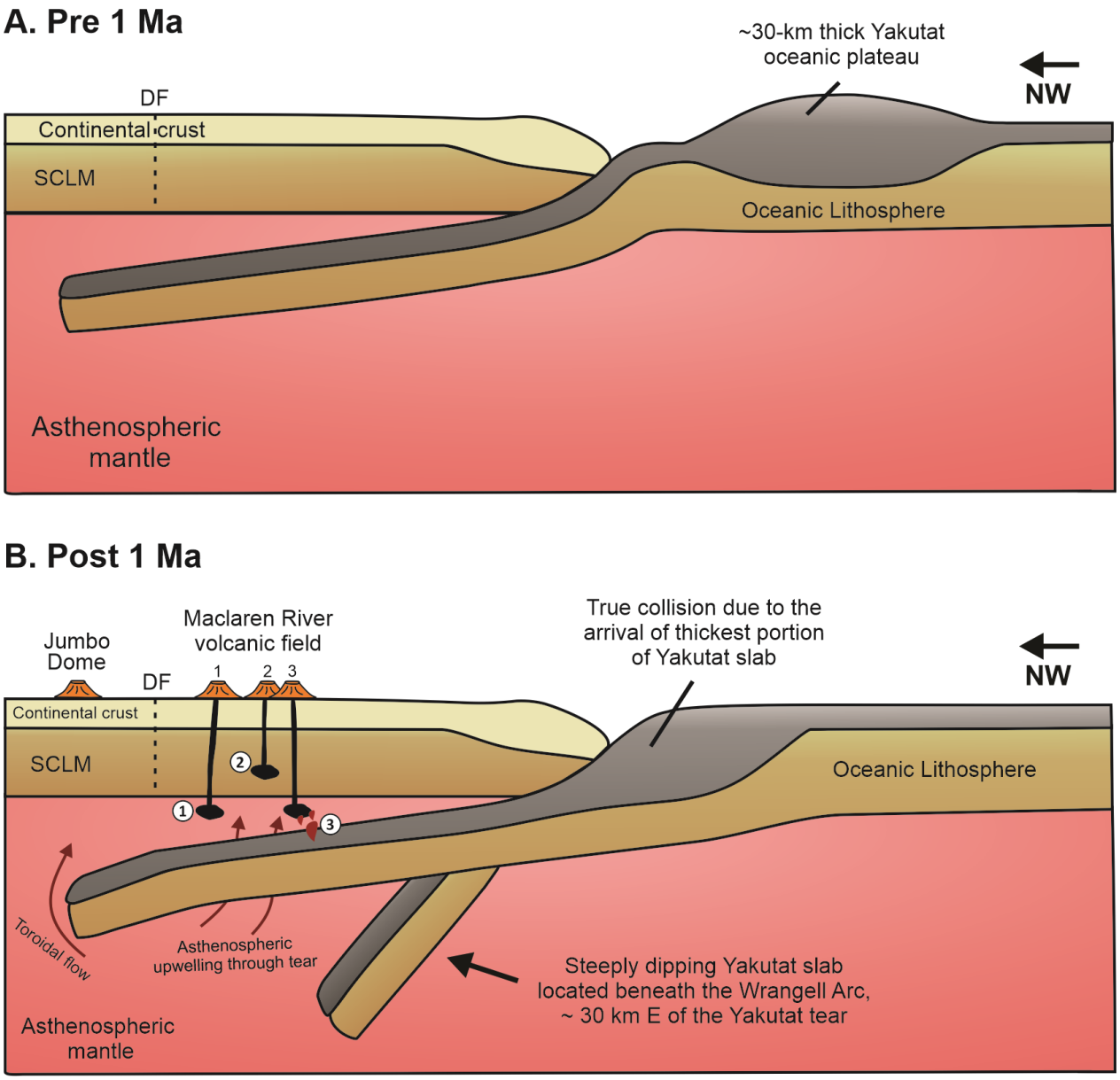

Figure 4.15: Petrogenetic model for MRVF magmatism in relation to the onset of true Yakutat oceanic plateau collision and Yakutat tear development. (A) pre 1 Ma, the buoyant Yakutat plateau subducts shallowly beneath south-central Alaska. (B) post 1 Ma, introduction of the thickest portion of the buoyant Yakutat oceanic plateau to the trench causes true collision of the Yakutat plateau and initiates the Yakutat slab tear. Asthenospheric upwelling may have provided the heat necessary to melt (1) a subduction-affected lithospheric mantle source; (2) a metasomatized subcontinental lithospheric mantle source; and (3) the eclogitic Yakutat slab. DF = Denali fault, SCLM = subcontinental lithospheric mantle.

Chapter 5 - Conclusions and Future Work

Conclusions

1. The MRVF consists of at least <1 Ma three monogenetic volcanoes, volcano #1, #2, and #3, that represent the magmatic response to the Yakutat slab tear formation ca. ~1 Ma and lie along a 21-km-long, north-south transect.
2. Eruptive products from the three MRVF slab tear volcanoes cluster into three compositional groups with different mantle sources, consistent with their monogenetic nature. All MVRF rocks display subduction signatures with LILE enrichments and HFSE depletions. Volcano #1 rocks are subalkaline, olivine-phyric basaltic andesites and likely derive from a 1-5% partial melt of a metasomatized lithospheric mantle source with a kaerustite pyroxenite composition. Volcano #2 rocks range from alkaline basalts to trachybasalts, are shoshonite-like with a hydrated mineralogy (e.g., amphibole and phlogopite), and likely derive from a 1-5% partial melt of a subcontinental lithospheric mantle source with a kaerustite pyroxenite composition. Volcano #3 rocks range from subalkaline/transitional basaltic-trachyandesites-trachyandesites-andesites, are adakitic, and likely derive from a 15-30% partial melt of an eclogitic slab that interacted with overlying mantle peridotite.
3. New Sr-Nd-Pb isotope data indicates that MRVF volcanoes are isotopically similar to modern Aleutian and Wrangell arc magmas, Siletzia terrane, Nikolai Greenstone, and the Holocene Buzzard Creek maars.
4. New Mg-B data reported here sheds light on the contribution of subducted material on MRVF magmas sources. MRVF rocks have mantle-like δ^{26}Mg compositions and overlap

with the most negative serpentinite abyssal peridotite compositions. However, MRVF B concentrations indicate a limited role for fluid metasomatism, and varying sediment melt input in the MRVF mantle sources. MRVF $\delta^{11}B$ compositions generally fall within the range for the depleted mantle, and OIB-like rocks from the Cascades; however, volcano #3 has a higher $\delta^{11}B$ composition that may reflect its slab-melt origin.

Future Work

The MRVF provides constraints on the magmatic response to Yakutat tear initiation and development, however the physical volcanology, eruption extent, and vent location of volcano #1 remains unclear due to the inaccessibility of the field site. Moreover, the MRVF geochemical dataset only includes two samples from volcano #1, therefore additional field work with the goal of identifying the eruptive vent, acquiring additional samples, and mapping the erupted extent would increase the robustness of the sample suite, constrain the erupted volume, and further constrain the petrogenesis of this volcano.

Before the fieldwork season in July 2022, remote sensing was used to search for evidence of other unrecognized volcanism in the area. While this work and previous studies by Waldien *et al*. (2022) and Brueseke *et al*. (2023) identified volcano #1, #2, and #3, the possibility of additional < 1 Ma volcanism related to the Yakutat slab tear initiation in south-central Alaska cannot be ruled out. Searching for other volcanoes, especially along the S-N transect that the MRVF lies along, would help constrain the magmatic evolution of slab tear environments by examining any geochemical trends from nascent volcanism observed in the MRVF toward magmatism with a more established slab tear. Sampling volcanic clasts along glacial moraines north of the known MRVF volcanoes discussed herein may help identify other Yakutat slab tear magmatic sources.

The petrogenetic modeling in this study was able to identify mantle sources for MRVF magmas; however, implication of more complex modeling methods may further constrain the petrogenesis of MRVF rocks. Analyzing mineral chemistry of MRVF rocks may provide further constraints on depths of last equilibration, temperature conditions, and mantle sources. In particular, analyzing the clinopyroxene phenocrysts in volcano #2 and #3 with aegirine cores would be interesting.

This study reports new Sr-Nd-Pb isotopic data for the MRVF; however, results from radiogenic isotopic analyses of DEN20-13 (volcano #2) and Jumbo Dome are not available yet. Once these data are available, comparing the Sr-Nd-Pb composition of DEN20-13 to the rest of the MRVF suite may provide constraints on its petrogenesis because this sample is the only basalt from volcano #2 (SiO_2 = 4.96 wt%), while the rest are trachybasalts. Comparison of new radiogenic isotopic data from Jumbo Dome to the MRVF may further constrain the MRVF's petrogenesis.

References

Agostini, S., Di Guiseppe, P., Manetti, P., Doglioni, C. & Conticelli, S. (2021). A heterogenous subcontinental mantle under the African-Arabian Plate boundary revealed by boron and radiogenic isotopes. *Scientific Reports* **11**, 11230, https://doi.org/10.1038/s41598-021-90275-7.

Albanese, M. (1980). The Geology of three extrusive bodies in the Central Alaska Range. University of Alaska Fairbanks, unpublished M.S. thesis, 104 p.

Aldanmaz, E., Pearce, J.A., Thirwall, M.F., & Mitchell, J.G. (2000). Petrogenetic evolution of late Cenozoic, post-collision volcanism in western Anatolia, Turkey. *Journal of Volcanology and Geothermal Research* **102**, 67-95, https://doi.org/10.1016/S0377-0273(00)00182-7.

Aleinikoff, J.N., & Nokleberg, W.J. (1985). *Age of Devonian igneous-arc terranes in the northern Mount Hayes quadrange, eastern Alaska Range*. In: Bartsch-Winker, S. (ed.). The United States Geological Survey in Alaska: accomplishments during 1984, United States Geological Survey Circular 967, 44-49.

Aleinikoff, J.N., Dusel-Bacon, C., Foster, H.L., & Nokleberg, W.J. (1987). Lead isotopic fingerprinting of tectono-stratigraphic terranes, east-central Alaska. *Canadian Journal of Earth Sciences* **24**(10), 2089-2098, https://doi.org/10.1139/e87-198.

Aleinikoff, J.N., Farmer, G.L, Rye, R.O., & Nokleberg, W.J. (2000). Isotopic evidence for the sources of Cretaceous and Tertiary granitic rocks, east-central Alaska: implications for the tectonic evolution of the Yukon-Tanana Terrane. *Canadian Journal of Earth Sciences* **37**, 945-946, https://doi.org/10.1139/e00-006.

Andronikov, A.V., & Mukasa, S.B. (2010). $^{40}Ar/^{39}Ar$ eruption ages and geochemical characteristics of Late Tertiary to Quaternary intraplate and arc-related lavas in interior Alaska. *Lithos* **115**, 1-14, https://doi.org/10.1016/j.lithos.2009.11.002.

Atherton, M.P., & Petford, N. (1993). Generation of sodium-rich magmas from newly underplated basaltic crust. *Nature* **362**, 144-146, https://doi.org/10.1038/362144a0.

Athey, J.E., Newberry, R.J., Werdon, M.B., Freeman, L.K., Smith, R.L., & Szumigala, D.J. (2006). Bedrock geologic map of the Liberty Bell area, Fairbanks A-4 Quadrangle, Bonnifield mining district, Alaska. *Alaska Division of Geological and Geophysical Surveys Report of Investigation* **2006-2**, v. 1.0.1, 98 p., 1 sheet, scale 1:50,000, https://doi.org/10.14509/15026.

Berg, H.C., Jones, D.L., & Richter, D.H. (1972). The Gravina-Nutzotin Belt-Tectonic significance of an Upper Mesozoic sedimentary and volcanic sequence in southern and southeastern Alaska. *U.S. Geological Survey Professional Paper 800-D*, p. D1-D24.

Berkelhammer, S.E. (2017). Initiation of the Wrangell arc: A record of tectonic changes in an arc-transform junction revealed by new geochemistry and geochronology of the ~29-18 Ma

Sonya Creek volcanic field, Alaska. Kansas State University, unpublished M.S. thesis, 217 p.

Berkelhammer, S.E., Brueseke, M.E., Benowitz, J.A., Trop, J.M., Davis, K., Layer, P.W., & Weber, M. (2019). Geochemical and geochronological records of tectonic changes along a flat-slab arc-transform junction: Circa 30 ma to ca. 19 Ma Sonya Creek volcanic field, Wrangell Arc, Alaska. *Geosphere* **15**, 1508-1538, https://doi.org/10.1130/GES02114.1.

Boschi, C., Dini, A., Früh-Green, G.L., & Kelley, D.S. (2008). Isotopic and element exchange during serpentinization and metasomatism at the Atlantis Massif (MAR 30°N): Insights from B and Sr isotope data. *Geochimica et Cosmochimica Acta* **72**, 1801-1823, https://doi.org/10.1016/j.gca.2008.01.013.

Botazzi, P., Tiepolo, M., Vannucci, R., Zanetti, A., Brumm, R., Foley, S.F., & Oberti, F. (1999). Distinct site preferences for heavy and light REE in amphibole and the prediction of Amph/LDREE. *Contributions to Mineralogy and Petrology* **137**, 36-45, https://doi.org/10.1007/s004100050580.

Bouvier, A., Vervoort, J.D., & Patchett, P.J. (2008). The Lu-Hf and Sm-Nd isotopic composition of CHUR: Constraints from unequilibrated chondrites and implications for the bulk composition of terrestrial planets. *Earth and Planetary Science Letters* **273**, 1-2, 48-57, https://doi.org/10.1016/j.epsl.2008.06.010.

Brennan, P., Ridgway, K.D., Witmer, J., & Valencia, V.A. (2009). Stratigraphy and provenance of the Poul Creek Formation in the Chugach-St. Elias Mountains, southeast Alaska: Insights on Eocene-Miocene sedimentation in the Gulf of Alaska. *Geological Society of America Abstracts with Programs* **41**, 306.

Brewer, A.W., Teng, F.-Z., & Mullen, E. (2018). Magnesium isotopes as a tracer of crustal materials in volcanic arc magmas of the Northern Cascade Arc. *Frontiers in Earth Science* **6**, https://doi.org/10.3389/feart.2018.00021.

Brown, K., Hart, W.K., & Stuck, R.J. (2018). Temporal and geochemical signatures in granitoids of northwestern Nevada: Evidence for the continuity of the Mesozoic magmatic arc through the western Great Basin. *Lithosphere* **10**, 327-350, https://doi.org/10.1130/L694.1.

Brueseke, M.E., Callicoat, J.S., Hames, W., & Larson, P.B. (2014). Mid-Miocene rhyolite volcanism in northeastern Nevada: The Jarbridge Rhyolite and its relationship to the Cenozoic evolution of the northern Great Basin (USA). *GSA Bulletin* **126** (7-8), 1047-1067, https://doi.org/10.1130/B30736.1

Brueseke, M.E., Benowitz, J.A., Trop, J.M., Davis, K.N., Berkelhammer, S.E., Layer, P.W., & Morter, B.K. (2019). The Alaska Wrangell Arc: ~30 m.y. of subduction-related magmatism along a still active arc-transform junction. *Terra Nova* **31**, 59-66, https://doi.org/10.1111/ter.12369.

Brueseke, M.E., Benowitz, J.A., Bearden, A.T., Mann, M.E., & Miggins, D.P. (2023). Subduction disruption, slab tears: ca. 1 Ma true collision of an ~30-km-thick oceanic plateau segment

recorded by Yakutat slab nascent tear magmatism. *Terra Nova* **35**, 49-57, https://doi.org/10.1111/ter.12628.

Cameron, C.E., Nye, C.J., Bull, K.F., & Woods, R-E. (2015). Jumbo Dome, Interior Alaska: Whole-rock, major- and trace-element analysis. Alaska Division of Geological and Geophysical Surveys Raw Data File 2015-14, 3p., https://doi.org/10.14509/29520.

Castillo, P.R. (2012). Adakite petrogenesis. *Lithos* **134-135**, 304-316, https://doi.org/10.1016/j.lithos.2011.09.013.

Chan, C.F., Tepper, J.H., & Nelson, B.K. (2012). Petrology of the Grays River volcanics, southwest Washington: Plume-influenced slab window magmatism in the Cascadia forearc. *GSA Bulletin* **124** (7-8), 1324-1338, https://doi.org/10.1130/B30576.1.

Chauvel, C., & Blichert-Toft, J. (2001). A hafnium isotope and trace element perspective on melting on the depleted mantle. *Earth and Planetary Science Letters* **190**, 137-151, https://doi.org/10.1016/S0012-821X(01)00379-X.

Christeson, G.L., Van Avendonk, H.J.A., Gulick, S.P.S., Reece, R.S., Pavlis, G.L., & Pavlis, T.L. (2010). Moho interface beneath Yakutat terrane, southern Alaska. *Journal of Geophysical Research: Solid Earth* **118**, 5084-5097, https://doi.org/10.1002/jgrb.50361.

Chuang, L., Bostock, M., Wech, A., & Plourde, A. (2017). Plateau subduction, intraslab seismicity, and the Denali (Alaska) volcanic gap. *Geology* **45**(7), 647-650, https://doi.org/10.1130/G38867.1.

Ciborowski, T.J.R., Phillips, B.A., Kerr, A.C., Barfod, D.N., & Mark, D.F. (2020). Petrogenesis of Siletzia: The world's youngest oceanic plateau. *Results in Geochemistry* **1**, https://doi.org/10.1016/j.ringeo.2020.100004.

Class, C., Miller, D.M., Goldstein, S.L., & Langmuir, C.H. (2000). Distinguishing melt and fluid subduction components in Umnak Volcanics, Aleutian Arc. *Geochemistry, Geophysics, Geosystems **1***, 1004, https://doi.org/10.1029/1999GC000010.

Clift, P.D., Draut, A.E., Kelemen, P.B., Blusztajn, J., & Greene, A. (2005). Stratigraphic and geochemical evolution of an oceanic arc upper crustal section: The Jurassic Talkeetna Volcanic Formation, south-central Alaska. *Geological Society of America Bulletin* **117**, p. 902-925.

Cole, R.B., & Stewart, B.W. 2009. Continental margin volcanism at sites of spreading ridge subduction: Examples from southern Alaska and western California. *Tectonophysics* **464** (1-4), 118-136, https://doi.org/10.1016/j.tecto.2007.12.005.

Coleman, R.G., Lee, D.E., Beatty, L.B., & Brannock, W.W. (1965). Eclogites and Eclogites: Their differences and similarities. *Geological Society of America Bulletin* **76**, 483-508.

Conrey, R.M., Bailey, D.G., Singer. J.W., Wagoner, L., Parfitt, B., Hay, J., & Key, O. (2019). Optimization of internal standards in LA-ICPMS analysis of geologic samples using

lithium borate fused glass. *Geological Society of America Abstracts with Programs* **51**, 1, https://doi.org/10.1130/abs/2019NE-328672.

Conrey, R.M., Bailey, D.G., Singer, J.W., Wagoner, L.J., Parfitt, B., Hay, J., Keh, O., Chang, Z., & Huang, S. (2023). Combined use of multiple external and internal standards in LA-ICP-MS analysis of bulk geological samples using lithium borate fused glass. *Geochemical: Exploration, Environment, Analysis* **23**, https://doi.org/10.1144/geochem2023-001.

Daly, K.A., Abers, G.A., Mann, M.E., Roecker, S., & Christensen, D.H. (2021). Subduction of an oceanic plateau across south-central Alaska: High-resolution seismicity. *Journal of Geophysical Research: Solid Earth* **126**, e2021JB022809, https://doi.org/10.1029/2021JB022809.

Defant, M.J., & Drummond, M.S. (1990). Derivation of some modern arc magmas by melting of young subducted lithosphere. *Nature* **347**, 662-665, https://doi.org/10.1038/347662a0.

DePaolo, D.J., (1981). Trace element and isotopic effects of combined wallrock assimilation and fractional crystallization. *Earth and Planetary Science Letters* **53**, 189-202,

De Hoog, J.C.M., & Savov, I.P. (2018). *Boron Isotopes as a Tracer of Subduction Zone Processes*. In: Marschall, H., & Foster, G. (eds.) Boron Isotopes. *Advances in Isotope Geochemistry*. Springer, Cham, https://doi.org/10.1007/978-3-319-64666-4_9.

Elizondo-Pacheco, L.A., Ramírez-Fernández, J.A., De Ignacio, C., González-Guzmán, R., Rodríguez-Saavedra, P., Leal-Cuellar, V.A., Velasco-Tapia, F., & Montalvo-Arrieta, J.C. (2022). Generation of arc-like and OIB-like magmas trigged by slab detachment in the Eastern Mexican Alkaline Province: Petrological evidence from the Cenozoic Sierra de San Carlos-Cruillas Complex, Tamaulipas. *Journal of Petrology* **63**, 5, egac027, https://doi.org/10.1093/petrology/egac027.

Elkins, L.J., Gaetani, G.A., & Sims, K.W.W. (2008). Partitioning of U and Th during garnet pyroxenite partial melting: Constraints on the source of alkaline oceanic basalts. *Earth and Planetary Science Letters* **265**, 270-286, https://doi.org/10.1016/j.epsl.2007.10.034.

Enkelmann, E., Zeitler, P.K., Garver, J.I., Pavlis, T.L., & Hooks, B.P. (2010). The thermochronological record of tectonic and surface process interaction at the Yakutat-North American collision zone in southeast Alaska. *American Journal of Science* **310**, 231-260, https://doi.org/10.2475/04.2010.01.

Finzel, E.S., Trop, J.M., Ridgeway, K.D., & Enkelmann, E. (2011). Upper plate proxies for flat-slab subduction processes in southern Alaska. *Earth and Planetary Science Letters* **303**, 348-360, https://doi.org/10.1016/j.epsl.2011.01.014.

Finzel, E.S., Enkelmann, E., Falkowski, S., & Hedeen, T. (2016). Long-term fore-arc basin evolution in response to changing subduction styles in southern Alaska. *Tectonics* **35**, 1735-1759, https://doi.org/10.1002/2016TC004171.

Foster, G.L., Lécuyer, C., & Marschall H.R. (2016). *Boron stable isotopes*. In: White, W. (eds.) Encyclopedia of Geochemistry. *Encyclopedia of Earth Sciences Series*. Springer, Cham, https://doi.org/10.1007/978-3-319-39193-9_238-1.

Fuis, G.S., Moore, T.E., Plafker, G., Brocher, T.M., Fischer, M.A., Mooney, W.D., Nokleberg, W.J., Page, R.A., Beaudoin, B.C., Christensen, N.I., Levander, A.R., Lutter, W.J., Saltus, R.W., & Ruppert, N.A. (2008). Trans-Alaska Crustal Transect and continental evolution involving subduction underplating and synchronous foreland thrusting. *Geology* **36** (3): 267-270, https://doi.org/10.1130/G24257A.1.

Gasparon, M., Rosenbaum, G., Wijbrans, J., & Manetti, P. (2009). The transition from subduction arc to slab tearing: Evidence from Capraia Island, northern Tyrrhenian Sea. *Journal of Geodynamics* **47**, 30-38, https://doi.org/10.1016/j.jog.2008.06.004.

Gazel, E., Hoernle, K., Carr, M.J., Herzberg, C., Saginor, I., van den Bogaard, P., Hauff, F., Feigenson, M., & Swisher, C.III. (2011). Plume-subduction interaction in southern Central America: Mantle upwelling and slab melting. *Lithos* **121**, 117-134, https://doi.org/10.1016/j.lithos.2010.10.008.

Green, T.H., & Pearson, N.J. (1983). Effect of pressure on rare earth element partition coefficients in common magmas. *Nature* **305**, 414-416, https://doi.org/10.1038/305414a0.

Greene, A.R., Scoates, J.S., & Weis, D. (2008). Wrangellia flood basalts in Alaska: A record of plume-lithosphere interaction in a Late Triassic accreted oceanic plateau. *Geochemistry, Geophysics, Geosystems* **9**, q12004, https://doi.org/10.1029/2008GC002092.

Greene, A.R., Scoates, J.S., Wise, S., & Israel, S. (2009). Geochemistry of Triassic flood basalts from the Yukon (Canada) segment of the accreted Wrangellia oceanic plateau. *Lithos* **110** (1-4), 1-19, https://doi.org/10.1016/j.lithos.2008.11.010.

Gulick, S.P.S., Reece, R.S., Christeson, G.L., van Avendonk, H., Worthington, L.L., & Pavlis, T.L. (2013). Seismic images of the Transition fault and the unstable -Yakutat-Pacific-North American triple junction. *Geology* **41**(5), 571-574, https://doi.org/10.1130/G33900.1.

Gutscher, M-A., Spakman, W., Bijwaard, H., & Engdahl, E.R. (2000). Geodynamics of flat subduction: Seismicity and tomographic constraints from Andean margin. *Tectonics* **19**, 5, 814-833, https://doi.org/10.1029/1999TC001152.

Harvey, J., Savov, I.P., Agostini, S., Cliff, R.A., & Walshaw, R. (2014). Si-metasomatism in serpentinized peridotite: The effects of tac-alteration on strontium and boron isotopes in abyssal serpentinites from Hole 1268a, ODP Leg 209. *Geochemica et Cosmochimica Acta* **126**, 30-48, https://doi.org/10.1016/j.gca.2013.10.035.

Hart, S.R., & Dunn, T. (1993). Experimental cpx/melt partitioning of 24 trace elements. *Contributions to Mineralogy and Petrology* **113,** 1-8, https://doi.org/10.1007/BF00320827.

Hao, L.L., Nan, X.Y., Kerr, A.C., Li, S.Q., Wu, Y.B., Wang, H., & Huang, F. (2022). Mg-Ba-Sr-Nd isotopic evidence for a mélange origin of early Paleozoic arc magmatism. *Earth and Planetary Science Letters* **577**, 117263, https://doi.org/10.1016/j.epsl.2021.11726.

Hauri, E.H., Wagner, T.P., & Grove, T.L. (1994). Experimental and natural partitioning of Th, U, Pb, and other trace element between garnet, clinopyroxene and basaltic melts. *Chemical Geology* **117**, 149-166, https://doi.org/10.1016/0009-2541(94)90126-0.

Hu, F., Liu, S., Zhang, W., Deng, Z., & Chen, X. (2016). A westward propagating slab tear model for Late Triassic Qinling Orogenic Belt geodynamic evolution: Insights from the petrogenesis of the Caoping and Shahewan intrusions, central China. *Lithos* **262**, 486-506, https://doi.org/10.1016/j.lithos.2016.07.034.

Hu, Y., Teng, F.-Z., Plank, T., & Huang, K.-J. (2017). Magnesium isotopic composition of subducting marine sediments. *Chemical Geology* **466**, 15-31, https://doi.org/10.1016/j.chemgeo.2017.06.010.

Hu, F., Teng, F.-Z., & Ionov, D.A. (2020). Magnesium isotopic composition of metasomatized upper sub-arc mantle and its implications to Mg cycling in subduction zones. *Geochemical et Cosmochimca Acta* **278**, 219-234, https://doi.org/10.1016/j.gca.2019.09.030.

Huang, J., Ke, S., Gao, Y., Xiao, Y., & Li, S. (2015). Magnesium isotopic compositions of altered oceanic basalts and gabbros from IODP site 1256 at the East Pacific Rise. *Lithos* **231**, 53-61, https://doi.org/10.1016/j.lithos.2015.06.009.

Huang, K-J., Teng, F-Z., Plank, T., Staudigel, H., Hu, Y., & Bao, Z-Y. (2018). Magnesium isotopic composition of altered oceanic crust and the global Mg cycle. *Geochimica et Cosmochimica Acta* **238**, 357-373, https://doi.org/10.1016/j.gca.2018.07.011.

Hyeong, K., Kim, J., Pettke, T., Yoo, C.M., & Hur, S.D. (2011). Lead, Nd, and Sr isotope records of pelagic dust: Source indication versus the effects of dust extraction procedures and authigenic mineral growth. *Chemical Geology* **286**, 240-251.

Irvine, T.N., & Baragar, W.R.A. (1971). A guide to the chemical classification of the common volcanic rocks. *Canadian Journal of Earth Sciences* **8**(5), 523-548, https://doi.org/10.1139/e71-055.

Ishikawa, T., & Nakamura, E. (1994). Origin of the slab component in arc lavas from across-arc variation of B and Pb isotopes. *Nature* **370**, 205-208, https://doi.org/10.1038/370205a0.

Ishikawa, T., & Tera, F. (1997). Source, composition, and distribution of the fluid in the Kurile mantle wedge: Constraints from across-arc variations of B/Nb and B isotopes. *Earth and Planetary Science Letters* **152**, 123-138, https://doi.org/10.1016/S0012-821X(97)00144-1.

Ishikawa, T., & Tera, F. (1999). Two isotopically distinct fluid components involved in the Mariana arc: Evidence from Nb/B ratios and B, Sr, Nd, and Pb isotope systematics. *Geology* **27**, 83-86, https://doi.org/10.1130/0091-7613(1999)027<0083:TIDFCI>2.3.CO;2.

Ishikawa, T., Tera, F., & Nakazawa, T. (2001). Boron isotope and trace element systematics of the three volcanic zones in the Kamchatka arc. *Geochimica et Cosmochimca Acta* **65**, 4523-4537, https://doi.org/10.1016/S0016-7037(01)00765-7.

Ke, S., Teng, F.-Z., Li, S.-G., Gao, T., Liu, S.-A., He, Y., & Mo, X. (2016). Mg, Sr, and O isotope geochemistry of syenites from northwest Xinjiang, China: Tracing carbonate recycling during Tethyan oceanic subduction. *Chemical Geology* **437**, 109-119, https://doi.org/10.1016/j.chemgeo.2016.05.002.

Kelemen, P.B., Yogodzinski, G.M., & Scholl, D.W. (2003). Along-strike variation in the Aleutian Island Arc: Genesis of high Mg# andesite and implications for continental crust. In: J. Eiler, (ed.) *Inside the Subduction Factory*, https://doi.org/10.1029/138GM11.

Király, Á., Portner, D.E., Haynie, K.L., Chilson-Parks, B.H., Ghosh, T., Jadamec, M., Makushkina, A., Magma, M., Moresi, L., & O'Farrell, K.A. (2020). The effect of slab gaps on subduction dynamics and mantle upwelling. *Tectonophysics* **785**, 228458, https://doi.org/10.1016/j.tecto.2020.228458.

Klemme, S., Prowatke, S., Hametner, K., & Günther, D. (2005). Partitioning of trace elements between rutile and silicate melts: Implications for subduction zones. *Geochimica et Cosmochimica Acta* **69,** 2361-2371, https://doi.org/10.1016/j.gca.2004.11.015.

Jicha, B.R., Singer, B.S., Brophy, J.G., Fournella, J.H., Johnson, C.M., Beard, B.L., Lapen, T.J., & Mahlen, N.J. (2004). Variable impact of the subducted slab on Aleutian Island Arc magma sources: evidence from Sr, Nd, Pb and Hf isotopes and trace element abundances. *Journal of Petrology* **45**, 1845-1875, https://doi.org/10.1093/petrology/egh036.

Lassiter, J.C., DePaolo, D.J., & Mahoney, J.J. (1995). Geochemistry of the Wrangellia flood basalt province: Implications for the role on continental and oceanic lithosphere in flood basalt genesis. *Journal of Petrology* **36**, 983-1009, https://doi.org/10.1093/petrology/36.4.983.

Lease, R.O., Haeussler, P.J., & O'Sullivan, P. (2016). Changing exhumation patterns during Cenozoic growth and glaciation of the Alaska Range: Insights from detrital thermochronology and geochronology. *Tectonics* **35**, 934-955, https://doi.org/10.1002/2015TC004067.

Le Bas, M.J., Le Maitre, R.W., Streckeisen, A., & Zanettin, B.A. (1986). Chemical classification of volcanic rocks based on the total alkali-silica diagram. *Journal of Petrology* **27**, 745-750, https://doi.org/10.1093/petrology/27.3.745.

Leeman, W.P., Tonarini, S., Chan, L.H., & Borg, L.E. (2004). Boron and lithium isotopic variations in a hot subduction zone – the southern Washington Cascades. *Chemical Geology* **212**, 101-124, https://doi.org/10.1016/j.chemgeo.2004.08.010.

Lemarchand, F., Benoit, V., & Calais, G. (1987). Trace element distribution coefficients in alkaline series. *Geochemica et Cosmochimca Acta* **51**, 1071-1081, https://doi.org/10.1016/0016-7037(87)90201-8.

Le Maitre, R., Streckeisen, A., Zanettin, B., Le Bas, M., Bonin, B., & Bateman, P. (eds.) (2002). Igneous Rocks: A classification and glossary of terms: Recommendations of the International Union of Geological Sciences Subcommision on the Systematics of Igneous Rocks (2^{nd} ed.). Cambridge: Cambridge University Press. https://doi.org/10.1017/CBO9780511535581.

Li, S.-G., Yang, W., Ke, S., Meng, X., Tian, H., Xu, L., He, Y., Huang, J., Wang, X.-C., Xia, Q., Sun, W., Yang, x., Ren, Z.-Y., Wei, H.,Liu, Y., Meng, F., & Yan, J. (2017). Deep carbon cycles constrained by a large-scale mantle Mg isotope anomaly in eastern China. *National Science Review* **4**(1), 111-120, https://doi.org/10.1093/nsr/nww070.

Liu, P.-P., Teng, F.-Z., Dick, H.J.B., Zhou, M.-F., & Chung, S.-L. (2017). Magnesium isotopic composition of the oceanic mantle and oceanic Mg cycling. *Geochimica et Cosmochimica Acta* **206**, 151-165, https://doi.org/10.1016/j.gca.2017.02.016.

Mann, M.E., Abers, G.A., Daly, K., & Christensen, D.H. (2022). Subduction of an oceanic plateau across southcentral Alaska: Scattered-wave imaging. *Journal of Geophysical Research: Solid Earth* **127**, e2021JB022697, https://doi.org/10.1029/2021JB022697.

Manuszack, J.D., Ridgway, K.D., Trop, J.M., & Gehrels, G.E. (2007). Sedimentary record of tectonic growth of a collisional continental margin: Upper Jurassic-Lower Cretaceous Nutzotin Mountains sequence, eastern Alaska Range, Alaska. In: Ridgway, K.D., Trop, J.N., O'Niell, J.M., & Glen, J.M.D., (eds.) *Tectonic growth of a collisional continental margin: Crustal evolution of southern Alaska*. *Geological Society of America Special Paper* **431**, 345-377, https://doi.org/10.1130/2007.2431(14).

Marschall H.R., Wanless, V.D., Shimizu, N., Pogge von Strandmann, P.A.E., Elliott, T., & Monteleone, B.D. (2017). The boron and lithium isotopoic composition of mid-ocean ridge basalts and the mantle. *Geochemica et Cosmochimica Acta* **207**, 102-138, https://doi.org/10.1016/j.gca.2017.03.028.

Martin-Short, R., Allen, R., Bastow, I.D., Porritt, R.W., & Miller, M.S. (2018). Seismic imaging of the Alaska Subduction Zone: Implications for Slab Geometry and Volcanism. *Geochemistry, Geophysics, Geosystems* **19**, 4541-4560, https://doi.org/10.1029/2018GC007962.

Manselle, P., Brueseke, M.E., Trop, J.M., Benowitz, J.A., Snyder, D.C. & Hart, W.K. (2020). Geochemical and stratigraphic analysis of the Chisana Formation, Wrangellia terrane, eastern Alaska: Insights into Earth Cretaceous magmatism and tectonics along the northern Cordilleran Margin. *Tectonics* **39,** e2020TC006131, https://doi.org/10.1029/2020TC006131.

Matsui, A., Onuma, N., Nagasawa, H., Higuchi, H., & Banno, S. (1977). Crystal structure control in trace element partition between crystal and magma. *Bull Soc Fr Mineral Cristallogr* **100**, 315-324.

McCallum, I.S., & Charette, M.P. (1978). Zr and Nb partition coefficients: Implications for the genesis of mare basalts, KREEP and sea floor basalts. *Geochimica et Cosmochimica Acta* **42**, 859-869, https://doi.org/10.1016/0016-7037(78)90098-4.

McLennan, S.M., Taylor, S.R., McCulloch, M.T., & Maynard, J.B. (1990). Geochemical and Nd-Sr isotopic composition of deep-sea turbidites: Crustal evolution and plate tectonic associations. *Geochemica et Cosmochimica Acta* **54**, 2015-2050, https://doi.org/10.1016/0016-7037(90)90269-Q.

McLeod, O.E., Brenna, M., Briggs, R.M., & Pittari, A. (2022). Slab tear as a cause of coeval arc-intraplate volcanism in the Alexandra Volcanic Group, New Zealand. *Lithos* **408-409**, 106564, https://doi.org/10.1016/j.lithos.2021.106564.

Moriguti, T., Shibiata, T., & Nakamura, E. (2004). Lithium, boron, and lead isotope and trace element systematics of Quaternary basaltic volcanic rocks in northeastern Japan: mineralogical controls on slab-derived fluid composition. *Chemical Geology* **212**, 81-100, https://doi.org/10.1016/j.chemgeo.2004.08.005.

Morris, J.D., Leeman, W.P., & Tera, F. (1990). The subducted component in island arc lavas: constraints from Be isotopes and B-Be systematics. *Nature* **344**, 31-36, https://doi.org/10.1038/344031a0.

Navarrete, C.R., Massaferro, G.I., Gianni, G.A., & Lastra, M.B. (2021). The slab gap-related Late Cretaceous-Paleocene magmatism of southern Patagonia. *Journal of Geodynamics* **147**, 101869, https://doi.org/10.1016/j.jog.2021.101869.

Nielsen, R.L., Gallahan, W.E., & Newberger, F. (1992). Experimentally determined mineral-melt partition coefficients for Sc, Y, and REE for olivine, orthopyroxene, pigeonite, magnetite, and ilmenite. *Contributions to Mineralogy and Petrology* **110**, 488-499, https://doi.org/10.1007/BF00344083.

Nokleberg, W.J., & Aleinikoff, J.N. (1985). *Summary of stratigraphy, structure, and metamorphism of Devonian igneous-arc terranes, northeastern Mount Hayes quadrangle, eastern Alaska Range*. In: Bartsch-Winkler, S. (ed.). The United States Geological Survey in Alaska: accomplishments during 1984. *United States Geological Survey Circular 967*, 66-71

Nye, C.J., Beget, J.E., Layer, P.W., Mangan, M.T., McConnell, V.S., McGimsey, R.G., Miller, T.P., Moore, R.B., & Stelling, P.L. (2018). Geochemistry of some quaternary lavas from eh Aleutian Arc and Mt. Wrangell. Alaska Division of Geological & Geophysical Surveys Raw Data File 2018-1, 29 p., http://doi.org/10.14509/29843.

Peccerillo A., & Taylor, S.R. (1976). Geochemistry of Eocene calc-alkaline volcanic rocks from the Kastamonu area, Northern Turkey. *Contributions to Mineralogy and Petrology* **58**, 63-81, https://doi.org/10.1007/BF00384745.

Pe-Piper, G., Piper, D.J.W., Koukouvelas, I., Dolanksy, L.M., & Kokkalas, S. (2009). Postorogenic shoshonitic rocks and their origin by melting underplated basalts: The Miocene of Limnos, Greece. *GSA Bulletin* **121**, 39-54, https://doi.org/10.1130/B26317.1.

Plafker, G., & Berg, H.C. (1994). Overview of the geology and tectonic evolution of Alaska. In: Plafker, G., & Berg, H.C., (eds.) The Geology of Alaska. *Geological Society of America*, Boulder, Colo, 989-1021.

Plafker, G., Moore, J.C., & Winkler, G.R. (1994). Geology of the south Alaska margin. In: Plafker, G., & Berg, H.C., (eds.) The Geology of Alaska. *Geological Society of America*, Boulder, Colo, 389-448.

Plank, T., & Langmuir, C. (1998). The chemical composition of subducting sediment and its consequences for the crust and mantle. *Chemical Geology* **145**, 325-394, https://doi.org/10.1016/S0009-2541(97)00150-2.

Preece, S.J. (1997). Geochemical variation in the <5 Ma Wrangell Volcanic Field, Alaska with an emphasis on the Skookum Creek Volcanic Complex. Miami University, Ph.D. dissertation, 547 p.

Prelević, D., Akal, C., Romer, R.L., Mertz-Kraus, R., & Helvacı, C. (2015). Magmatic response to slab tearing: Constraints from the Afyon Alkaline Volcanic Complex, Western Turkey. *Journal of Petrology* **56**, 3, 527-562, https://doi.org/10.1093/petrology/egv008.

Prowatke, S., & Klemme, S. (2005). Effect of melt composition on the partitioning of trace elements between titanite and silicate melt. *Geochemica et Cosmochimca Acta* **69**, 695-709, https://doi.org/10.1016/j.gca.2004.06.037.

Rapp, R.P., Watson, E.B., & Miller, C.F. (1991). Partial melting of amphibolite/eclogite and the origin of Archean trondhjemites and tonalites. *Precambrian Research* **51**, 1-25, https://doi.org/10.1016/0301-9268(91)90092-O.

Richter, D.H., Smith, J.G., Lanphere, M.A., Dalrymple, G.B., Reed, B.L., & Shew, N. (1990). Age and progression of volcanism, Wrangell volcanic field, Alaska. *Bulletin of Volcanology* **53**, 29-44, https://doi.org/10.1007/BF00680318.

Rioux, M., Hacker, B., Mattinson, J., Kelemen, P., Blusztajn, J., & Gehrels, G. (2007). Magmatic development of an intra-oceanic arc: High-precision U-Pb zircon and whole-rock isotopic analysis from the accreted Talkeetna arc, south-central Alaska. *Geologic Society of America Bulletin* **119**, 1168-1184, https://doi.org/10.1130/B25964.1.

Rollinson, H.R. (1993). *Using Geochemical Data: Evaluation, presentation, interpretation*. Longman Group UK LTD., 352 p.

Rollinson, H.R., & Pease, V. (2021). *Using Geochemical Data: To Understand Geological Processes*. Cambridge, Cambridge University Press, 346 p.

Rondenay, S., Montési, & Abers, G.A. (2010). New geophysical insight into the origin of the Denali volcanic gap. *Geophysical Journal International* **182**(2), 613-630, https://doi.org/10.1111/j.1365-246X.2010.04659.x.

Rosenbaum, G., Gasparon, M., Lucente, F.P., Peccerillo, A., & Miller, M.S. (2008). Kinematics of slab tear faults during subduction segmentation and implications for Italian magmatism. *Tectonics* **27**, TC2008, https://doi.org/10.1029/2007TC002143.

Rosner, M., Erzinger, J., Franz, G., & Trumbull, R.B. (2003). Slab-derived boron isotope signatures in arc volcanic rocks from the Central Andes and evidence for boron isotope fractionation during progressive slab dehydration. *Geochemistry, Geophysics, Geosystems* **4**, 9005, https://doi.org/10.1029/2002GC000438.

Rosman, K.J.R., & Taylor, P.D.P. (1998). Isotopic compositions of the elements. *Pure & Applied Chemistry* **70**, 217-225, https://doi.org/10.1351/pac199870010217.

Sajona, F.G., Maury, R.E., Bellon, H., Cotton, J., Defant, M.J., & Pubellier, M. (1993). Initiation of subduction and the generation of slab melts in western and eastern Mindanao, Philippines. *Geology* **21**, 1007-1010, doi: 10.1130/0091-7613(1993)021<1007:IOSATG>2.3.CO;2.

Sajona, F.G., Maury R.C., Bellon, H., Cotton, J., & Defant, M. (1996). High field strength element enrichment of Pliocene-Pleistocene island arc basalts, Zamboanga Peninsula, western Mindanao (Philippines), *Journal of Petrology* **37**, 693-726, https://doi.org/10.1093/petrology/37.3.693.

Salters, V.J.M., & Stracke, A. (2004). Composition of the depleted mantle. *Geochemistry, Geophysics, Geosystems* **5**, Q05B07, https://doi.org/10.1029/2003GC000597.

Samson, S.D., McClelland, W.C., Patchett, P.J., Gehrels, G.E., & Anderson R.G. (1989). Evidence from neodymium isotopes for mantle contributions to Phanerozoic crustal genesis in the Canadian Cordillera. *Nature* **337**, 705-709, https://doi.org/10.1038/337705a0.

Skulski, T., Minarik, W., & Watson, E.B. (1994). High-pressure experimental trace-element partitioning between clinopyroxene and basaltic melts. *Chemical Geology* **117**, 127-147, https://doi.org/10.1016/0009-2541(94)90125-2.

Smith, H.J., Spivack, A.J., Staudigel, H., & Hart, S.R. (1995). The boron isotopic composition of altered oceanic crust. *Chemical Geology* **126**, 199-135 https://doi.org/10.1016/0009-2541(95)00113-6.

Smith, E.I., Sánchez, A., Walker, J.D., & Wang, K. (1999). Geochemistry of mafic magmas in the Hurricane Volcanic Field, Utah: Implications for small- and large-scale chemical variability of the lithospheric mantle. *The Journal of Geology* **107**, 433-448, https://doi.org/10.1086/314355.

Snyder, D.C. (2005). Processes and time scales of differentiation in silicic magma chambers: chemical and isotopic investigations. Miami University, Ph.D. dissertation, 216 p.

Snyder, D.C., & Hart, W.K. (2007). The White Mountain Granitoid suite: Isotopic constraints on source reservoirs for Cretaceous magmatism within the Wrangellia Terrane. In: Ridgway, K.D., Trop, J.M., O'Neill, J.M., and Glen, J.M.G., (eds.) Tectonic growth of a collisional continental margin: crustal evolution of southern Alaska. *Geological Society of America Special Paper* **431**, 379-399, https://doi.org/10.1130/2007.2431(15).

Spivack, A.J., & Edmond, J.M. (1987). Boron isotope exchange between seawater and the oceanic crust. *Geochimica et Cosmochimica Acta* **51**, 1033-1043, https://doi.org/10.1016/0016-7037(87)90198-0.

Spotila, J.A., & Berger, A.L. (2010). Exhumation at orogenic indentor corners under long-term glacial conditions: Example of the St. Elias orogen, Southern Alaska. *Tectonophysics* **490**, 241-256, https://doi.org/10.1016/j.tecto.2010.05.015.

Stevenson, A.J., Scholl, D.W., & Vallier, T.L. (1983). Tectonic and geologic implications of the Zodiac fan, Aleutian Abyssal Plain, northern Pacific. *Geological Society of America Bulletin* **94**, 259-273, https://doi.org/10.1130/0016-7606(1983)94<259:TAGIOT>2.0.CO;2.

Stevenson, A.J., & Embley, R. (1987). Deep-sea fan bodies, terrigenous turbidite sedimentation, and petroleum geology, Gulf of Alaska. In: Scholl, D.W., Grantz, A., & Vedder, J.G., (eds.) Geology and resource potential of the continental margin of western North America and adjacent ocean basins – Beaufort Sea to Baja California. *Circum-Pacific Council for Energy and Mineral Resources Earth Science Series* **6**, 503-522.

Stout, J.H. (1976). Geology of the Eureka Creek area, east-central Alaska Range. State of Alaska, Department of Natural Resources, Division of Geological and Geophysical Surveys Geologic report **45**, 32 p., 1 sheet, scale 1:63,360, https://doi.org/10.14509/374.

Stracke, A. (2012). Earth's heterogenous mantle: A product of convention-driven interaction between crust and mantle. *Chemical Geology* **330-331**, 274-229. https://doi.org/10.1016/j.chemgeo.2012.08.007

Sugden, P.J., Savov, I.P., Agostini, S., Wilson, M., Halama, R., & Meliksetian, K. (2020). Boron isotope insights into the origin of subduction signatures in continent-continent collision zone volcanism. *Earth and Planetary Science Letters* **538**, 116207, https://doi.org/10.1016/j.epsl.2020.116207.

Teng, F.-Z., Wadhwa, M., & Helz, R.T. (2007). Investigation of magnesium isotope fractionation during basalt differentiation: Implications for a chrondritic composition of the terrestrial mantle. *Earth and Planetary Science Letters* **261**, 84-92, https://doi.org/10.1016/j.epsl.2007.06.004.

Teng, F.-Z., Li, W.-Y., Ke, S., Marty, B., Dauphas, N., Huang, S., Wu, F.-Y., & Pourmand, A. (2010). Magnesium isotopic composition of the Earth and chondrites. *Geochimica et Cosmochimica Acta*, 74 (14) 4150-4166, https://doi.org/10.1016/j.gca.2010.04.019.

Teng, F-Z., Li, W-Y., Ke, S., Yang, W., Liu, S-A., Sedaghatpour, F., Wang, S.-J., Huang, K.-J., Hu, Y., Ling, M.-X., Xiao, Y., Liu, X.-M., Li, X.-W., Gu, H.-O., Sio, C.K., Wallace, D.A., Su, B.-X., Zhao, L., Chamberlin, J., Harrington, M., & Brewer, A. (2015). Magnesium isotopic compositions of international geological reference materials. *Geostandards and Geoanalytical Research* **39**, 329-339, https://doi.org/10.1111/j.1751-908X.2014.00326.x.

Teng, F.-Z., Hu, Y., & Chauvel, C. (2016). Magnesium isotope geochemistry in arc volcanism. *Proceedings of the National Academy of Sciences* **113**(26), 7082-7087, https://doi.org/10.1073/pnas.1518456113.

Teng, F.-Z. (2017). Magnesium Isotope Geochemistry. *Reviews in Mineralogy and Geochemistry* **82**(1), 219-287, https://doi.org/10.2138/rmg.2017.82.7.

Thorkelson, D.J., & Breitsprecher, K. (2005). Partial melting of slab window margins: genesis of adakitic and non-adakitic magmas. *Lithos* **79**, 25-41, https://doi.org/10.1016/j.lithos.2004.04.049.

Tonarini S., Agostini, S., Doglioni, C., Innocenti, F., & Manetti, P. (2007). Evidence for serpentinite fluid in convergent margin systems: The example of El Salvador (Central America) arc lavas. *Geochemistry, Geophysics, Geosystems* **8**, Q09014, https://doi.org/10.1029/2006GC001508.

Trop, J.M., Ridgway, K.D., Manuszak, J.D., & Layer, P.W. (2002). Sedimentary basin development on the allochthonous Wrangellia composite terrane, Mesozoic Wrangell Mountains basin, Alaska: A long-term record of terrane migration and arc construction. *Geological Society of America Bulletin* **114**, 693-717, https://doi.org/10.1130/0016-7606(2002)114<0693:MSBDOT>2.0.CO;2.

Trop, J.M., Benowitz, J.A., Cole, R.B., & O'Sullivan, P. (2019). Cretaceous to Miocene magmatism, sedimentation, and exhumation within the Alaska Range suture zone: A polyphase reactivated terrane boundary. *Geosphere* **15**. 1066-1101, https://doi.org/10.1130/GES02014.1.

Trop, J.M., Benowitz, J.A., Koepp, D.Q., Sunderlin, D., Brueseke, M.E., Layer, P.W., & Fitzgerald, P.G. (2020). Stitch in the ditch: Nutzotin Mountains (Alaska) fluvial strata and dike record ca. 117-114 Ma accretion of Wrangellia with western North America and initiation of the Totschunda fault. *Geosphere* **16**, 82-110, https://doi.org/10.1130/GES02127.1.

Trop, J.M., Benowitz, J.A., Kirby, C., & Brueseke, M.E. (2022). Geochronology of the Wrangell Arc: Spatial-temporal evolution of slab edge magmatism along a slab subduction-transform transition, Alaska-Yukon. *Geosphere* **18**, 19-48, https://doi.org/10.1130/GES02417.1.

Twelker, E., Waldien, T.S., Newberry, R.J., Freeman, L.K., Sicard, K.R., Lande, L.L., Wypych, A., Reioux, D.A., & Bachmann, E.N. (2020). Bedrock geologic map of the eastern Denali Highway area, Mount Hayes, Healy, and Talkeetna Mountains quadrangles, Alaska. Alaska Division of Geological & Geophysical Surveys Report of Investigation 220-7: 1 sheet, 1:100,000 scale, https://doi.org/10.14509/30469.

U.S. Geological Survey, 20140322, USGS Alaska 5 Meter AK_IFSAR_2010 23: U.S. Geological Survey.

Vervoort, J.D., Plank, T., & Prytulak, J. (2011). The Hf-Nd isotopic composition of marine sediments. *Geochemica et Cosmochimica Acta* **75**, 5903-5926, https://doi.org/10.1016/j.gca.2011.07.046.

Villemant, B., Jaffrezic, H., Joron, J.L., & Treuil, M. (1981). Distribution coefficients of major and trace-elements – Fractional crystallization in the alkali basalt series of Chaine-Des-Puys (Massif Central, France). *Geochimca et Cosmochimca Acta* **45**, 1997-2016, https://doi.org/10.1016/0016-7037(81)90055-7.

Von Drach, V., Marsh, B.D., & Wasserburg, G.J. (1986). Nd and Sr isotopes in the Aleutians: multicomponent parenthood of island-arc magmas. *Contributions to Mineralogy and Petrology* **92**, 13-34, https://doi.org/10.1007/BF00373960.

Waldien, T.S., Lease, R.O., Roeske, S.M., Benowitz, J.A., & O'Sullivan, P.B. (2022). The role of preexisting upper plate strike-slip faults during long-lived (ca. 30 Myr) oblique flat slab subduction, southern Alaska. *Earth and Planetary Science Letters* **577**, 117242, https://doi.org/10.1016/j.epsl.2021.117242.

Walowski, K.J., Kirstein, L.A., De Hoog, J.C.M., Elliott, T., Savov, I.P., Jones, R.E., & EIMF. (2021). Boron recycling in the mantle: Evidence from a global comparison of ocean island basalts. *Geochimica et Cosmochimica Acta* **302**, 83-100, https://doi.org/10.1016/j.gca.2021.03.01.

Wang., Q., Xu, J-F., Jian, P., Bao, Z-W., Zhao, Z-H., Li, C-F., Xiong, X-L., & Ma, J-L. (2006). Petrogenesis of adakitic porphyries in an extensional tectonic setting, Dexing, South China: Implications for the genesis of porphyry copper mineralization. *Journal of Petrology* **47** (1), 119-114, https://doi.org/10.1093/petrology/egi070.

Wang, H., Wu, Y-B., Li, C-R., Zhao, T-Y., Qin, Z-W., Zhu, L-Q., Gao, S., Zheng, J-P., Liu, X-M., Zhou, L., Zhang, Y., & Yang, S-H. (2014). Recycling of sediment into the mantle source of K-rich mafic rocks: Sr-Nd-Hf-O isotopic evidence from the Fushui complex in the Qinling orogen. *Contributions to Mineralogy and Petrology* **168**, 1062, https://doi.org/10.1007/s00410-014-1062-y.

Wang, X-C, Wilde, S.A., Xu, B., & Pang, C-J. (2016). Origin of arc-like continental basalts: Implications for deep-Earth fluid cycling and tectonic discrimination. *Lithos* **261**, 5-45, https://doi.org/10.1016/j.lithos.2015.12.014.

Wang, X.-J., Chen, L.-C., Hanyu, T., Zhong, Y., Shi, J-H., Liu, X.-W., Kawabata, H., Zeng, G., & Xie, L.-W. (2022). Magnesium isotopic fractionation during basalt differentiation as recorded by evolved magmas. *Earth and Planetary Science Letters* **565**, 116954, https://doi.org/10.1016/j.epsl.2021.116954.

Wells, R., Bukry, D., Friedman, R., Pyle, D., Duncan, R., Haeussler, P., & Wooden, J. (2014). Geologic history of Siletzia, a large igneous province in the Oregon and Washington

Coast Range: Correlation to the geomagnetic polarity time scale and implications for a long-lived Yellowstone hotspot. *Geosphere* **10**(4), 692-719, https://doi.org/10.1130/GES01018.1.

White, W.M., Hofmann, A.W., & Puchelt, H. (1987). Isotopic geochemistry of pacific mid-ocean ridge basalt. *Journal of Geophysical Research* **92**, 4881-4893 https://doi.org/10.1029/JB092iB06p04881.

White, T., Bradley, D., Haeussley, P., & Rowley, D.B. (2017). Late Paleocene-Earth Eocene paleosols and a new measure of the transport distance of Alaska's Yakutat Terrane. *Journal of Geology* **125**, 113-123, https://doi.org/10.1086/690198.

Wirth, K.R., Grandy, J., Kelly, K., & Sadofsky, S. (2002). Evolution of crust and mantle beneath the Bering Sea region: Evidence from xenoliths and late Cenozoic basalts. *Geological Society of America Special Paper* **360**, 167-193.

Worthington, L.L., Van Avendonk, H.J., Gulick, S.P., Christeson, G.L., & Pavlis, T.L. (2012). Crustal structure of the Yakutat terrane and the evolution of subduction and collision in southern Alaska. *Journal of Geophysical Research: Solid Earth* **147**, B01102, https://doi.org/10.1029/2011JB008493.

Wood, C.A., & Kienle, J. (eds.) (1990). *Volcanoes of North America: United States and Canada*. Cambridge University Press, 354 p.

Yogodinski, G.M., Kay, R.W., Volynets, O.N., Koloskov, A.V., & Kay, S.M. (1995). Magnesian andesite in the western Aleutian Komandorsky region: implications for slab melting and processes in the mantle wedge. *Geological Society of America Bulletin* **107**, 505-519, https://doi.org/10.1130/0016-7606(1995)107<0505:MAITWA>2.3.CO;2.

Yogodinski, G.M., Lees, J.M., Churikova, T.G., Dorendorf, F., Wöerner, G., & Volynets, O.N. (2001). Geochemical evidence for the melting of subducting oceanic lithosphere at plate edges. *Nature* **409**, 500-504, https://doi.org/10.1038/35054039.

Zack, T., & Brumm, R. (1998). Illmenite/liquid partition coefficients of 26 trace elements determined through ilmenite/clinopyroxene partitioning in garnet pyroxene. In: Gurney, J.J., Gurney, J.L., Pascoe, M.D., & Richardson, S.H., (eds.) *7th International Kimberlite Conference*, Red Roof Design, Cape Town, 986-988.

Zhang, L.Y., Ducea, M.N., Ding, L., Pullen, A., Kapp, P., & Hoffman, D. (2014). Southern Tibetan Oligocene-Miocene adakites: a record of Indian slab tearing. *Lithos* **210-211**, 209-223, https://doi.org/10.1016/j.lithos.2014.09.029.

Zhang, L-.Y., Fan, W.M., Ding, L., Ducea, M.N., Pullen, A., Li, J.X., Sun, Y.L., Yue Y.H., Cai, F.L., Wang, C., Peng, T.P. & Sein, K. (2020). Quaternary volcanism in Myanmar: A record of Indian slab tearing in a transition zone from oceanic to continental subduction. *Geochemistry, Geophysics, Geosystems* **21**, e2020GC009091, https://doi.org/10.1029/2020GC009091.

Zhang, L., Li, S., & Zhao, Q. (2021). A review of research on adakites. *International Geology Review* **63**, 47-64, doi:10.1080/00206814.2019.1702592.

Zhang, G., Zhang, J., Dalton, H., & Phillips, D. (2022). Geochemical and chronological constraints on the origin and mantle source of Earth Cretaceous arc volcanism on the Gagua Ridge in Western Pacific. *Geochemistry, Geophysics, Geosystems* **23**, e2022GC010424. https://doi.org/10.1029/2022GC010424.

Zhong, Y., Chen, L.-H., Wang, X.-J., Zhang, G.-L., Xie, L.-W., & Zeng, G. (2017). Magnesium isotopic variation of oceanic island basalts generated by partial melting and crustal recycling. *Earth and Planetary Science Letters* **463**, 127-135, https://doi.org/10.1016/j.epsl.2017.01.040.

Zamboni, D., Gazel, E., Ryan, J.G., Cannatelli, C., Lucchi, F., Atlas, Z.D., Trela, J., Mazza, S.E., & De Vivo, B. (2016). Contrasting sediment melt and fluid signatures for magma components in the Aeolian Arc: Implications for numerical modeling of subduction systems. *Geochemistry, Geophysics, Geosystems* **17**, 2034-2053, https://doi.org/10.1002/2016GC006301.

Appendix A - Supplementary Geochemistry

Whole rock major and trace element data for rocks from Jumbo Dome, Sonya Creek Volcanic Field, and Mt. Drum that were analyzed for B-Mg isotope composition are reported below.

Sample	05JDDS02	SB15-31*	SB15-39*	15JB25LA*	73ARh21**
Unit	Jumbo Dome	SCVF	SCVF	SCVF	WVF
SiO_2	59.19	56.55	49.21	50.70	55.52
TiO_2	0.65	1.06	1.39	1.37	1.00
Al_2O_3	17.51	16.55	16.90	16.39	17.08
FeO*		7.05	9.88	9.10	7.02
MnO	0.11	0.12	0.17	0.15	0.12
MgO	4.06	5.11	8.52	7.60	6.32
CaO	7.56	7.46	9.28	9.77	7.42
Na_2O	2.99	4.04	3.39	3.47	3.74
K_2O	2.32	1.46	0.61	0.71	0.90
P_2O_5	0.18	0.30	0.29	0.40	0.28
LOI	0.08	0.55	1.53	1.04	0.10
Mg#	67.50	56.30	60.60	59.80	66.75
Ba	1135	386	215	289	349
Cr	28.7	139	282	221	215
Cs	0.52	0.53	0.10	0.19	
Cu	56.2				
Ga	20.7				
Hf	3.47	4.44	2.66	2.90	
Mo	0.97				
Nb	6.68	8.7	8.9	9.4	3.6
Ni	15.7	63	139	71	137
Pb	4.68	4.0	2.0	2.0	
Rb	35.2	31	9	10	14
Sc	17.67	21	31	31	21
Sr	1051	574	540	632	571
Ta	0.45	0.63	0.57	0.53	
Th	3.80	3.2	1.0	1.5	1.6
U	1.42	1.3	0.4	0.6	2.0
V	157	165	207	207	157
Y	13.69	22	23	24	18
Zn	64				
Zr	122	187	108	119	118
La	15.52	18.42	12.11	18.50	
Ce	29.84	38.24	26.92	39.79	
Pr	3.66	4.81	3.66	5.23	
Nd	14.53	19.35	16.23	21.82	
Sm	3.10	4.52	4.20	5.14	
Eu	0.99	1.33	1.52	1.64	
Gd	2.76	4.34	4.22	4.83	
Tb	0.43	0.71	0.73	0.79	
Dy	2.53	4.41	4.58	4.80	
Ho	0.51	0.89	0.92	0.97	
Er	1.40	2.39	2.51	2.60	
Tm		0.34	0.36	0.36	
Yb	1.31	2.18	2.23	2.25	
Lu	0.21	0.33	0.36	0.34	
$^{87}Sr/^{86}Sr_m$		0.703597	0.703734	0.704237	0.70351
$^{143}Nd/^{144}Nd_m$		0.513005	0.512968	0.512841	0.513002
$^{206}Pb/^{204}Pb$		38.3722	38.2510	38.4169	38.34
$^{207}Pb/^{204}Pb$		15.5629	15.5499	15.5709	15.558
$^{208}Pb/^{204}Pb$		18.9321	18.8137	18.9740	18.83

Note: All major element data expressed as raw weight % oxide; FeO* is total Fe; trace element concentrations in ppm. N.d. = not determined. Samples with 1 asterisk (*) are from Berkelhammer (2017); samples with 2 asterisks (**) are from Preece (1997). Sr-Nd data reported as measured.

Appendix B - Sample Locations and Petrographic Descriptions

Volcano #1

Sample ID: DEN20-10 **Latitude:** 63.2357

Rock Type: Basaltic andesite **Longitude:** -146.1944

Thin Section Description: Based on thin section description, the rock is hypocrystalline, aphanitic, porphyritic, and contains olivine phenocrysts within a finer-grained, intergranular groundmass consisting of plagioclase (71%), clinopyroxene (12%), oxides (10%), biotite (6%), and olivine (1%). The sample is approximately (4.5%) phenocrysts and (95.5%) groundmass. Mineral abundances were calculated via point counting at 1 mm intervals. Olivine phenocryst grainsizes range from 0.425 mm to 1.18 mm. Groundmass grains range from 0.06 mm – 0.21 mm with plagioclase, biotite, and olivine on the larger side and smaller clinopyroxene and oxides. Olivine phenocrysts are generally anhedral and display a swallowtail morphology. Groundmass plagioclase and biotite are subhedral to euhedral and are tabular. Textures and alteration displayed within the sample are described as follows. Alteration within the sample is confined to olivine phenocrysts and voids. Olivine phenocrysts display iddingsite alteration along fractures and grain boundaries. Radial aggregates of chlorite are present in groundmass and extend into voids. Olivine phenocrysts commonly host spinel inclusions and display resorbed margins. Groundmass plagioclase display pilotaxitic to felty flow textures and polysynthetic twinning.

Sample ID: DEN20-11 **Latitude:** 63.2368

Rock Type: Basaltic andesite **Longitude:** -146.1924

Thin Section Description: Based on thin section description, the rock is hypocrystalline, aphanitic, porphyritic, and contains olivine phenocrysts within a finer-grained intergranular groundmass consisting of plagioclase (79%), clinopyroxene (7%), oxides (7%), biotite (5%), and olivine (1%). The sample is approximately (6%) phenocrysts and (94%) groundmass. Mineral abundances were calculated via point counting at 1 mm intervals. Olivine phenocryst grains range from 0.26 – 1.12 mm. Groundmass grains range from 0.0075 mm – 0.17 mm with plagioclase, biotite, and olivine on the larger side and smaller clinopyroxene and oxides. Olivine phenocrysts are generally subhedral to anhedral and display a swallowtail morphology. Groundmass

plagioclase and biotite are subhedral to euhedral and are tabular. Groundmass clinopyroxene are subhedral. Textures and alteration displayed within the sample are described as follows. Alteration within the sample is confined to olivine phenocrysts and voids. Olivine phenocrysts display iddingsite alteration along fractures and grain boundaries. Radial aggregates of chlorite are present in groundmass and extend into voids. Olivine phenocrysts commonly host spinel inclusions and display resorbed margins. Groundmass plagioclase display pilotaxitic to felty flow textures and polysynthetic twinning

Volcano #2

Sample ID: DEN20-01 **Latitude:** 63.1358

Rock Type: Trachybasalt **Longitude:** -146.3252

Thin Section Description: Based on thin section description, the rock is hypocrystalline, aphanitic, seriate, porphyritic, vesicular, and contains olivine (48%), clinopyroxene (34%), phlogopite (15%), and amphibole (3%) phenocrysts within a finer-grained, intersertal groundmass consisting of plagioclase, olivine, phlogopite, clinopyroxene, and glass. The sample is approximately 18% phenocrysts and 82% groundmass. Mineral abundances were calculated via point counting at 1 mm intervals. Phenocrysts range in size from 0.25 - 0.95 mm with all minerals encompassing this size range. Groundmass grains range from 0.025 - 0.07 mm with all minerals encompassing the size range. Minerals within the sample are unoriented. Olivine, clinopyroxene, amphibole phlogopite are subhedral while plagioclase is generally euhedral. Olivine and amphibole are prismatic, phlogopite and plagioclase are tabular, and clinopyroxene range from tabular to equant. The rock is glomeroporphyritic with glomerocrysts of olivine, clinopyroxene, and phlogopite.

Slight alteration is found within the groundmass, olivine crystals, and an amphibole. Olivine display iddingsite alteration along fractures and grain boundaries. Within the sample is a large (1.05 mm) amphibole with chlorite alteration and partial replacement by phlogopite altered to chlorite. This amphibole does not contain any opacitic rims. Large black opaque/opacitic tabular crystals occur within the sample and may be amphibole. The groundmass glass is altered to a reddish-brown color. The sample also contains two xenocrysts: (1) an elongate, anhedral potassium-feldspar xenocryst (4.25 mm) with evidence of resorption; and (2) an anhedral quartz xenocryst (0.95 mm) with subgrain boundaries.

Clinopyroxene and olivine phenocrysts display evidence of reabsorption and sieve textures. Some clinopyroxene contain phlogopite within their crystal boundaries. Phlogopite display black/brown opacitic rims and may be altered to a reddish-brown color. Clinopyroxene phenocrysts display oscillatory zoning. Melt inclusions are found within olivine, clinopyroxene, phlogopite, and amphibole.

Sample ID: DEN20-03 **Latitude:** 63.1371

Rock Type: Trachybasalt **Longitude:** -146.3217

Thin Section Description: Based on thin section description, the rock is hypocrystalline, aphanitic, porphyritic/seriate, vesicular, and contains olivine (53%), clinopyroxene (27%), phlogopite (12%) and amphibole (8%) phenocrysts within a finer-grained, intersertal groundmass consisting of plagioclase, phlogopite, clinopyroxene, opacitic black amphibole, and oxides. The sample is approximately (26%) phenocrysts, (73%) groundmass, and 1% xenoliths/xenocrysts. Mineral abundances were calculated via point counting at 1 mm intervals. Phenocrysts range in size from 0.25 - 1.5 mm with larger olivine and amphibole, and smaller clinopyroxene and phlogopite. Groundmass grains range from 0.03 – 0.20 mm with all minerals encompassing the size range. Minerals within the sample are unoriented and the groundmass is felty. Mineral grains are euhedral to subhedral. Olivine and amphibole are prismatic, phlogopite and plagioclase are tabular, and clinopyroxene range from tabular to equant. The rock is glomeroporphyritic with glomerocrysts (or cumulates) of olivine, clinopyroxene, phlogopite, and plagioclase.

A summary of xenoliths and xenocrysts is as follows. Two microcline xenocrysts, three quartz xenocrysts, and grainy clots of oxidized minerals/opacitic minerals are found within the sample. Microcline xenocrysts are between 0.4 – 0.46 mm in length and have tartan twinning. Three quartz xenoliths are found within the sample. The first is 1.625 mm in length with a clinopyroxene and plagioclase reaction rim. The second is 1.99 mm in length, with large resorbed margins partially filled with groundmass plagioclase, olivine, and clinopyroxene, and has a reaction rim. The third is smaller and is 0.15 mm in length.

Alteration is restricted to olivine and vesicles. Olivine display iddingsite alteration along mineral boundaries and fractures. Vesicles are occasionally filled with chlorite. Amphibole phenocrysts are opacitic, indicating decompression breakdown. Textures displayed within the sample are described as follows. Olivine and clinopyroxene phenocrysts display evidence or

reabsorption and sieve textures. Clinopyroxene display oscillatory zoning. Trailing melt inclusions are found in olivine, clinopyroxene, plagioclase, and in the potassium feldspar xenocryst. Corona/reaction rims are found around quartz xenocrysts.

Sample ID: DEN20-04 **Latitude:** 63.1286

Rock Type: Trachybasalt **Longitude:** -146.3224

Thin Section Description: Based on thin section description, the rock is hypocrystalline, aphanitic, porphyritic/seriate, vesicular, and contains olivine (31%), clinopyroxene (29%), opacitic amphibole (23%), and phlogopite (8%) phenocrysts within a finer-grained, intergranular groundmass consisting of plagioclase, olivine, phlogopite, clinopyroxene, and opacitic amphibole. The sample is approximately 27% phenocrysts, 72% groundmass, and 1% xenoliths/xenocrysts. Mineral abundances were calculated via point counting at 1 mm intervals. Phenocrysts range in size from 0.25 – 1.6 mm with all minerals making up this size range. Groundmass grains range from 0.03 – 0.20 mm with larger phlogopite, olivine, amphibole, and clinopyroxene and smaller plagioclase. The groundmass plagioclase orientation lies between felty and pilotaxitic plagioclase orientation varies locally within the thin section. Mineral grains are euhedral to subhedral. Olivine and amphibole are prismatic, phlogopite and plagioclase are tabular, and clinopyroxene range from tabular to equant.

A summary of xenoliths and xenocrysts is as follows. Five quartz xenocrysts and 2 plagioclase xenocrysts are found within the sample. Quartz xenocrysts range in size from 0.25 – 1.63. Quench rinds are found on smaller xenocrysts and consist of clinopyroxene and plagioclase. Some quartz xenocrysts display phlogopite inclusions and resorbed margins. Plagioclase xenocrysts are anhedral with zoning, melt inclusions, and mineral inclusions (e.g., phlogopite).

Next, sample alteration and textures are described. Alteration is restricted to olivine, xenocrysts, and vesicles. Olivine display iddingsite alteration along mineral boundaries and fractures and some groundmass olivine are completely replaced by iddingsite. Olivine also contain spinel inclusions. Amphibole are opacitic. Olivine phenocrysts display corona reaction rims composed of clinopyroxene. Clinopyroxene phenocrysts display oscillatory zoning. Olivine and clinopyroxene phenocrysts display evidence of reabsorption and sieve textures. Melt inclusions are present in olivine and clinopyroxene phenocrysts.

Sample ID: DEN20-12 **Latitude:** 63.1364

Rock Type: Trachybasalt **Longitude:** -146.3199

Thin Section Description: Based on thin section description, the rock is hypocrystalline, aphanitic, porphyritic/seriate, and vesicular with olivine (50%), clinopyroxene (28%), phlogopite (21%), and amphibole (2%) phenocrysts within a finer-grained, intersertal groundmass consisting of plagioclase, olivine, clinopyroxene, phlogopite, amphibole, oxides, and glass. The sample is approximately (19%) phenocrysts and (80%) groundmass. Mineral abundances were calculated via point counting at 1 mm intervals. Phenocrysts range in size from 0.25 – 1.18 mm with each mineral making up the entire size spectrum. Groundmass grains range from 0.02 – 0.20 mm with plagioclase on the smaller side of the size range while other minerals are larger. The groundmass is unoriented. Mineral grains are euhedral to subhedral. Olivine and amphibole are prismatic. Clinopyroxene, phlogopite, and plagioclase are tabular. The rock is also glomeroporphyritic with glomerocrysts of clinopyroxene, olivine, and phlogopite.

A summary of xenoliths and xenocrysts is as follows. The sample contains a plagioclase + potassium feldspar xenolith 2.3 mm in length. It displays polysthentic twinning and oscillatory zoning. There is also a anhedral quartz xenocryst 0.45 mm in length. Next, alteration and textures are described. Slight alteration is restricted to olivine, and the glassy groundmass. Olivine display iddingsite alteration along grain boundaries and fractures. The groundmass glass is altered to a reddish-brown color. Olivine, clinopyroxene, and phlogopite display sieve textures and reabsorbed margins. Oscillatory zoning is found within clinopyroxene and amphibole. Finally, textures within the sample are summarized. Clinopyroxene phenocrysts display simple twins. Trailing melt inclusions are present in olivine phenocrysts. Olivine phenocrysts also display corona rims with clinopyroxene.

Sample ID: DEN20-13 **Latitude:** 63.1364

Rock Type: Basalt **Longitude:** -146.3199

Thin Section Description: Based on thin section description, the rock is highly phyric porphyritic/seriate, and vesicular with phlogopite (40%), clinopyroxene (27%), olivine (25%), and amphibole (8%) phenocrysts within a finer-grained, intersertal groundmass consisting of olivine, clinopyroxene, phlogopite, plagioclase, amphibole, and oxides. The sample is approximately (21%) phenocrysts, (77%) groundmass, 2% xenoliths/xenocrysts. Mineral abundances were calculated via point counting at 1 mm intervals. Phenocrysts range in size from 0.25 – 1.25 mm with larger phlogopite, amphibole, and smaller clinopyroxene and olivine. Groundmass grains range from 0.02 – 0.1 mm with all minerals encompassing this size range. The groundmass is unoriented. Primary mineral grains are euhedral to subhedral. Plagioclase, phlogopite, and clinopyroxene are tabular. Olivine and amphibole are prismatic. The rock is also glomeroporphyritic with glomerocrysts/clots of clinopyroxene, phlogopite, and olivine.

A summary of xenoliths and xenocrysts is as follows. The sample contains 4 quartz xenocrysts, 2 plagioclase xenocrysts, and 1 quartz + potassium feldspar xenolith. Quartz xenocrysts range in size from 0.2 – 2.28 mm with larger crystals displaying subgrain boundaries and resorbed margins. Plagioclase xenocrysts range in size between 0.71 – 1.8 mm, are rounded, and display polysynthetic twinning, resorbed margins, and melt inclusions. The potassium feldspar + quartz xenolith is anhedral, with Carlsbad twining, zoning, and subgrain boundaries within the quartz.

Next, alteration and textures are described. Alteration is primarily restricted to olivine which display partial iddingsite alteration along grain boundaries and fractures. Some amphibole olivine, clinopyroxene, and phlogopite phenocrysts display sieve textures and evidence of resorption. Phlogopite display kink bands. A poikilitic amphibole phenocryst encloses clinopyroxene and phlogopite. Some olivine phenocrysts have corona rims/reaction rims with clinopyroxene. Clinopyroxene phenocrysts display simple twins. Plagioclase and clinopyroxene display variolitic texture in voids/vesicles. Phlogopite and plagioclase are locally pilotaxitic within the thin section.

Sample ID: DEN20-14 **Latitude:** 63.1364

Rock Type: Trachybasalt **Longitude:** -146.3199

Thin Section Description: Based on thin section description, the rock is hypocrystalline, aphanitic, porphyritic/seriate, and vesicular with olivine (45%), clinopyroxene (35%), phlogopite (17%), and amphibole (3%), phenocrysts within a finer-grained, intersertal groundmass consisting of plagioclase, amphibole, phlogopite, olivine, clinopyroxene, oxides and glass. The sample is approximately (21%) phenocrysts, (78%) groundmass, and 2% xenoliths/xenocrysts. Mineral abundances were calculated via point counting at 1 mm intervals. Phenocrysts range in size from 0.25 – 2.58 mm with larger amphibole and smaller olivine and phlogopite. Groundmass grains range from 0.005 – 0.2 mm with all minerals encompassing this size range. The groundmass is unoriented. Primary mineral grains are euhedral to subhedral. Clinopyroxene are equant or tabular. Amphibole phenocrysts are prismatic to tabular, olivine is prismatic, and plagioclase and phlogopite are tabular. The rock also is glomeroporphyritic with glomerocrysts of clinopyroxene, olivine, phlogopite, and amphibole.

A summary of xenoliths and xenocrysts are as follows. The sample contains a quartz xenocryst (4.95 mm in length) with sutured grain boundaries, undulatory extinction, and melt inclusions. The xenocryst contains embayments and fractures filled with groundmass. It also contains a colorless, elongated prismatic inclusion (0.04 mm) with second order birefringence.

Next, alteration and textures are described. Alteration is primarily resetricted to olivine and the glassy groundmass. Olivine display iddingsite alteration along grain boundaries and fractures. The glass groundmass is altered to a reddish-brown color. Amphibole, clinopyroxene, phlogopite, and olivine phenocrysts display evidence of reabsorption and sieve textures. Some reabsorbed amphibole have phlogopite inclusions. Clinopyroxene phenocrysts display simple twins. Amphibole and clinopyroxene phenocrysts are zoned. Melt inclusions are present within ampihibole, clinopyroxene and olivine. Olivine phenocrysts contain spinel inclusions.

Sample ID: AB22-1 **Latitude:** 63.1251

Rock Type: Trachybasalt **Longitude:** -146.3333

Thin Section Description: Based on thin section description, the rock is hypocrystalline, aphantic, porphyritic/seriate, and vesicular. The rock consists of olivine (36%), clinopyroxene (40%) opacitic amphibole (17%), and phlogopite (7%) phenocrysts set within a finer-grained,

intergranular groundmass consisting of plagioclase, clinopyroxene, olivine, amphibole, phlogopite, and oxides. The sample is approximately (21%) phenocrysts and (79%) groundmass. Mineral abundances were calculated via point counting at 1 mm intervals. Phenocrysts range in size from 0.25 - 1.3 mm with all minerals encompassing this size range. Groundmass grain sizes are less than > 0.15 mm. Overall, the groundmass is unoriented. Primary mineral grains are subhedral to euhedral. The rock is also glomeroporphyritic with glomerocrysts of clinopyroxene and olivine.

A summary of xenoliths and xenocrysts is as follows. The sample contains a microcline xenocryst (1.4 mm) and a plagioclase xenocryst (0.5 mm). Both xenocrysts show evidence of resorption. Next, alteration and textures are described. Alteration is primarily restricted to olivine, amphibole and phlogopite. Olivine display partial to complete iddingsitization while amphibole and phlogopite have opacitic rims, often with complete replacement by oxides. However, phlogopite in vesicles remains unaltered. Clinopyroxene phenocrysts display oscillatory zoning. Olivine and clinopyroxene phenocrysts show evidence of resorption and sieve textures. There is also a clinopyroxene phenocryst with a green, anhedral aegirine core.

Volcano #3

Sample ID: DEN20-5 **Latitude:** 63.0553

Rock Type: Andesite **Longitude:** -146.3132

Thin Section Description: Based on thin section description, the rock is hypocrystalline, aphanitic, porphyritic, vesicular with clinopyroxene (62%), and olivine (38%), and opacitic amphibole (1%) within a finer-grained, intergranular groundmass consisting of plagioclase (82%), olivine (4%), clinopyroxene (12%), amphibole (1%), and biotite (1%). The sample is approximately (2%) phenocrysts and (98%) groundmass. Mineral abundances were calculated via point counting at 1 mm intervals. Phenocrysts range in size from 0.40 mm – 1 mm with larger amphibole and smaller olivine and phlogopite. Groundmass grains range from 0.02 – 0.25 mm with all minerals encompassing this size range. Plagioclase displays a trachytic flow texture. Primary mineral grains are generally subhedral. Clinopyroxene, amphibole, and olivine are prismatic. Plagioclase and phlogopite are tabular. The rock is also glomerporphyritic with glomerocrysts of clinopyroxene and olivine.

Next a summary of xenoliths, alteration, and textures are summarized. The sample contains a grainy xenolith composed of quartz and plagioclase crystals. Alteration appears to be restricted to olivine and biotite microlites. Some of the microlites have slightly opacitic/higher relief rims. Amphibole are opacitic. Clinopyroxene and olivine phenocrysts display evidence of resorption and sieve textures. Plagioclase have polysynthetic twinning and display a variolitic texture.

Sample ID: DEN20-6 **Latitude:** 63.0578

Rock Type: Andesite **Longitude:** -146.3132

Thin Section Description: Based on thin section description, the rock is hypocrystalline, aphanitic, and porphyritic with olivine (31%), amphibole (8%), and clinopyroxene (62%) phenocrysts and within a finer-grained, intergranular groundmass consisting of plagioclase (79%), olivine (3%), clinopyroxene (18%), amphibole (1%), and biotite (1%). The sample is approximately (2%) phenocrysts, (95%) groundmass, and 5% xenoliths/xenocrysts. Phenocrysts range in size from 0.37– 0.82 mm with larger amphibole and smaller olivine and clinopyroxene. Groundmass grains range from 0.01 – 0.23 mm with all minerals encompassing this size range.

The sample contains multiple xenoliths and xenocrysts which are comprised of either quartz + plagioclase or siliclastic, grainy and opaque lithics. The quartz + plagioclase xenoliths/xenocrysts ranging in size from 0.2 – 0.8mm in size. These consist of quartz and plagioclase and are commonly sieved with resorbed margins. The grainy xenoliths range in size from 0.25 – 1.87 mm.

Alteration and textures are summarized next. Amphibole are opacitic. Clinopyroxene phenocrysts display simple twins, and one phenocryst has a green aegirine core. Olivien and clinopyroxene phenocrysts also are sieved with evidence of resorption. Groundmass plagioclase are pilotaxitic. The sample also has areas of finer-grained groundmass in which larger plagioclase laths flow around.

Sample ID: DEN20-7 **Latitude:** 63.0547

Rock Type: Andesite **Longitude:** -146.3110

Thin Section Description: Based on thin section description, the rock is hypocrystalline, aphanitic, and porphyritic with olivine (14%), amphibole (7%), and clinopyroxene (79%) phenocrysts and within a finer-grained, intergranular groundmass consisting of plagioclase (84%), olivine (4%), clinopyroxene (12%), amphibole (1%), and oxides. The sample is approximately (3%) phenocrysts and (97%) groundmass. Phenocrysts range in size from 0.3 - 0.7 mm with larger olivine and clinopyroxene and smaller amphibole. Groundmass is less than 0.25 mm in size and groundmass plagioclase are pilotaxitic. Phenocrysts are subhedral and the groundmass ranges from euhedral to subhedral. Plagioclase and clinopyroxene are tabular, while olivine and amphibole are prismatic.

Next, xenoliths, alteration, and textures are summarized. The sample contains siliclastic, grainy and opaque lithics (0.2 – 1 mm). These are anhedral with and appear "smudged" and blurry. Alteration is restricted to olivine, which display very slight alteration to iddingsite. Amphibole are opacitic. Clinopyroxene phenocrysts display oscillatory zoning, with evidence of resorption and sieve textures.

Sample ID: AB22-3 **Latitude:** 63.0577

Rock Type: Andesite **Longitude:** -146.3046

Thin Section Description: Based on thin section description, the rock is hypocrystalline, aphanitic, porphyritic, and vesicular. The rock consists of clinopyroxene (100%) phenocrysts set within a finer-grained groundmass consisting of plagioclase laths (86%), olivine (3%), clinopyroxene (11%), oxides, and biotite microlites. Mineral abundances were calculated via point counting at 1 mm intervals. Phenocrysts range in size from 0.3 – 0.73 mm. Groundmass grains are generally < 0.25 mm with larger plagioclase, olivine, and clinopyroxene, and smaller oxides and biotite. Mineral grains are subhedral to anhedral. Plagioclase laths in the groundmass are pilotaxitic. The rock is also glomeroporphritic with clinopyroxene and olivine glomerocrysts.

Next, xenoliths/xenocrysts, alteration, and textures are summarized. The rock contains xenoliths and xenocrysts of plagioclase and quartz that range in size from 0.20 – 0.95 mm. These display evidence of resorption and are sieved. Alteration is restricted to olivine, which display occasional iddingsite alteration along crystal boundaries and fractures. Groundmass clinopyroxene

display simple twinning. Clinopyroxene phenocrysts display evidence of resorption and have sieve textures. Clinopyroxene phenocrysts also display oscillatory zoning. Olivine phenocrysts contain spinel inclusions. Plagioclase display polysynthetic twinning.

Sample ID: AB22-4 **Latitude:** 63.0589

Rock Type: Andesite **Longitude:** -146.3045

Thin Section Description: Based on thin section description, the rock is hypocrystalline, aphanitic, porphyritic, and vesicular. The rock consists of olivine (21%), clinopyroxene (65%), and opacitic amphibole (3%) phenocrysts set within a finer-grained groundmass consisting of plagioclase laths (88%), olivine (3%), clinopyroxene (8%), oxides, and biotite microlites. Mineral abundances were calculated via point counting at 1 mm intervals. Phenocrysts range in size from 0.3 – 0.85 mm, with larger clinopyroxene and smaller olivine. Groundmass grains are less than > 0.25 in size. Mineral grains are subhedral to anhedral. Plagioclase laths in the groundmass are pilotaxitic. The rock is also glomeroporphritic with clinopyroxene and olivine glomerocrysts.

Next, a summary of xenoliths, alteration, and texture are described. The sample contains a grainy xenolith that is opacitic/partially opaque and is .5 mm long. Alteration is restricted to olivine, where few crystals display slight alteration to iddingsite. Clinopyroxene phenocrysts display resorbed margins and sieve textures. Clinopyroxene also display simple twins, and one phenocryst has a green aegirine gore surrounded by a lighter green, zoned rim.